UNIVERSITÉ DE MONTRÉAL

DISPERSION BASED REAL-TIME ANALOG SIGNAL PROCESSING (R-ASP) AND APPLICATION TO WIRELESS COMMUNICATIONS

LIANFENG ZOU
DÉPARTEMENT DE GÉNIE ÉLECTRIQUE
ÉCOLE POLYTECHNIQUE DE MONTRÉAL

THÈSE PRÉSENTÉE EN VUE DE L'OBTENTION
DU DIPLÔME DE PHILOSOPHIÆ DOCTOR
(GÉNIE ÉLECTRIQUE)
DÉCEMBRE 2017

UNIVERSITÉ DE MONTRÉAL

ÉCOLE POLYTECHNIQUE DE MONTRÉAL

Cette thèse intitulée :

DISPERSION BASED REAL-TIME ANALOG SIGNAL PROCESSING (R-ASP) AND APPLICATION TO WIRELESS COMMUNICATIONS

présentée par : ZOU Lianfeng
en vue de l'obtention du diplôme de : Philosophiæ Doctor
a été dûment acceptée par le jury d'examen constitué de :

M. NERGUIZIAN Chahé , Ph. D., président
M. CALOZ Christophe, Ph. D., membre et directeur de recherche
M. CHEN Lawrence, Ph. D., membre
M. AZAÑA José, Ph. D., membre externe

DEDICATION

To my family

ACKNOWLEDGEMENTS

My deepest gratitude goes to professor Christophe Caloz, who has been the educator, the motivator, and the mentor for my life beyond research. His spirit, enthusiasm and endeavour for scientific research inspires me to pursue a challenging career.

I would like to convey my acknowledgement to the committee members, professor Chahé Nerguizian from École Polytechnique de Montréal, professor José Azaña from INRS, professor Lawrence Chen from McGill university, for having accepted to examine my thesis.

I would also like to thank my former colleagues Qingfeng Zhang, Babak Nikfal and Shulabh Gupta for their invaluable help and advice on my research, and Zoé-Lise Deck-Léger for translating the abstract of the thesis into French, and all the colleagues in Christophe's group for the communication on regular basis.

None of the experimental works would have been successful, if without the assistance of all the technical staffs from Poly-GRAMES Research Center and from outside. I want to give my thanks to Jules Gauthier, Steve Dubé, Traian Antonescu and Maxime Thibault, and also to Normand Gravel from ÉTS, for helping me fabricate components and systems. I am also grateful to Jean-Sébastien Décarie for his excellent IT administration, and to Ms. Nathalie Lévesque and Ms. Rachel Lortie for their daily administrative work.

Last but not least, a lot of thanks and loves go to my parents and my girlfriend, for always being supportive and making me happy.

RÉSUMÉ

Nous sommes confrontés à une demande explosive de systèmes radio plus rapides, plus fiables et plus écoénergétiques, pour la communication sans fil 5G par exemple. On s'attend à ce que la capacité des données mobiles dépasse 1000 fois ce qu'elle est actuellement dans la prochaine décennie. Un tel volume de données nécessite un grand spectre de bande passante. Aux fréquences radio-fréquences (RF) faibles, le spectre est congestionné par des milliards d'appareils radio. Dans les hautes fréquences, le spectre de bande passante ultra large (UWB) est moins congestionné. Cependant, le traitement d'un tel signal UWB RF pose de grands défis au niveau du traitement du signal (DSP) numérique, qui est habituellement utilisé pour les basses fréquences et les bandes passantes étroites. Les problèmes dont souffre le DSP pour les signaux hautes fréquences sont la limitation de la vitesse, le coût élevé et la forte consommation d'énergie pour la conversion analogique / numérique (ADC). Par conséquent, une technique de traitement en temps réel et purement analogique est souhaitable. En optique, les gens ont traité des signaux RF UWB avec des approches photoniques hyperfréquences en temps réel, mais cela impliquait une conversion électrique / optique coûteuse. Le traitement de signal analogique d'une onde radio en temps réel (R-ASP) est une alternative attrayante et moins exploitée. Le premier chapitre présente l'état de l'art de la technologie R-ASP ainsi que la contribution de la thèse.

Le composant au cœur du traitement R-ASP s'appelle "phaseur", un composant qui fournit un retard de groupe spécifié $\tau(\omega)$ à une onde radio. Un phaseur, en réponse à un signal d'excitation large bande, réorganise les composants spectraux dans le temps. La façon dont un phaseur réorganise le spectre dépend de la fonction de retard de groupe, $\tau(\omega)$. Différentes applications R-ASP peuvent nécessiter des profils de retard de groupe différents. Le chapitre 2 introduit le concept de retard de groupe, présente différentes technologies phaseur, et présente une méthode pour augmenter la quantité de délai de groupe en utilisant des phaseurs réfléchissants passifs.

Un phaseur passif et passe-tout (qui ne filtre aucune fréquence) affiche une perte qui est proportionnelle au retard de groupe, ce qui entraîne une distorsion du signal. Le chapitre trois présente une solution à ce problème, qui consiste en une mise en cascade d'un phaseur ayant du gain et un phaseur ayant des pertes. Des phaseurs ayant du gain (G) ou des pertes ($L = 1/G$) ont des amplitudes symétriques par rapport à une amplitude de 0 dB, et des retards de groupe identiques. Le signal à la sortie d'une paire de ces phaseurs a une amplitude constante. En outre, le retard de groupe peut être réglé par le contrôle du gain et des pertes. Le

chapitre trois présente ce concept, présente mathématiquement la modélisation des appareils et a présente des résultats expérimentaux.

La radio à impulsion UWB (IR-UWB) pour la communication sans fil permet des designs d'émetteurs-récepteurs très simples et peu coûteux. En effet, l'émetteur ne nécessite pas de porteuse et le récepteur est non cohérent. Pour améliorer l'efficacité du spectre de la communication IR-UWB, une technique d'accès multiple doit être utilisée. D'une manière conventionnelle, on utilise une technique de sauts temporels avec un accès multiple basé sur un traitement de signal numérique. Cette technique occasionne une latence de l'ordre la milliseconde, ce qui est trop élevé pour répondre à la communication future (par exemple, la technologie 5G), qui requiert une latence de l'ordre des nanosecondes. Les phaseurs traitent le signal IR-UWB avec un délai de propagation électromagnétique de l'ordre de la nanoseconde, et peuvent donc être la solution pour le traitement des signaux de communication IR-UWB. En exploitant la diversité des profils de retard de groupe pour un codage à accès multiple, nous introduisons un code à dispersion multiple (DCMA), une technique de codage en temps réel efficace pour la communication IR-UWB haute vitesse. Le chapitre 4 introduit le concept de DCMA, présente un critère de sélection de codage, et présente la démonstration expérimentale du système DCMA.

Ensuite, pour éviter de caractériser expérimentalement le système DCMA, qui est assez complexe, le chapitre 5 caractérise de manière analytique le système DCMA en termes de robustesse, d'interférence à accès multiple, de rapport signal à interférence et de probabilité d'erreur de bit. La section 5.1 caractérise un canal sans fil à ligne de mire (LOS). Pour le canal qui n'est pas en ligne de mire (NLOS), un mécanisme de compensation supplémentaire pour la dispersion des canaux est nécessaire. De plus, la commutation dynamique entre les différentes paires de communication nécessite une adaptation. La section 5.2 propose et caractérise un schéma de routage dynamique basé sur l'inversion de temps pour le canal NLOS.

Enfin, le chapitre 6 conclut le travail de la thèse, souligne la limitation de la modulation IR-UWB, et recommande l'approche par accès multiple à spectre étalé en temps réel en utilisant un milieu spatio-temporel, qui offre un schéma de modulation ayant une largeur de bande inférieure pour la même quantité de données.

ABSTRACT

We are facing exploding demands for faster, more reliable, more energy-efficient radio systems, such as for instance 5G wireless communication. It is expected that for the next decade the mobile data capacity would exceed 1000 times higher than it is right now. Such high data volume requires large bandwidth spectrum resources. In low RF frequencies, the precious spectrum have been congested by zillions of radio devices. In high frequencies, such as millimeter wave, ultra wideband (UWB) spectrum is much easier available. However, processing UWB RF signal poses great difficulties on conventional digital signal processing (DSP) technique that has prevailed for low frequency and small bandwidth processing. For instance, DSP suffers limited speed, high cost and high power consumption for analog/digital conversion (ADC). Therefore, real-time and purely analog processing technique is desirable. In optics, people have been processing UWB RF signal with microwave photonics approaches, which is real-time, but involves expensive and lossy electrical/optical conversion. The direct radio Real-time Analog Signal Processing (R-ASP) is thus attractive but less exploited. Chapter 1 presents the advancements of R-ASP along with the contributions of the thesis.

The core of R-ASP is "phaser", which is a group delay engineered component that provides specified group delay function $\tau(\omega)$. A phaser, in response to a wideband signal excitation, rearranges spectral components in time. The way a phaser arranges spectral components is controlled by the group delay function, $\tau(\omega)$. Different R-ASP applications may require different group delay profiles. Chapter 2 introduces the concept of group delay engineering, different phaser technologies, and presents an R-ASP resolution (group delay swing) enhancement example using passive reflective phaser units.

Passive phaser exhibits loss that is proportional to the group delay, i.e. imbalance amplitude, which typically results in undesired processing distortion. It is found that a phaser unit loaded with gain (G) and another loaded with equalized loss ($L = 1/G$) provide symmetric amplitudes (about 0 dB) and identical group delays. Cascading such gain and loss pair yields real all-pass amplitude. Moreover, the group delay can be tuned by the gain and loss. Chapter 3 introduces the gain-loss equalization concept, mathematically presents the device modeling, and experimentally demonstrated the prototype.

Impulse radio UWB (IR-UWB) wireless communication allows very simple and low-cost transceiver design, e.g. carrier-less transmitter and non-coherent receiver. To enhance the spectrum efficiency of IR-UWB communication, a multiple access technique has to be employed. Conventionally, time hopping multiple access based on DSP is used, whose latency

is too high (millisecond order) to meet the future communication (e.g. 5G and internet of things) requirement (nanosecond order). Phaser processes IR-UWB signal with negligible electromagnetic propagation delay (nanosecond order), thus may be the solution for future communications. By exploiting the diversity of group delay profiles, we propose the dispersion code multiple access (DCMA) as an efficient real-time multiple access coding technique for high-speed communication. Chapter 4 introduces the DCMA concept, presents coding selection criterion, demonstrates the proof-of-concept DCMA experimental system.

Then, to avoid experimentally characterizing DCMA system for many simultaneous users, which is very involved, Chapter 5 analytically characterizes DCMA system in terms of robustness, multiple access interference (MAI), signal to interference ratio (SIR) and bit error probability (BEP). Section 5.1 characterizes for line-of-sight (LOS) wireless channel. For non-line-of-sight (NLOS) channel, additional compensation mechanism for the channel dispersion is required. Moreover, dynamic switching between different communication pair requires adaptivity. Section 5.2 proposes and characterizes time-reversal based dynamic routing scheme for NLOS channel.

Finally, Chapter 6 summarizes the work of the thesis, suggests miscellaneous topics for future works, specifically points out the limitation of IR-UWB modulation schemes, and recommends a real-time spread spectrum multiple access approach using space-time metamaterial, so as to accommodate higher spectrum-efficiency modulation schemes.

TABLE OF CONTENTS

LIST OF TABLES

LIST OF FIGURES

LIST OF SYMBOLS AND ABBREVIATIONS

Abbreviations

5G	5th Generation
ADC	Analog-Digital Converter
BEP	Bit Error Probability
BPSK	Binary Phase Shift Keying
CDMA	Code Division Multiple Access
CRLH	Composite Right/Left-Handed
DCMA	Dispersion Code Multiple Access
DSBP	Delay Swing Bandwidth Product
DSP	Digital Signal Processing
EBG	Electromagnetic BandGap
FBG	Fiber Bragg Grating
IR	Impulse Radio
LOS	Line of Sight
LPDA	Log-Periodic Dipole Array
MAI	Multiple Access Interference
NLOS	Non Line of Sight
OFDM	Orthogonal Frequency Division Modulation
OFDMA	Orthogonal Frequency Division Multiple Access
OOK	On Off Keying
PCB	Printed Circuit Board
PDF	Probability Density Function
PPM	Pulse Position Modulation
QPSK	Quadrature Phase Shift Keying
R-ASP	Real-time Analog Signal Processing
RF	Radio Frequency
RFID	Radio Frequency Identification
SAW	Surface Acoustic Wave
SNR	Signal to Noise Ratio
SINR	Signal to Interference and Noise Ratio
SIR	Signal to Interference Ratio
SPDT	Single Pole Double Throw

SRD	Step Recovery Diode
ST	Space-Time
TEM	Transverse ElectroMagnetic
TR	Time Reversal
UWB	Ultra Wideband

Symbols

c	speed of light in vacuum 3×10^8 m/s
ϵ_0	permittivity of vacuum 8.85×10^{-12} F/m
μ_0	permeability of vacuum $4\pi \times 10^{-7}$ H
ϵ_r	relative permittivity of a medium
k_0	free space wave number
k	Boltzmann constant 1.38×10^{-23} J/K
λ	wavelength
γ	propagation constant $\gamma = \beta - j\alpha$
β	propagation phase constant
α	propagation attenuation constant
$\Delta\tau$	group delay swing
$\mathcal{P}$	time bandwidth product
ρ	standing wave ratio

LIST OF APPENDIXES

CHAPTER 1 INTRODUCTION

1.1 Motivation

Today we are facing exploding demands for faster, more energy-efficient, and more scalable radio techniques for wireless communications, which currently are mostly narrow-bandwidth. People have squeezed the precious radio spectrum resources to push the channel capacity towards the Shannon limit [19], yet hardly meet the fast growing needs for massive data applications. It is expected that the mobile capacity would be increased by 1000 times for the next decade [20]. To achieve such high data traffic volume, people may naturally resort to large spectrum resources, i.e. ultra wideband (UWB), which are easier available in millimeter wave and terahertz regime than today's low-frequency communication bands. Unfortunately, however, current low-frequency and small-bandwidth signal processing techniques are incompetent to manipulate the high-frequency and large-bandwidth signals [21]. The digital signal processing (DSP) technique has prevailed in wireless communications for a long time due to the high flexibility and easy integration. However, DSP is not without its drawbacks, its cost and power consumption scale with increased processing frequency and bandwidth [22], hence inhibiting high-frequency and UWB applications. Therefore, more efficient high-frequency UWB signal processing paradigm are highly desirable.

In optical regime, scientists and engineers have been using analog dispersive structures, such as fiber Bragg grating, ring resonator, etc, to efficiently process electromagnetic pulses with ultra-short duration and hence huge bandwidth in real time [9, 13, 23–25], Reported optical analog signal signal processing (O-ASP) systems include Fourier transformer [26–28], time-stretched digitizer [29], optical integrator [30], differentiator [31], convolver [32], Hilbert transformer [33,34], fiber Bragg grating based real-time code division multiple access (CDMA) [35, 36], etc.

The real time feature of O-ASP leads to low-latency and high-speed signal transmission. Given the advantages of O-ASP, a lot of efforts have been done to apply it to radio signal processing via microwave photonics approaches [37–43]. However, microwave photonics typically involves lossy, expensive and non-integrable optoelectronic components for frequency conversion betweens RF and optical. Thus direct analog signal processing at radio frequency and corresponding applications, which are less exploited, is an attractive area and will be the research topic of this thesis.

1.2 Radio Real-Time Analog Signal Processing (R-ASP)

Radio real-time analog signal processing (R-ASP) consists in processing RF UWB signals in real time using dispersive electromagnetic structure, which has been given the name "phaser" [6, 44] and, as the name suggests, manipulates the phase or the group delay of the input signals. As the core of R-ASP, an *ideal* phaser, is typically engineered to provide a frequency-independent transfer magnitude over certain bandwidth, i.e. $|H(\omega)| = 1$, $\omega \in [\omega_1, \omega_2]$, and a specified frequency-dependent group delay function that is the negative derivative of the transfer phase with respect to angular frequency, i.e. $\tau(\omega) = -\partial\phi/\partial\omega$. Consequently, an ultra-short pulse with no chirping, i.e. being transform-limited [23], travelling through a phaser experiences rearrangement of spectral components in time and corresponding *intended* signal distortions.

Various RF phaser technologies have been reported, including surface acoustic wave structure [7], electromagnetic bandgap (EBG) structure [10, 45–47], composite right/left-handed (CRLH) metamaterial structures [8, 48], coupled-resonator based narrowband structure [11] [14], all-pass (broadband) structures [1, 12, 44, 49–57], active structures [58, 59]. Each technology has its own advantages and disadvantages, which will be compared comprehensively in Chapter 2

Thanks to RF phaser technologies, a lot of promising R-ASP applications have been demonstrated, such as, for instance, Fourier transformation [10, 60, 61], spectrogram analysis [62], spectrum sniffing [5], Nth-order differentiation [63], UWB pulse shaping [64], arbitrary bean frequency scanning [65], dispersion compensation in log periodic antenna [66], time expansion for enhanced sampling [67, 68], and time reversal [69, 70]. Moreover, phasers have been used as encoder/decoder or modulator/demodulator in wireless communications, such as pulse position modulator [71], ramp-less compressive receiver [72], source-less frequency division multiplexing receiver [73], dispersion-modulation based signal-to-noise ratio enhanced transceiver [74, 75], dispersion coding RFID system [76, 77], and dispersion code multiple access (DCMA) wireless communication system [78–80], to name a few.

1.3 Thesis Major Contributions

The thesis mainly contributes to two aspects of R-ASP : a) development of novel phasers for enhanced dispersion (group delay swing) or for balanced amplitude and reconfigurable group delay, and development of a novel UWB pulse generator with simple topology and pulse width reconfigurability, b) application of R-ASP technologies to wireless communications. Next, we introduce the contributions and corresponding publications.

1.3.1 Phaser and UWB Pulse Generator Technologies

Group Delay Swing Enhanced Passive Phaser

Ideally, a phaser exhibits 1) specified group delay, 2) flat amplitude that is independent of the group delay, over the desired bandwidth. The dispersion capability, measured by the group delay swing $\Delta\tau = \tau_{\max} - \tau_{\min}$, represents the capability of phaser to resolve different frequency components in time [6]. Different all-pass phasers exhibit different dispersion capabilities ($\Delta\tau$). For example, the group delay swing of C-section is proportional (non-linearly) to the coupling factor k of its constituent coupler, whose enhancement is therefore constrained by the tolerance of photolithography fabrication process [12]. To conquer the limit, we proposed an passive phaser whose group delay swing is proportional to the reflection coefficient of its coupling aperture, thus relaxing the fabrication constraint. Chapter 2 presents the proposed passive group delay enhanced phaser in Sec. 2.4, corresponding to publication [1], along with introduction to the group delay engineering concept and to different existing passive phaser technologies.

Real All-Pass Group Delay Reconfigurable Phaser

In practice, passive phasers deviate from the ideal case where the transfer amplitude is frequency independent [$|H(\omega)| = 1, \omega \in [\omega_1, \omega_2]$], and the actual loss is proportional to the amount of group delay [81]. People may naturally resort to active devices to combat the loss. The reported active phasers in [58, 59] exhibit amplitudes that are strongly frequency-dependent. Such amplitude imbalance over frequency would cause undesired signal distortion [6]. Moreover, conventional passive phasers exhibit fixed group delay swing ($\Delta\tau$) and group delay profile [$\tau(\omega)$]. In practice, however, there are occasions where group delay swing and profile are required to be reconfigurable in order to adapt to dynamic environment. Despite all the references on phaser given in the previous section, no one has ever addressed these problems in one shot. Chapter 3 fills the gap by presenting a novel gain-loss equalized phaser, corresponding to publication [15].

Low-Cost, Duration Tunable UWB RF Pulse Generator

Phasers usually deal with ultrashort (typically picosecond) pulses with very rich spectral contents. Such pulses may be generated by different techniques [82]. Among them, the step recovery diode (SRD) approach [2,3,83] features simple circuit design, while offering picosecond pulse generation capability. Conventional SRD-based pulse generators usually employ an SRD to generate a picosecond rising edge pulse. This pulse then destructively interferes

with an opposite-polarity delayed replica of it produced by a short-circuited stub, resulting in a short pulse with duration equal to the round trip time along the stub. However, the stub configuration suffers from spurious reflections, which together with SRD mismatch induce ringing in the output waveform. The suppression of stub reflection requires a pulse shaping network [3], and pulse width tuning requires complicated tuning schemes [84]. Chapter 4 presents a stub-less pulse generator based on a pair of SRDs in Sec. 4.4.1, which provides flexible control of the pulse width via a simple resistance, corresponding to publication [4].

1.3.2 Application of R-ASP Technology to Wireless Communication

Dispersion Code Multiple Access (DCMA) Wireless Communication System

UWB communication provides high speed thanks to large spectrum resources available. To improve spectrum efficiency, some multiple access (MA) techniques have to be used. Conventionally, MA are done using digital signal processing, such as for instance code division multiple access (CDMA), orthogonal frequency division multiple access (OFDMA), etc [85], which typically exhibits high latency (millisecond range) and hence low speed, which cannot meet the future wireless communication standards like 5G. R-ASP provides unprecedented ultra low latency (nanosecond range) processing delay thanks to the analog nature of the processing core, phaser. Chapter 4 introduces the concept of DCMA as a purely analog MA technique based on R-ASP, experimentally demonstrates the proof-of-concept system, thus preliminarily proves the feasibility of the system, while Chapter 5 further characterizes the performance of DCMA system for line-of-sight (LOS) channel in Sec. 5.1, corresponding to publication [79].

Dynamic Routing of DCMA in Non-Line-of-Sight (NLOS) Channel Using Time Reversal

The proposed DCMA system is fixed, without capability of switching between different communication users. To address this issue and enable dynamic routing for DCMA, time reversal technique is employed, which introduces a base station or router with time-reversal mechanism, while maintains the simplicity of the access point transceiver design. Moreover, the self-adaptivity of time reversal technique allows automatic dispersion compensation for practical NLOS channels. Chapter 5 introduces and characterizes the time-reversal DCMA system for NLOS channels in Sec. 5.2, corresponding to publication [18].

CHAPTER 2 GROUP DELAY ENGINEERING USING PASSIVE PHASER

This chapter introduces the essentials of group delay engineering and passive phaser. Section 2.1 presents the group delay engineering concept, then, Sec. 2.2 comprehensively compares different passive phaser technologies, next, Sec. 2.3 presents the signal flow graph technique as an efficient tool for phaser analysis, finally, Sec. 2.4 presents group delay swing enhancement based on reflective-type phaser (excerpt from [1]).

2.1 Group Delay Engineering

Given a phaser, the corresponding transfer function is

$$H(\omega) = A(\omega)e^{j\phi(\omega)}, \quad \omega \in [\omega_0 - \Delta\omega/2, \omega_0 + \Delta\omega/2], \tag{2.1}$$

where ω_0 and $\Delta\omega$ are the center angular frequency and bandwidth, respectively, $A(\omega)$ and $\phi(\omega)$, being real functions, are the amplitude response the phase response, respectively. Ideally, $A(\omega) = 1$ over the bandwidth, while in a small frequency range around $\omega' \in [\omega_0 - \Delta\omega/2, \omega_0 + \Delta\omega/2]$, $\phi(\omega)$ may be approximated by the Taylor expansion [23, 86], corresponding to

$$\phi(\omega) = \phi_0 + \phi_1(\omega - \omega') + \frac{\phi_2}{2}(\omega - \omega')^2 + \ldots + \frac{\phi_n}{n!}(\omega - \omega')^n + \ldots, \text{ with } \phi_n = \left.\frac{d^n\phi}{d\omega^n}\right|_{\omega=\omega'}. \tag{2.2}$$

Taking negative derivative of (2.2) leads to the group delay

$$\tau(\omega) = -\frac{\partial\phi}{\partial\omega} = \tau' + \sigma(\omega - \omega') + \ldots - \frac{\phi_n}{(n-1)!}(\omega - \omega')^{n-1} + \ldots, \tag{2.3}$$

where $\tau' = \tau(\omega') = -\phi_1$ is the group delay at ω', $\sigma = -\phi_2$ is the group delay slope around ω'. If the coefficients of all the non-linear terms in (2.2) are zero, i.e. $\phi_n = 0, \ \forall\, n \geqslant 2$, Eq. (2.3) reduces to $\tau(\omega) = \tau'$ and thus becomes frequency independent around ω', i.e. non-dispersive, otherwise, when $\phi_n \neq 0$ for any $n \geqslant 2$, Eq. (2.3) is frequency dependent, i.e. dispersive.

Different applications require different group delay profiles, hence different coefficients. For instance, real-time Fourier transformation employs linear group delay, i.e. $\phi_n = 0, \forall\, n \geqslant 3$ [10, 60, 61] . The Arbitrary bean scanning in antenna array [65] and dispersion compensation in log periodic antenna [66] are based on some non-linear group delay curve, i.e. $\phi_n \neq 0$ for some $n \geqslant 3$. The dispersion code multiple access (DCMA) involves a group delay set with diversified

profiles [79]. The success of various R-ASP applications, therefore, lies in engineering arbitrary specified group delay, and the corresponding process is referred to *group delay engineering*. Figure 2.1 illustrates two group delay engineering examples, namely linear and stair cases. The linear case in Fig. 2.1(a) is typically seen in real-time Fourier transformer [10, 60, 61], pulse compression radar [87–89], etc, the latter stair case in Fig. 2.1(b) has been recently proposed for spectrum sniffing [5].

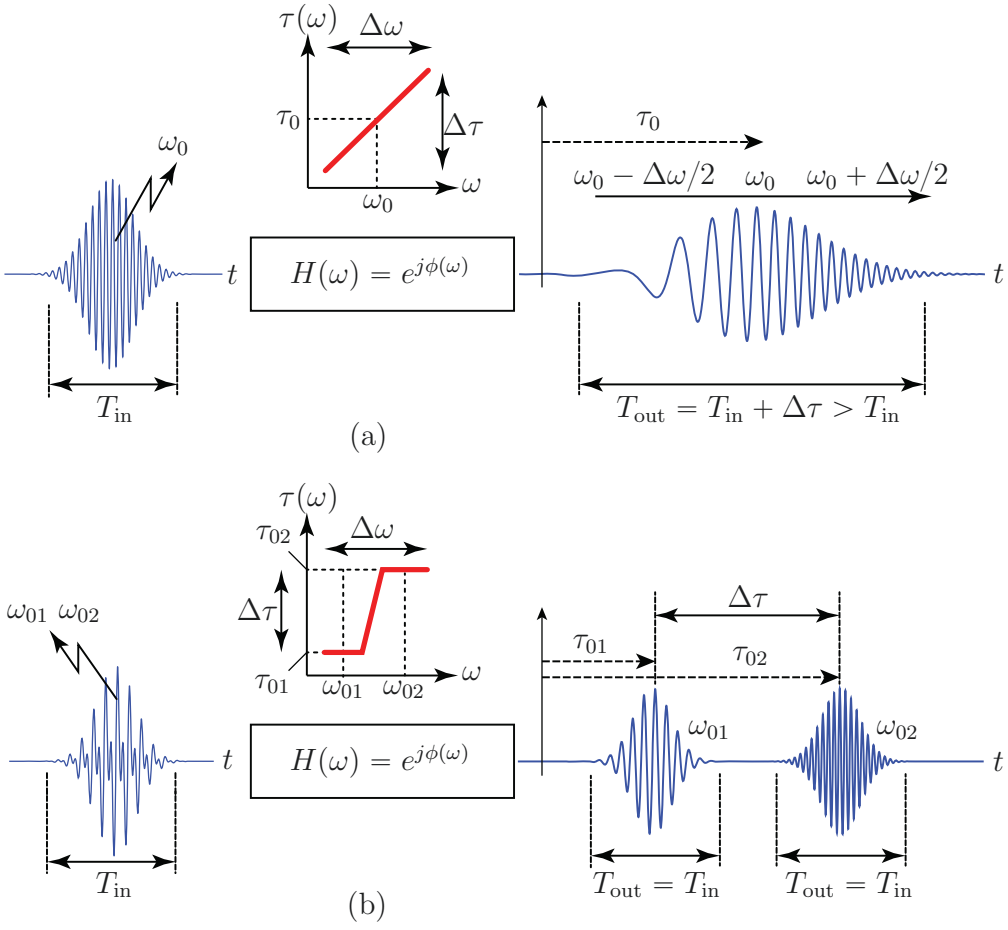

Figure 2.1 Illustration of two group delay engineering examples. (a) Linear group delay with time spread ($T_{\text{out}} > T_{\text{in}}$). (b) Frequency discrimination [5] in time with each output pulse not dispersed ($T_{\text{out}} = T_{\text{in}}$). (C. Caloz, et al [6], Microwave Magazine, ©2013 IEEE)

An important figure of merit of group delay function is the dispersion capability, measured by the group delay swing $\Delta\tau = \tau_{\max} - \tau_{\min}$. $\Delta\tau$ represents the R-ASP resolution, which is the capability of phaser to resolve different frequency components in time [6]. We will show later in Sec. 2.3 that different passive phasers have different dispersion capability. Another figure of merit is time bandwidth product, which is the integral of group delay function over

the bandwidth as

$$\mathcal{P} = \int_{\Delta\omega} \tau(\omega')\, d\omega' = \text{const.}, \tag{2.4}$$

and is a constant for a given phaser [6, 44]. Large $\mathcal{P}$ is desirable for some applications, such as for instance the DCMA communications [79], where increasing $\mathcal{P}$ improves signal to interference ratio and hence lower bit error probability.

2.2 Passive Phaser Technologies

The group delay engineered component, which is called phaser, can be realized in various technologies. Figure 2.2 shows a few typical phasers, part of which are excerpted from [6]. The surface acoustic wave (SAW) structure [Fig. 2.2(a)] is electromechanical device commonly

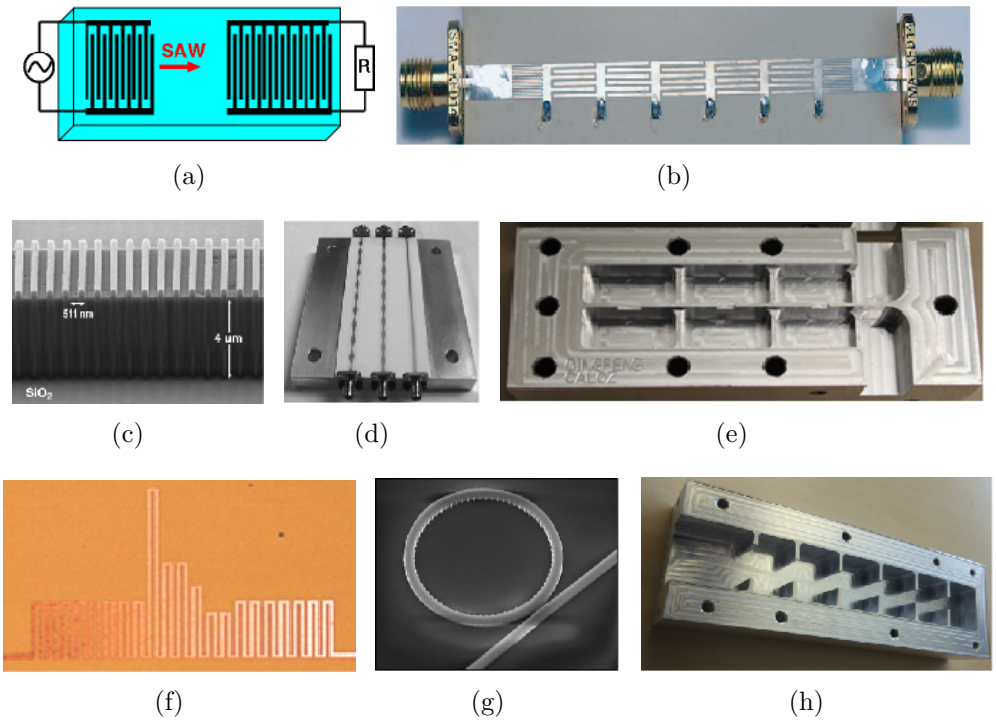

Figure 2.2 Different phaser technologies. (a) Surface acoustic wave (SAW) structure [7]. (b) Metal-insulator-metal (MIM) composite right/left-handed (CRLH) metamaterial structure [8]. (c) Fiber Bragg grating [9]. (d) Electromagnetic bandgap structure [10]. (e) Cross coupled resonator structure [11]. (f) Cascaded C-section structure [12]. (g) Single ring resonator [13]. (h) Reflection-type cascaded coupled resonator structure [14]. (C. Caloz, et al [6], Microwave Magazine, ©2013 IEEE)

seen in applications such as pulse-compression radar [90–92]. The electrical signals applied to a SAW delay line are converted into a mechanical wave on a piezoelectric substrate where

the wave amplitude decays exponentially deep into the substrate (surface wave) and the wave is delayed. At the output, the mechanical wave is again converted back into electrical signal by electrodes [7, 88, 89]. Due to the slow-wave nature, SAW delay line typically provides large group delay in compact size. However, the operation frequency is typically limited below 3 GHz. The metamaterial dispersion and applications have been studied [93, 94]. Figure 2.2(b) shows a CRLH metamaterial transmission line phaser [71, 72], which is a periodic structure whose bandwidth is constrained by broadband Bloch impedance matching and size is much larger than SAW delay lines. The CRLH phaser typically exhibits hyperbolic phase response [8], thus restricted dispersion engineering flexibility. The fiber Bragg grating (FBG) [Fig. 2.2(c)] and electromagnetic bandgap (EBG) structures [Fig. 2.2(d)] are both bandgap structures. They consist in varying the refractive index or characteristic impedance with certain pattern along the transmission line, so as to create bandgaps for different frequencies at different positions along the transmission line [9, 10]. Each bandgap reflects correpsonding frequency component with delay amount that is equal to the corresponding round trip time. A drawback of bandgap structures is that they are excessively long (usually a lot of wavelengths) and thus too bulky for integration. Moreover, the group delay response typically exhibits undesired ripples due to multiple internal reflection [45]. Figure 2.2(e) shows a phaser based on cross-coupled resonator technology, where the filter coupling matrix has been synthesized for the group delay response [11,95–97]. The fractional bandwidth of the synthesized phaser is narrow (typically $< 5\%$) due to strong frequency dependence of the coupling mechanism. The last row shows three all-pass phasers, namely C-section phaser [Fig. 2.2(f)], ring resonator phaser [Fig. 2.2(g)] and reflective cascaded-coupled resonator phaser [Fig. 2.2(h)], all of which ideally provide frequency-independent amplitude (for lossless case) and specified group delay. We will focus on all-pass phaser in the rest of the chapter, due to its independent control capability of amplitude (flat for lossless case) and group delay.

2.3 Signal Flow Graph Technique

This section introduces signal flow graph technique as an efficient and insightful approach for phaser analysis, and then analyzes examples of all-pass phasers corresponding to Fig. 2.2(f), (g) and (h), and finally finds their group delay swing determinant factor. For simplicity, we assume first-order all-pass phasers that are lossless and support TEM wave propagation.

Figure 2.3 shows schematics for the first-order all-pass phasers, with corresponding parameters indicated. Figure 2.4 shows their corresponding signal flow graphs, where only port 1 is excited. By inspecting the signal flow graphs, one may easily find similarity between the graphs : 1) all graphs include a direct path from node 1 to node 2, with coefficient B, T or

R in Figs 2.4(a), (b) or (c), respectively ; 2) all graphs include another path with feedback loop whose feedback coefficient is equal to that of the direct path in 1).

It is the feedback loop that causes the energy storage and hence group delay swing (dispersion). Therefore, the stronger the feedback, the higher the group delay swing is. For instance, in the C-section graph [Fig. 2.4(a)], the feedback is due to the coupler backward coupling (B), i.e. the group delay swing is proportional (nonlinearly) to B [12]. In the ring resonator graph [Fig. 2.4(b)], the feedback is due to the coupler through transmission coefficient (T), i.e. the group delay swing is proportional to T, or inversely proportional to B since $|B|^2 = 1 - |T|^2$ [57]. In the reflective coupled resonator graph [Fig. 2.4(c)], the feedback is due to the local reflection (R) of the coupling mechanism, i.e. the group delay swing is proportional to R [1]. Note that we have assumed ideal TEM propagation here, leading to the condition $|B|^2 + |T|^2 = 1$, i.e. zero parasitic effects (coupler forward coupling and reflection), for the four-port coupled-line coupler used in C-section and ring resonator. However, in practice, due to the imperfect TEM wave in coupler, there may exist innegligible parasitic effects, which create undesired wave paths that are not taken into account in Figs 2.4(a) and (b). The reflective resonator is immune to the parasitic effects, because it is based on a coupling mechanism that is only two-port.

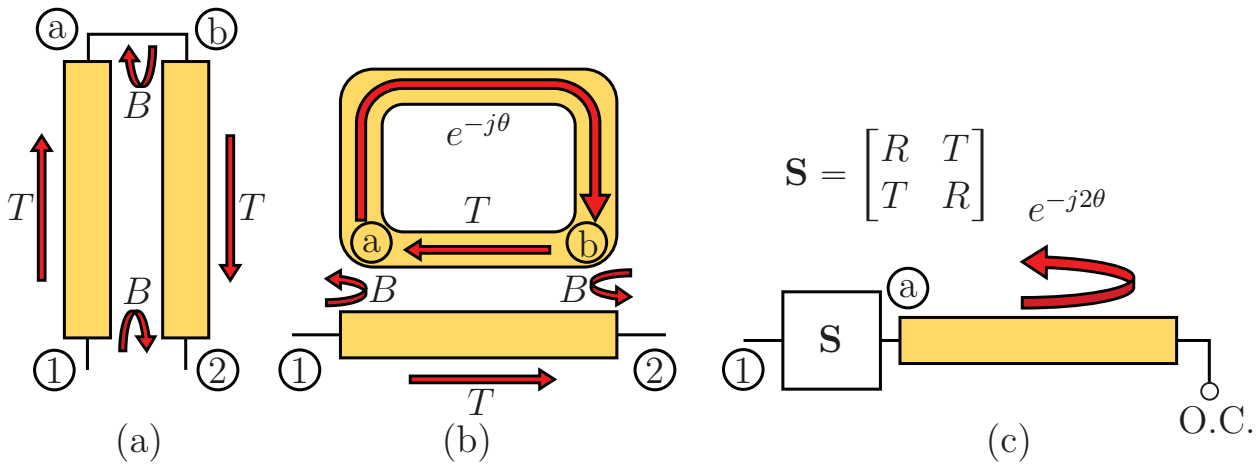

Figure 2.3 Schematics for first-order all-pass phasers. (a) C-section corresponding to Fig. 2.2(f) with a short at one end, and T and B are the coupler through and backward coupling coefficients, respectively. (b) Ring resonator corresponding to Fig. 2.2(g) with one of the coupled lines enclosed by an isolated transmission line with electrical length θ. (c) Reflective coupled resonator corresponding to one of the sections in Fig. 2.2(h), with an open stub with electrical length θ and a coupling mechanism characterized by scattering parameters $\mathbf{S}$, where R and T are the local reflection and transmission coefficients, respectively.

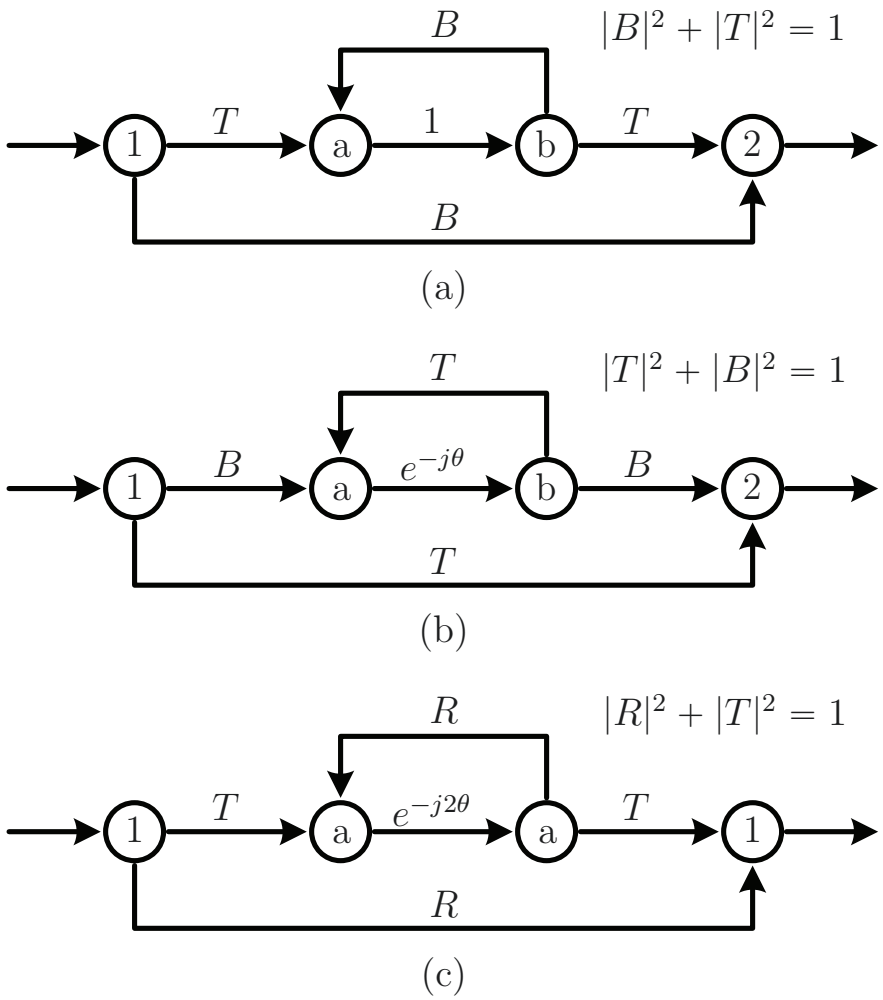

Figure 2.4 Signal flow graphs corresponding to the phasers in Fig. 2.3. (a) Signal flow graph for the C-section in Fig. 2.3(a). (b) Signal flow graph for the ring resonator in Fig. 2.3(b). (c) Signal flow graph for the reflective resonator in Fig. 2.3(c).

2.4 Group Delay Swing Enhancement with Reflective Resonator

The important figure of merit of phaser is group delay swing, $\Delta\tau = \tau_{\max} - \tau_{\min}$. As mentioned before, the passive C-section group delay swing is proportional to the the backward coupling. Unfortunately, the achievable coupling value, and thus the group delay swing, is typically limited by the tolerance of photolithographical PCB fabrication process. However, this would not be the case for passive ring resonator and reflective resonator, whose group delays are proportional to the coupler through transmission coefficient and the coupling mechanism reflection coefficient, respectively, hence greatly relaxing the fabrication constraint. Moreover, considering reflective resonator's immunity to parasitic effects, such as coupler forward cou-

pling, due to its tow-port nature, we will now present a phaser based on reflective resonator with group delay swing enhancement compared to C-section phaser. Some of the following materials are excerpt from [1].

2.4.1 Characterization of Reflective Coupled Resonator

The coupling mechanism in Fig. 2.3(c) may be a strip gap for a planar structure or a coupling aperture for a metallic waveguide, which is passive, lossless and reciprocal, and can be modeled by a scattering matrix of the form

$$\mathbf{S} = \begin{bmatrix} |R| & j|T| \\ j|T| & |R| \end{bmatrix}, \quad \text{with} \quad |R|^2 + |T|^2 = 1. \tag{2.5}$$

Assuming an unity excitation, one may obtain the overall scattering parameter (S_{11}) by adding up all the multiple scattering output waves, corresponding to

$$S_{11} = R + Te^{-j2\theta}T + Te^{-j2\theta}Re^{-j2\theta}T + Te^{-j2\theta}Re^{-j2\theta}Re^{-j2\theta}T \ldots = R + \frac{T^2e^{-j2\theta}}{1 - Re^{-j2\theta}}. \tag{2.6}$$

where $\theta = \pi\omega/\omega_0$ is the electrical length of the open stub at ω, which at the center frequency ω_0 is π. Performing mathematical manipulations (2.6), reduces to

$$S_{11}(\omega) = \frac{1 - j\rho\tan(\pi\omega/\omega_0)}{1 + j\rho\tan(\pi\omega/\omega_0)}, \tag{2.7a}$$

with

$$\rho = \frac{1 + |R|}{1 - |R|} \tag{2.7b}$$

identified as the local standing wave ratio of the coupling mechanism. The corresponding group delay is obtained by taking the phase derivative of (2.7a), leading to

$$\tau(\omega) = \frac{\rho T_0}{(\rho^2 - 1)\sin^2(\pi\omega/\omega_0) + 1}, \tag{2.8}$$

with $T_0 = 1/f_0$ being the period at $\omega_0 = 2\pi f_0$. The corresponding group delay swing is

$$\Delta\tau = \tau_{\max} - \tau_{\min} = \tau|_{\omega=n\omega_0} - \tau|_{\omega=(2n-1)\omega_0/2} = \frac{4|R|T_0}{(1 + |R|)(1 - |R|)}, \tag{2.9}$$

which is indeed proportional (nonlinearly) to the reflection coefficient. Since a high reflection coefficient is easier to achieve than high coupling in C-section, the reflective resonator

(RR) phaser practically provides higher group delay swing than its C-section counterpart. Figure 2.5 plots (2.8) for different R, the non-dispersive case ($|R| = 0$) corresponds to a flat group delay. As $|R|$ increases, the delay decreases at anti-resonance frequencies $(n + 0.5)\omega_0$ ($n \in \mathbb{Z}$), while increases quickly with increased $|R|$ at resonance frequencies $n\omega_0$, thus further confirming the group delay swing proportional to $|R|$. Also note that, as the group delay swing ($\Delta\tau$) increases, the bandwidth decreases, due to the constant time bandwidth product [Eq. (2.4)] nature. To broaden the bandwidth, one may cascade a few such resonators tuned at different resonance frequencies. However, cascading one port reflective resonators requires additional effort to transform the one-port network to two-port, as will be shown in Sec. 2.4.3.

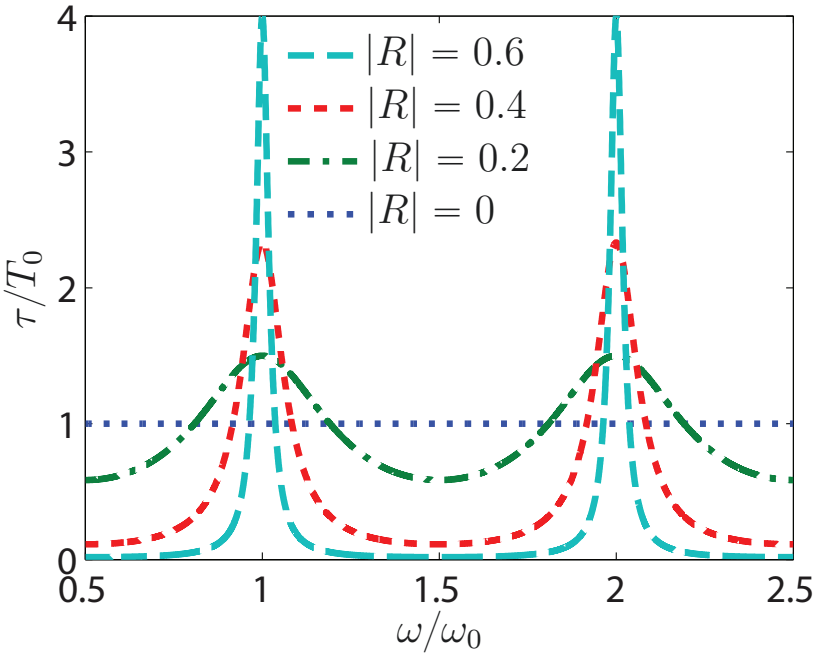

Figure 2.5 Normalized group delay τ/T_0 versus frequency ω/ω_0 computed using (2.8) for different reflection coefficients R's.

2.4.2 Physical Realization and Modeling of Reflective Resonator (RR) Phaser

A possible physical implementation of the reflective resonator [Fig. 2.3(c)] in planar circuit technology along with its equivalent model are presented in Figs 2.6(a) and (b), respectively. This is a half-wavelength (at ω_0) resonator fed by a quater-wavelength capacitive coupled-line coupling mechanism [98]. Around odd multiple of ω_0 [$\omega \approx (2n - 1)\omega_0$], Fig. 2.6(a) is equivalent to Fig. 2.6(b), which is identical to the reflective resonator in Fig. 2.3(c) with an additional phase shift by the leftmost transmission line shown in Fig. 2.6(b). The group

delay response of Fig. 2.6(a) differs from that of Fig. 2.3(c) in that, instead of exhibiting group delay maxima at all the multiples of ω_0 [$\tau_{\max} = \tau|_{\omega=n\omega_0}$ in Fig. 2.5], it exhibits them only at the odd multiples of ω_0 [$\tau_{\max} = \tau|_{\omega=(2n-1)\omega_0}$].

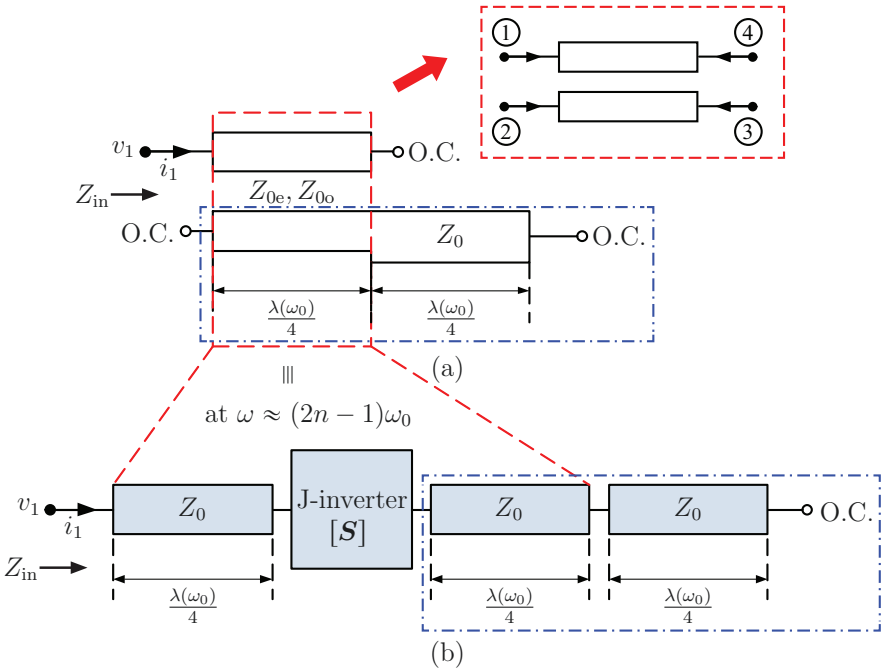

Figure 2.6 Coupled-line implementation of the constituent reflective resonator in Fig. 2.3(c). (a) Physical configuration. (b) Equivalent transmission-line model with the coupling mechanism modeled by a J-inverter with scattering parameters **S**.

We shall now model the circuit in Fig. 2.6(a). Note that the coupled-line coupler section performs the admittance inverter (J-inverter) function, while the bottom half-wavelength stepped-impedance line performs the resonator function.

A J-inverter may be modeled by its ABCD matrix, as [98]

$$\begin{bmatrix} A & B \\ C & D \end{bmatrix} = \begin{bmatrix} 0 & j1/J \\ jJ & 0 \end{bmatrix}. \tag{2.10}$$

Transforming (2.10) into its scattering parameters using standard network conversion formulas [98], and equating the corresponding scattering parameters to (2.5) yields the matched-output reflection coefficient (local reflection coefficient)

$$R = \frac{1-(JZ_0)^2}{1+(JZ_0)^2}. \tag{2.11}$$

Solving (2.11) for J leads to

$$J = \frac{1}{Z_0\sqrt{\rho}}, \tag{2.12}$$

with ρ given by (2.7b).

The equivalence shown in Fig. 2.6 holds in the vicinity of odd multiples of the first resonance, ω_0, where the coupler even and odd impedances, Z_{0e} and Z_{0o}, are expressed as [98]

$$z_{0e} = \frac{Z_{0e}}{Z_0} = 1 + JZ_0 + (JZ_0)^2 = 1 + \frac{1}{\sqrt{\rho}} + \frac{1}{\rho}, \tag{2.13a}$$

$$z_{0o} = \frac{Z_{0o}}{Z_0} = 1 - JZ_0 + (JZ_0)^2 = 1 - \frac{1}{\sqrt{\rho}} + \frac{1}{\rho}, \tag{2.13b}$$

respectively, where Z_0 is the system impedance, J is admittance inversion factor, and (2.12) was used to obtain the last expressions.

The goal is now to find the input impedance z_in, and hence the reflection coefficient of the coupled-line RT phaser to find its group delay characteristics. First, the four-port normalized impedance matrix for the coupled-line coupler shown in Fig. 2.6 is expressed in terms of the even and odd impedances as [98]

$$z_{11} = z_{22} = z_{33} = z_{44} = \frac{-j}{2}(z_{0e} + z_{0o})\cot\theta, \tag{2.14a}$$

$$z_{12} = z_{21} = z_{34} = z_{43} = \frac{-j}{2}(z_{0e} - z_{0o})\cot\theta, \tag{2.14b}$$

$$z_{13} = z_{31} = z_{24} = z_{42} = \frac{-j}{2}(z_{0e} - z_{0o})\csc\theta, \tag{2.14c}$$

$$z_{14} = z_{41} = z_{23} = z_{32} = \frac{-j}{2}(z_{0e} + z_{0o})\csc\theta, \tag{2.14d}$$

where $\theta = \pi\omega/(2\omega_0)$ is the electrical length of the coupler at any frequency ω.

Next, the open-end boundary conditions at port 2 and 4 shown in Fig. 2.6(a) are applied to reduce the four-port impedance matrix (2.14) to the two-port matrix

$$[\mathbf{z}] = \begin{bmatrix} z_{11} & z_{13} \\ z_{31} & z_{33} \end{bmatrix}. \tag{2.15}$$

Finally, the boundary condition at port 3, which is the normalized input impedance of the

open-end quarter-wavelength transmission line in Fig. 2.6(a) and reads

$$z_{\mathrm{L3}} = -j\cot\theta = \frac{v_3}{i_3}. \tag{2.16}$$

The system formed by the (v_1, v_3) - (i_1, i_3) matrix equation associated with (2.15) plus (2.16) represents a system of three equations in the variables v_1, i_1, v_3, i_3. Eliminating v_3 and i_3, provides the input impedance for the system in Fig. 2.6(a),

$$z_{\mathrm{in}} = \frac{v_1}{i_1} = z_{11} - \frac{z_{13}^2}{z_{11} + z_{\mathrm{L3}}}. \tag{2.17}$$

Inserting (2.16), (2.14a) and (2.14c) with (2.13) into (2.17) leads to the corresponding reflection coefficient

$$S_{11} = \frac{z_{\mathrm{in}} - 1}{z_{\mathrm{in}} + 1} = \frac{\cot\theta\left(1 + \dfrac{1}{\rho} - \dfrac{1}{2\rho+1}\sec^2\theta\right) - j}{\cot\theta\left(1 + \dfrac{1}{\rho} - \dfrac{1}{2\rho+1}\sec^2\theta\right) + j}, \text{ with } \theta = \frac{\pi\omega}{2\omega_0}. \tag{2.18}$$

It is straightforwardly verified in (2.18) that the reflective resonator is also an all-pass, i.e. $|S_{11}(\omega)| \equiv 1 \ \forall\, \omega$.

The corresponding normalized group delay response can be obtained by taking derivative of $\angle S_{11}$ from (2.18), which yields

$$\overline{\tau}_{11} = -\frac{1}{T_0}\frac{\partial \angle S_{11}}{\partial \omega} = \frac{\csc^2\theta\left(1 + \dfrac{1}{\rho} - \dfrac{1}{2\rho+1}\sec^2\theta\cos 2\theta\right)}{2 + 2\cot^2\theta\left(1 + \dfrac{1}{\rho} - \dfrac{1}{2\rho+1}\sec^2\theta\right)^2}. \tag{2.19}$$

Since this RR phaser, represented in Fig. 2.6(a), and the C-section phaser shown in Fig. 2.3(a) are both implemented using coupled lines, their group delay responses can be compared in terms of same parameter, namely the backward coupling factor k. However, one must first establish the relationship between k and ρ for the RR phaser. This relation may be found by inserting (2.13) with (2.7b) into the well-known relation $k = (z_{0\mathrm{e}} - z_{0\mathrm{o}})/(z_{0\mathrm{e}} + z_{0\mathrm{o}})$, which yields

$$k = \frac{\sqrt{\rho}}{\rho + 1}, \tag{2.20}$$

or, solving (2.20) for ρ

$$\rho = \frac{\left(1+\sqrt{1-4k^2}\right)^2}{4k^2}. \tag{2.21}$$

For comparison, we write the normalized group delay function of C-section below [12]

$$\overline{\tau}_{21} = \frac{\tau_{21}}{T_0} = \frac{\kappa/2}{(\kappa^2-1)\sin^2\theta+1}, \text{ with } \kappa = \sqrt{\frac{1-k}{1+k}} \text{ and } \theta = \frac{\pi\omega}{2\omega_0}. \tag{2.22}$$

Figure 2.7 compares the group delay function of an RR phaser, computed using (2.19), with that of a C-section, computed using (2.22). Where the group delay swing of C-section is proportional (non-linearly) to k, while that of the RR phaser is inversely proportional to k, which is preferable since the coupling factor (k) is typically constrained by fabrication tolerance. Also note that the group delay maxima of RR phaser indeed only appear at odd multiple of the first resonance frequency $(2n-1)\omega_0$.

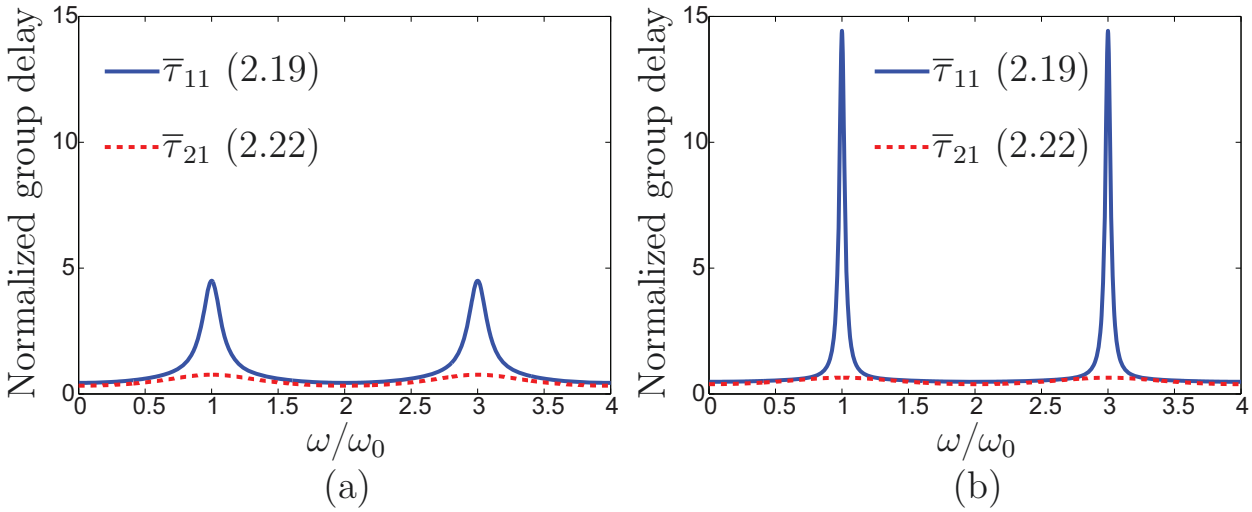

Figure 2.7 Comparison of group delays between RR phaser in Fig. 2.6(a) and C-section phaser in Fig. 2.3(a) for different coupling factors, (a) $k = 0.4$, (b) $k = 0.25$.

2.4.3 Experimental Demonstration of Group Delay Engineered RR Phaser

It was just shown that the RR phaser in Fig. 2.6(a) provides group delay swing ($\Delta\tau$) that is inversely proportional to the coupling coefficient k, and thus superior to C-section in terms of achievable $\Delta\tau$. However, they suffer from the drawback of requiring a circulator, which is bulky, at their input to separate out the input and output signals. To eliminate this drawback, while maintaining the superior resolution benefit, we propose here the RR phaser unit shown

in Fig. 2.8, which is composed of two identical reflective resonator units combined into a two-port network via a hybrid coupler. The concept of using a coupler to transform two one-port networks into a two-port network is similar to that used in reflection-type phase shifters [99]. The hybrid coupler in Fig. 2.8 may be implemented in different technologies.

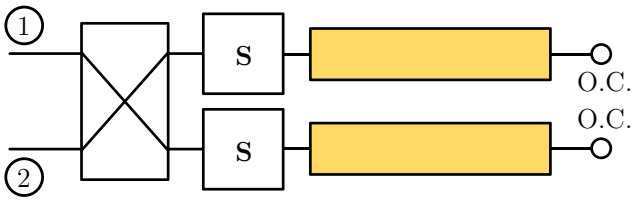

Figure 2.8 Proposed RR phaser unit based on two reflective resonators in Fig. 2.3(c) combined into a two-port network via a hybrid coupler. (L. Zou, et al [1], Proc. IMS ©2014 IEEE)

In this thesis, we use branch-line coupler, which is narrow band and is hence appropriate only for narrow-band analog signal processing applications (e.g. Doppler radar). For other applications, requiring broader bandwidth, the coupler may be implemented in various types of broadband couplers [100].

Figure 2.9 shows the layout and dimension parameters corresponding to the proposed RR phaser unit in Fig. 2.8. We fabricate a complete RR phaser prototype, consisting of two such units, as shown in Fig. 2.10, and designed to provide a group delay swing more than 7 ns over a bandwidth of 120 MHz centered at 4.09 GHz. The parameters of the two units composing this phaser are listed in Table 2.1. The two branch-line hybrids are tuned at the same frequency and hence have same dimensions : $w_1^{\mathrm{BC}} = 36.8559$ mil, $w_2^{\mathrm{BC}} = 20.7797$ mil, $\ell_1^{\mathrm{BC}} = \ell_2^{\mathrm{BC}} = 408.1352$ mil.

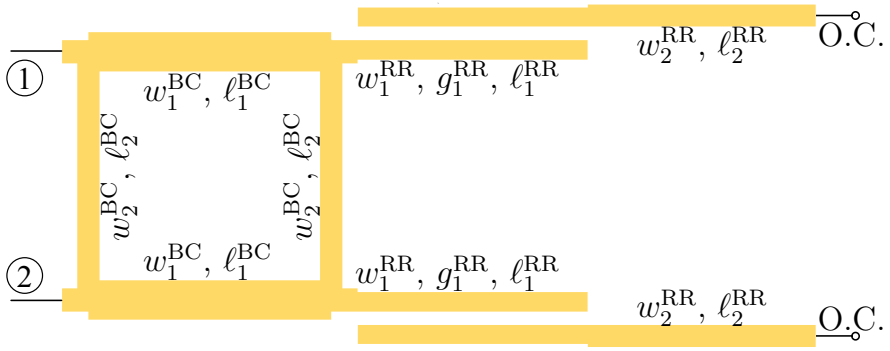

Figure 2.9 Implementation of the RR phaser unit corresponding to Fig. 2.8 using a branch-line hybrid coupler and two reflective resonators of the type shown in Fig. 2.6. (L. Zou, et al [1], Proc. IMS ©2014 IEEE)

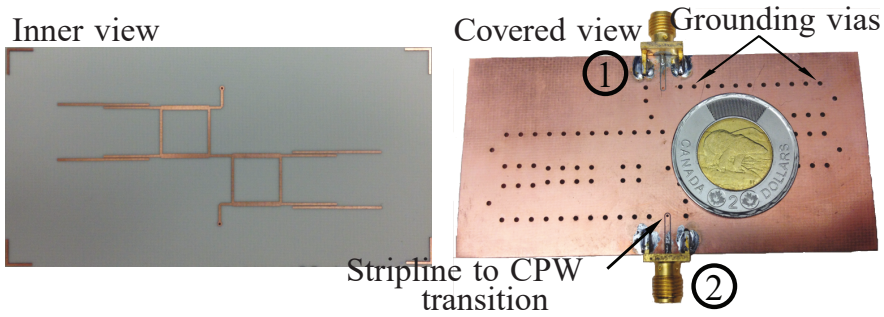

Figure 2.10 Fabricated two-unit RR phaser prototype in stripline technology. (L. Zou, et al [1], Proc. IMS ©2014 IEEE)

Table 2.1 Physical dimensions of the two-unit RR phaser shown in Fig. 2.10, with dimension parameters indicated in Fig. 2.9 (Units : mil). (L. Zou, et al [1], Proc. IMS ©2014 IEEE)

RT Unit	w_1^{RR}	g_1^{RR}	ℓ_1^{RR}	w_2^{RR}	ℓ_2^{RT}
1	17.8792	6.9895	383.8724	20.7797	383.6724
2	18.8850	9.2514	378.3913	20.7797	378.0913

The experimental results are presented in Fig. 2.11. Excellent agreement is observed with the specified group delay. The maximum insertion loss is less than 7 dB and the maximum return loss is better than 17 dB. Note that the insertion loss is proportional to the corresponding linear group delay, thus being amplitude imbalance, i.e. not flat. The amplitude imbalance issue will be addressed using loss-gain equalized phaser presented in next chapter.

Finally, Fig. 2.12 provides quantitative information on the benefit of the proposed RR phaser compared to C-section phaser with the same footprint area. In that particular design, the proposed structure provides a 20 times group delay swing enhancement compared to the C-section one.

2.5 Summary and Perspective

This chapter first introduces the group delay engineering concept and compares different passive phaser technologies, among which an all-pass phaser ideally shows flat amplitude and

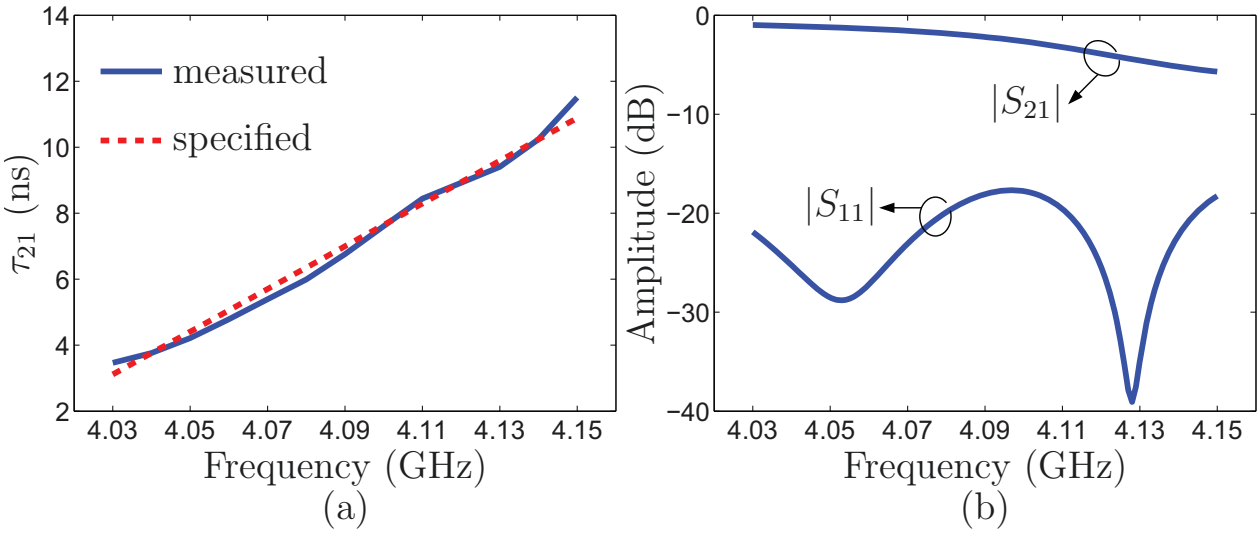

Figure 2.11 Experimental results of the RR phaser in Fig. 2.10. (a) Group delay response with $\Delta\tau \approx 10$ ns. (b) Amplitude responses (S_{11} and S_{21}).

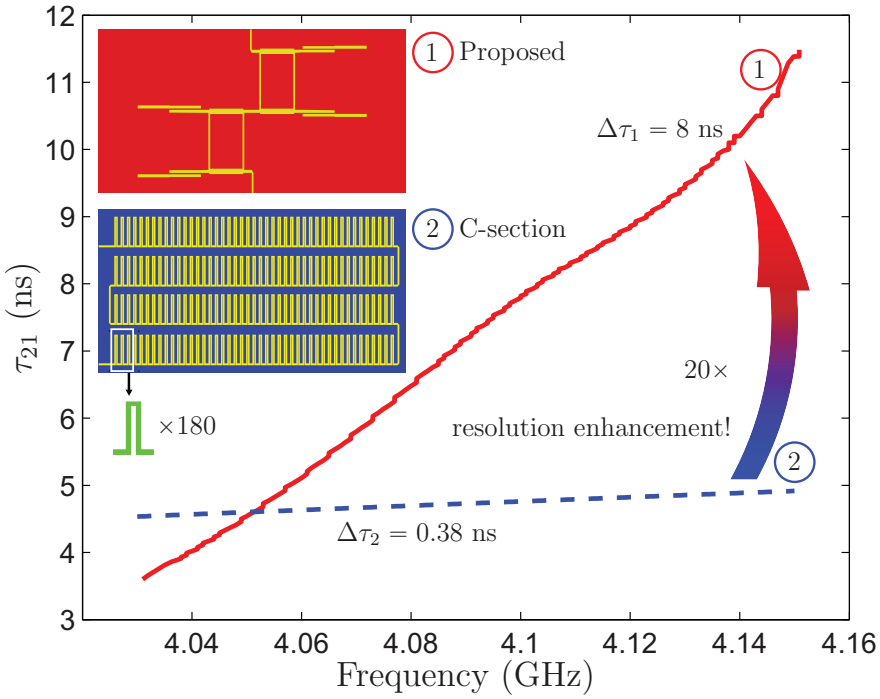

Figure 2.12 Comparison of the group delay responses of the RR phaser in Fig. 2.10 and the C-section phaser with the same footprint : (1) proposed RR phaser including only two RR units corresponding to the configuration of Fig. 2.9 (red curve) and (2) C-section phaser formed by cascading 180 C-sections (blue curve). (L. Zou, et al [1], Proc. IMS ©2014 IEEE)

group delay that can be controlled independently of its amplitude. Then, Sec. 2.3 compares three all-pass phasers, namely, C-section, ring resonator, reflective resonator, in terms of group delay swing capability, parasitic effects, and chooses reflective resonator as the candidate for frequency resolution enhancement, due to its proportionality of group delay swing to reflection coefficient and its immunity to parasitic effects. Next, Sec. 2.4 analyzes a practical implementation of the reflective resonator in terms of transfer function and group delay, and experimentally demonstrates the prototype with 20-time group delay swing enhancement compared to C-section phaser with identical footprint size. However, the reflective resonator is not without its drawbacks, 1) its reflective nature requires transformation configuration from one port to two port using 90° hybrid, thus complicating the layout design ; 2) its high group delay swing capability corresponds to narrow bandwidth due to constant time-bandwidth product for a given phaser, and also leads to high amplitude imbalance due to the loss of any natural material. The high group delay swing and narrow bandwidth properties may still find their applications in, such as for instance, real-time Doppler frequency shift. The amplitude imbalance issue may be solved by active phaser technology introduced in Chapter 3.

CHAPTER 3 GAIN-LOSS EQUALIZED ACTIVE PHASER

In Sec. 2.4, we have shown the amplitude imbalance issue [Fig. 2.11(b)] associated with passive phaser. Such issue leads to undesired signal distortion [6]. Moreover, passive phaser technologies introduced in Chapter 2 only provide fixed group delay. However, some applications may require the system to adapt to dynamic environments in real time, which may typically require group delay reconfigurability. One of such applications is dispersion code multiple access (DCMA) [101], where dynamic communication switching between different communication pairs requires real-time reconfiguration of the dispersion codes assigned to users. A reconfigurable phaser has been reported in [59] using a distributed amplifier to mimic an EBG structure [5], [22], but the obtained amplitude response is strongly frequency dependent, which is generally undesirable in R-ASP since this induces distortion [6]. In [58], an amplification feedback loop is added to a C-section phaser to increase the group delay swing. However, the group delay enhancement there is due to the equivalent cascade of N identical phasers, where N is the iteration counts controlled by an SPDT RF switch, which requires external synchronization and design complication. In that system, the amplification in the feedback loop does not contribute to group delay enhancement, but only loss compensation (L. Zou, et al [15], T-MTT, © 2017 IEEE).

This chapter systematically addresses these issues by exploiting the gain-loss equalization effect with C-section example, which leads to real all-pass amplitude response that is independent of group delay, and reconfigurable group delay response. This chapter is organized as follows : Sec. 3.1 presents the amplitude imbalance issue for a passive (lossy) C-section, then Sec. 3.2 introduces the gain-loss equalization concept, Sec. 3.3 proposes and models a practical lumped loaded active C-section in terms of scattering parameters, Sec. 3.4 presents gain-loss equalized phaser based on active C-sections and demonstrates the flat amplitude and reconfigurable group delay responses, finally Sec. 3.5 characterizes the noise figures. Part of the material in this chapter is excerpt from [15].

3.1 Amplitude Imbalance Issue

In practice, due to the inherent loss in natural materials, all passive devices are therefore lossy. Moreover, the transmission loss ($|S_{21}| < 1$) is proportional to the wave propagation distance, which in turn is proportional to the group delay τ, i.e. $20\log_{10}|S_{21}| \propto \tau$. This section only take all-pass phaser as study example for the amplitude imbalance issue, however readers should keep in mind that the conclusion applies to other types of phaser. Figure 3.1 shows a

lossy C-section example, which is constructed by shorting one end of a coupled-line coupler, whose isolated transmission line propagation constant is $\gamma = \beta - j\alpha$ [1]. Assuming TEM-wave propagation, or equal even and odd mode propagation constants, i.e. $\alpha_e = \alpha_o = \alpha$ and $\beta_e = \beta_o = \beta$, the transfer function of such a C-section structure takes the general form [12]

$$S_{21} = \frac{1 - j\kappa \tan\gamma\ell}{1 + j\kappa \tan\gamma\ell} = \frac{1 - \kappa \tanh\alpha\ell - j(\kappa - \tanh\alpha\ell)\tan\beta\ell}{1 + \kappa \tanh\alpha\ell + j(\kappa + \tanh\alpha\ell)\tan\beta\ell}, \tag{3.1}$$

where $\kappa = \sqrt{(1-k)/(1+k)}$, and k is the maximum coupling coefficient.

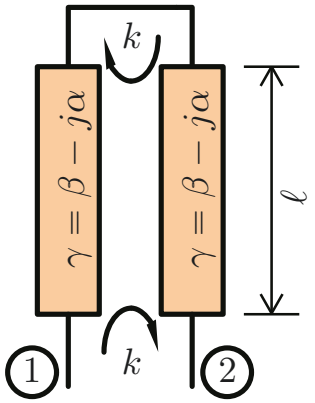

Figure 3.1 C-section with physical length ℓ, maximum coupling coefficient k, and isolated transmission line propagation constant $\gamma = \beta - j\alpha$.

Figure 3.2 plots C-section responses for lossless and lossy cases, where the former leads to ideal all-pass response ($|S_{21}| \equiv 1$), while the latter leads to overall loss that is proportional to the corresponding group delay (τ). Note that the group delay difference for two cases is negligible here, we will show how group delay is affected by loss in Sec. 3.2.

Figure 3.3 plots C-section responses for different k values for lossy case. Increasing k increases group delay swing [12], which is the result of increased wave travelling distance. Therefore, the wave propagating through a C-section with higher k experiences higher loss that is proportional to the corresponding propagation distance, and hence proportional to the group delay, i.e. $20\log_{10}|S_{21}| \propto \tau$.

Given the aforementioned amplitude-delay dependence ($20\log_{10}|S_{21}| \propto \tau$), in the presence of dispersion, i.e. $\tau(\omega) \neq$ constant, the amplitude is imbalance, i.e. $|S_{21}(\omega)| \neq$ constant. Such amplitude imbalance can be explained by Kramers-Kronig relation that relates the transfer function amplitude with phase [81], and creates undesired signal distortion [6]. This issue is systematically addressed in Chapter 3.

1. The time dependence $e^{+j\omega t}$.

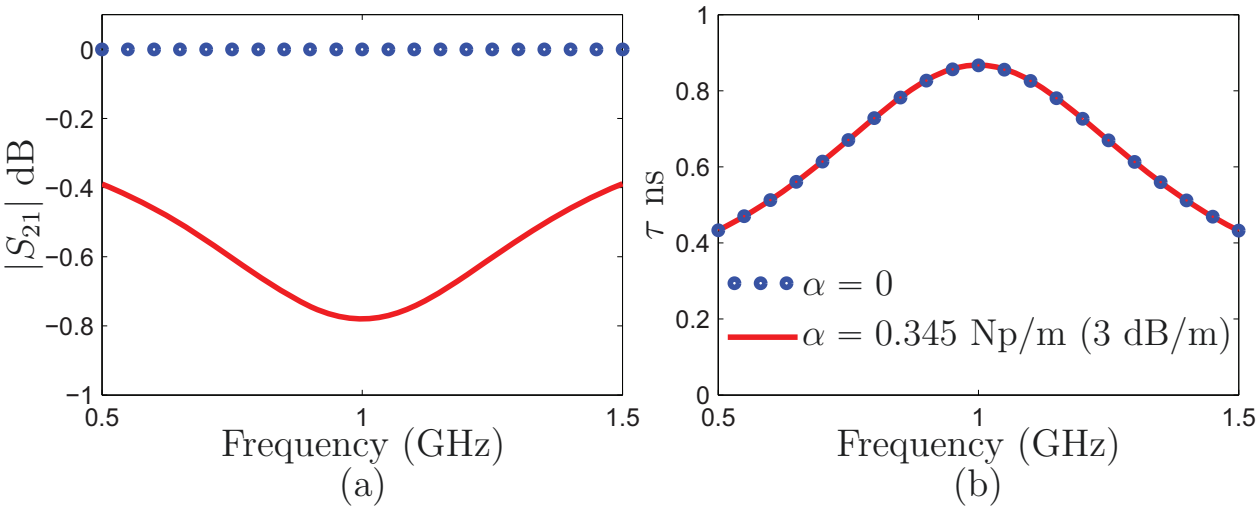

Figure 3.2 Circuit simulated responses of the C-section in Fig. 3.1 with S_{21} given by (3.1) with $\alpha = 0$ (lossless) and $\alpha = 0.345$ Np/m (3 dB/m loss), and $\beta = k_0$ (k_0 is free space wave number for $\epsilon_r = 1$), coupling coefficient $k = 0.5$, physical length $\ell = 0.075$ m (quarter wavelength at 1 GHz). (a) Transfer amplitude $|S_{21}|$. (b) Group delay response τ.

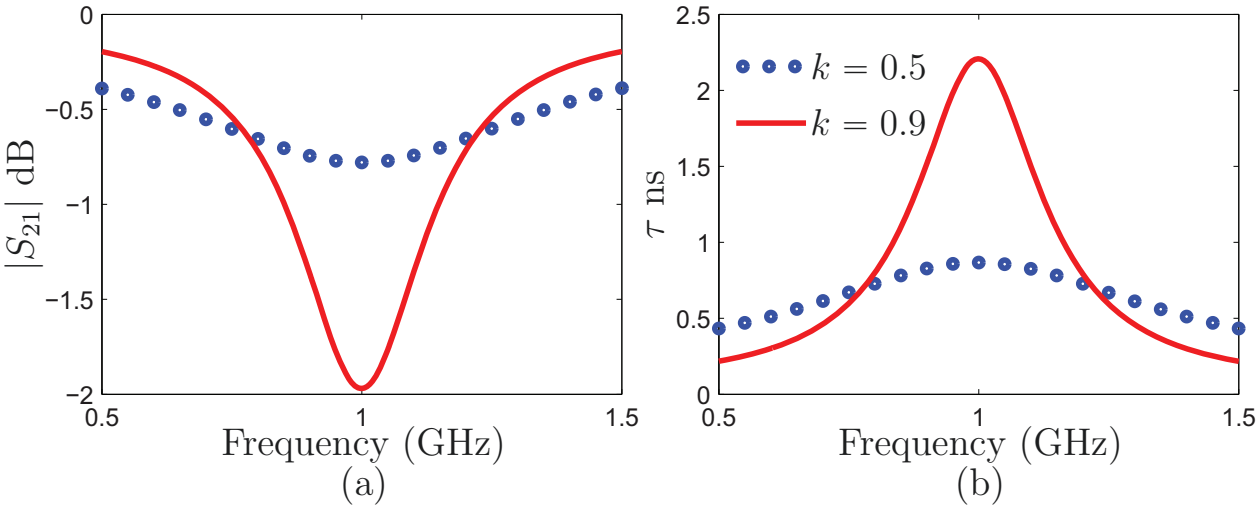

Figure 3.3 Circuit simulated responses of the lossy ($\alpha = 0.345$ Np/m or 3 dB/m) C-section in Fig. 3.1 with coupling coefficients $k = 0.5$ and $k = 0.9$, and , $\beta = k_0$ (k_0 is free space wave number for $\epsilon_r = 1$), physical length $\ell = 0.075$ m (quarter wavelength at 1 GHz). (a) Transfer amplitude $|S_{21}|$. (b) Group delay response τ. Note that $k = 0.9$ is typically impractical value for planar fabrication, here we just use it numerically to exaggerate the difference.

3.2 Gain-Loss Equalization Concept

This section includes both gain and loss in C-section, showing that the balanced gain and loss C-sections exhibit opposite amplitudes and identical group delays. To include either loss or gain in the C-section in Fig. 3.1 and in the corresponding transfer function in (3.1), we shall allow the imaginary part of the isolated transmission line propagation factor, α to be now either positive (loss) or negative (gain). The corresponding amplitude and the phase of (3.1) are

$$|S_{21}| = \sqrt{\frac{(1-\kappa\tanh\alpha\ell)^2+(\kappa-\tanh\alpha\ell)^2\tan^2\beta\ell}{(1+\kappa\tanh\alpha\ell)^2+(\kappa+\tanh\alpha\ell)^2\tan^2\beta\ell}}, \tag{3.2a}$$

$$\angle S_{21} = -\arctan\left(\frac{\kappa-\tanh\alpha\ell}{1-\kappa\tanh\alpha\ell}\tan\beta\ell\right) - \arctan\left(\frac{\kappa+\tanh\alpha\ell}{1+\kappa\tanh\alpha\ell}\tan\beta\ell\right), \tag{3.2b}$$

respectively. Inspecting (3.2a) and (3.2b) reveals that reversing the sign of α reverses $|S_{21}|$ while keeps $\angle S_{21}$ unchanged, i.e.

$$|S_{21}(-\alpha)| = \frac{1}{|S_{21}(\alpha)|}, \tag{3.3a}$$

$$\angle S_{21}(-\alpha) = \angle S_{21}(\alpha), \tag{3.3b}$$

respectively. Equations (3.3a) and (3.3b) state that equalized distributed loss ($|\alpha|$) and gain ($-|\alpha|$) yields amplitudes symmetric about 0 dB, i.e. $20\log(|S_{21}(-\alpha)|) = -20\log(|S_{21}(\alpha)|)$, and identical group delays, $\tau_{21}(-\alpha) = \tau_{21}(\alpha)$, since $\tau_{21} = -\partial\angle S_{21}/\partial\omega$, as plotted in Fig. 3.4. Moreover, the group delay swing is proportional (non-linearly) to the absolute value of gain or loss. The tuning effect of gain and loss on group delay will be later shown to allow group delay reconfigurability, the symmetry of gain and loss amplitudes about 0 dB will lead to perfect overall amplitude compensation and thus real all-pass response, by combining equalized gain and loss sections. However, *distributed* gain and loss profiles would be difficult to engineer, and we therefore now turn to *lumped* gain and loss inclusions, where the same conclusions will be shown to hold.

3.3 Active Loaded C-Section

We consider the lumped loaded active C-section shown in Fig. 3.5, where the coupler, practically including parasitic effects such as forward coupling and reflection, is assumed to be lossless and terminated at one end (ports 3 and 4) by a load, which may have loss or gain. We may always consider the actual loss of the coupler is absorbed in the load, for simplicity. The scattering matrices of the coupler and the load may be written as

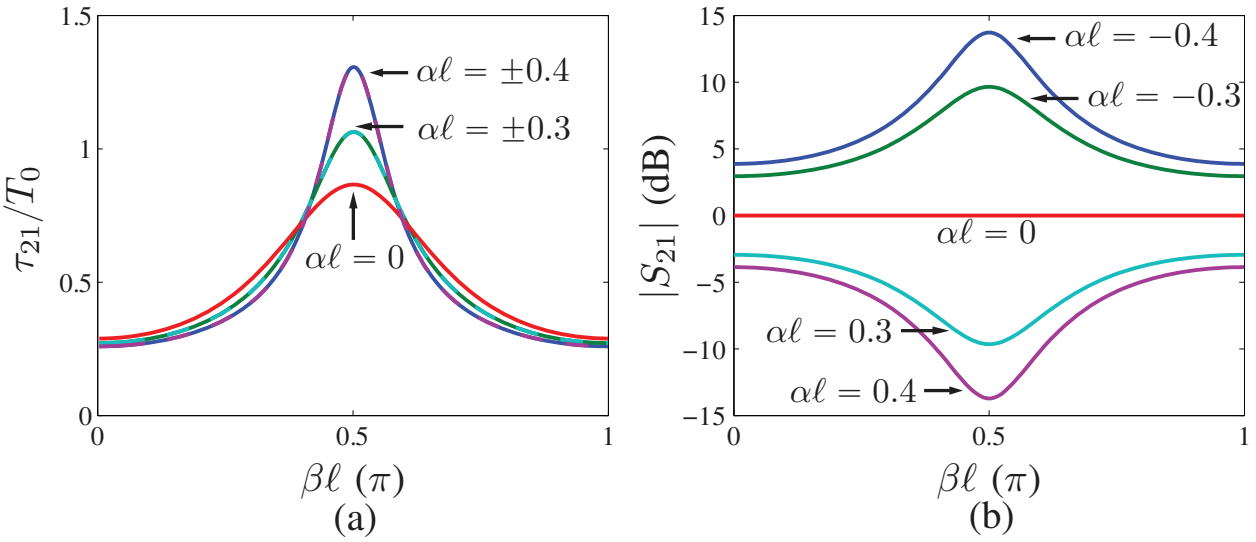

Figure 3.4 Single C-section responses for different equalized gain ($\alpha < 0$) loss ($\alpha > 0$) pairs, with $\beta\ell = \pi\omega/(2\omega_0)$ and coupling coefficient $k = 0.5$. (a) Group delay responses normalized by the period, T_0, of the quarter wavelength frequency ω_0. (b) Amplitude responses.

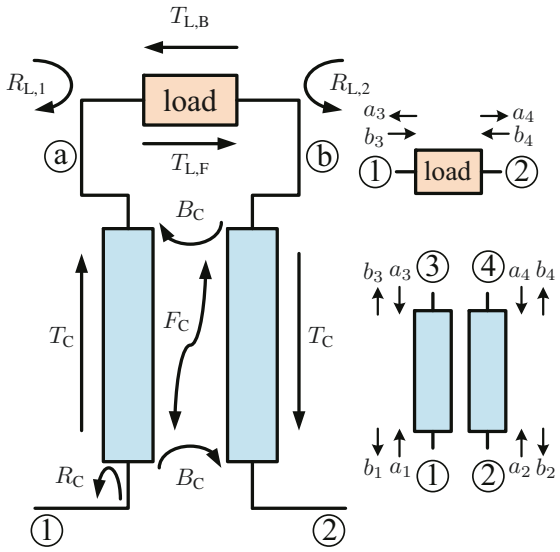

Figure 3.5 Lumped loaded active C-section consisting of a coupled-line coupler and a load with corresponding scattering parameters indicated.

$$\mathbf{S}_C = \begin{bmatrix} R_C & B_C & T_C & F_C \\ B_C & R_C & F_C & T_C \\ T_C & F_C & R_C & B_C \\ F_C & T_C & B_C & R_C \end{bmatrix}, \tag{3.4a}$$

$$\mathbf{S}_{\mathrm{L}} = \begin{bmatrix} R_{\mathrm{L},1} & T_{\mathrm{L,B}} \\ T_{\mathrm{L,F}} & R_{\mathrm{L},2} \end{bmatrix}, \tag{3.4b}$$

where B_{C}, F_{C}, T_{C} and R_{C} are the coupler backward and forward-wave coupling, through transmission and local reflection coefficients, respectively, and $R_{\mathrm{L},1}$, $R_{\mathrm{L},2}$, $T_{\mathrm{L,F}}$ and $T_{\mathrm{L,B}}$ are the load input and output reflection, and forward and backward transmission coefficients, respectively. The load will be implemented in the form of a transistor, which may be assumed to be unilateral, and we shall therefore next assume $T_{\mathrm{L,B}} = 0$. Ideally, F_{C}=$R_{\mathrm{C}} = 0$ for purely TEM-wave coupler, and $R_{\mathrm{L},1} = R_{\mathrm{L},2} = 0$ for perfectly matched load. However, in practice, F_{C}, R_{C}, $R_{\mathrm{L},1}$, $R_{\mathrm{L},2} \neq 0$, which represent non-idealities that create undesired wave paths. We shall now derive the scattering parameters of the active C-section.

3.3.1 Exact Scattering Parameters

The exact scattering parameters of the active C-section may be obtained, following the technique used in [102], by embedding the 2-port scattering matrix of the load into the 4-port scattering matrix of the coupler, which leads to the scattering matrix of the resulting 2-port active C-section.

The scattering of the coupler (without load) may be described by the general matrix equation

$$\mathbf{B} = \mathbf{S}_{\mathrm{C}}\mathbf{A}, \tag{3.5a}$$

where the vectors $\mathbf{A} = [a_1, a_2, a_3, a_4]^{\mathrm{T}}$ and $\mathbf{B} = [b_1, b_2, b_3, b_4]^{\mathrm{T}}$ are composed of the input and output waves at the 4 ports, respectively, or

$$\begin{bmatrix} \mathbf{B}_1 \\ \mathbf{B}_2 \end{bmatrix} = \begin{bmatrix} \mathbf{S}_1 & \mathbf{S}_2 \\ \mathbf{S}_2 & \mathbf{S}_1 \end{bmatrix} \begin{bmatrix} \mathbf{A}_1 \\ \mathbf{A}_2 \end{bmatrix}, \tag{3.5b}$$

where the matrix $\mathbf{S}_{\mathrm{C}}$, explicitely given in (3.4a), and the vectors $\mathbf{A}$ and $\mathbf{B}$ have been decomposed into the 2×2 and 2×1 block matrices

$$\begin{aligned} &\mathbf{S}_1 = \begin{bmatrix} R_{\mathrm{C}} & B_{\mathrm{C}} \\ B_{\mathrm{C}} & R_{\mathrm{C}} \end{bmatrix}, \quad \mathbf{S}_2 = \begin{bmatrix} T_{\mathrm{C}} & F_{\mathrm{C}} \\ F_{\mathrm{C}} & T_{\mathrm{C}} \end{bmatrix}, \quad \text{and} \\ &\mathbf{B}_1 = \begin{bmatrix} b_1 \\ b_2 \end{bmatrix}, \ \mathbf{B}_2 = \begin{bmatrix} b_3 \\ b_4 \end{bmatrix}, \ \mathbf{A}_1 = \begin{bmatrix} a_1 \\ a_2 \end{bmatrix}, \ \mathbf{A}_2 = \begin{bmatrix} a_3 \\ a_4 \end{bmatrix}, \end{aligned} \tag{3.5c}$$

respectively.

Noting that $\mathbf{B}_2$ and $\mathbf{A}_2$ represent the input and output waves of the load, respectively, the

effect of the load may be incorporated in these relations by setting

$$\mathbf{A}_2 = \mathbf{S}_\mathrm{L}\mathbf{B}_2, \tag{3.6}$$

where $\mathbf{S}_\mathrm{L}$ is explicitly given in (3.4b). Inserting (3.6) into (3.5b) yields

$$\mathbf{B}_1 = \mathbf{S}_1\mathbf{A}_1 + \mathbf{S}_2\mathbf{S}_\mathrm{L}\mathbf{B}_2, \tag{3.7a}$$

$$\mathbf{B}_2 = \mathbf{S}_2\mathbf{A}_1 + \mathbf{S}_1\mathbf{S}_\mathrm{L}\mathbf{B}_2. \tag{3.7b}$$

Solving (3.7b) for $\mathbf{B}_2$ leads to

$$\mathbf{B}_2 = \left(\mathbf{I} - \mathbf{S}_1\mathbf{S}_\mathrm{L}\right)^{-1}\mathbf{S}_2\mathbf{A}_1, \text{ with } \mathbf{I} = \begin{bmatrix} 1 & 0 \\ 0 & 1 \end{bmatrix}. \tag{3.8}$$

Inserting (3.8) into (3.7a) and solving for $\mathbf{B}_1$ finally yields

$$\mathbf{B}_1 = \left[\mathbf{S}_1 + \mathbf{S}_2\mathbf{S}_\mathrm{L}\left(\mathbf{I} - \mathbf{S}_1\mathbf{S}_\mathrm{L}\right)^{-1}\mathbf{S}_2\right]\mathbf{A}_1 = \mathbf{S}\mathbf{A}_1, \tag{3.9}$$

which is the general scattering relation of the active C-section characterized by the global scattering matrix $\mathbf{S}$

$$\mathbf{S} = \begin{bmatrix} S_{11} & S_{12} \\ S_{21} & S_{22} \end{bmatrix} = \mathbf{S}_1 + \mathbf{S}_2\mathbf{S}_\mathrm{L}\left(\mathbf{I} - \mathbf{S}_1\mathbf{S}_\mathrm{L}\right)^{-1}\mathbf{S}_2. \tag{3.10}$$

Finally, substituting (3.4b) for $\mathbf{S}_\mathrm{L}$ with $T_\mathrm{L,B} = 0$ (unidirectional load assumption) and (3.5c) for $\mathbf{S}_1$ and $\mathbf{S}_2$ into (3.10) yields the *exact* scattering parameters of the active C-section that are given in (3.11).

$$S_{11} = R_\mathrm{C} + \frac{T_\mathrm{C}^2 R_{\mathrm{L},1} + T_\mathrm{C}T_{\mathrm{L,F}}F_\mathrm{C} + F_\mathrm{C}^2 R_{\mathrm{L},2} - T_\mathrm{C}^2 R_\mathrm{C} R_{\mathrm{L},1}R_{\mathrm{L},2} + 2T_\mathrm{C}B_\mathrm{C}F_\mathrm{C}R_{\mathrm{L},1}R_{\mathrm{L},2} - F_\mathrm{C}^2 R_\mathrm{C}R_{\mathrm{L},1}R_{\mathrm{L},2}}{1 - B_\mathrm{C}T_{\mathrm{L,F}} - R_\mathrm{C}R_{\mathrm{L},1} - R_\mathrm{C}R_{\mathrm{L},2} - B_\mathrm{C}^2 R_{\mathrm{L},1}R_{\mathrm{L},2} + R_\mathrm{C}^2 R_{\mathrm{L},1}R_{\mathrm{L},2}}, \tag{3.11a}$$

$$S_{21} = B_\mathrm{C} + \frac{T_\mathrm{C}^2 T_{\mathrm{L,F}} + T_\mathrm{C}F_\mathrm{C}R_{\mathrm{L},1} + T_\mathrm{C}F_\mathrm{C}R_{\mathrm{L},2} + B_\mathrm{C}T_\mathrm{C}^2 R_{\mathrm{L},1}R_{\mathrm{L},2} + B_\mathrm{C}F_\mathrm{C}^2 R_{\mathrm{L},1}R_{\mathrm{L},2} - 2T_\mathrm{C}F_\mathrm{C}R_\mathrm{C}R_{\mathrm{L},1}R_{\mathrm{L},2}}{1 - B_\mathrm{C}T_{\mathrm{L,F}} - R_\mathrm{C}R_{\mathrm{L},1} - R_\mathrm{C}R_{\mathrm{L},2} - B_\mathrm{C}^2 R_{\mathrm{L},1}R_{\mathrm{L},2} + R_\mathrm{C}^2 R_{\mathrm{L},1}R_{\mathrm{L},2}}, \tag{3.11b}$$

$$S_{22} = R_\mathrm{C} + \frac{T_\mathrm{C}^2 R_{\mathrm{L},2} + T_\mathrm{C}T_{\mathrm{L,F}}F_\mathrm{C} + F_\mathrm{C}^2 R_{\mathrm{L},1} - T_\mathrm{C}^2 R_\mathrm{C} R_{\mathrm{L},1}R_{\mathrm{L},2} + 2T_\mathrm{C}B_\mathrm{C}F_\mathrm{C}R_{\mathrm{L},1}R_{\mathrm{L},2} - F_\mathrm{C}^2 R_\mathrm{C}R_{\mathrm{L},1}R_{\mathrm{L},2}}{1 - B_\mathrm{C}T_{\mathrm{L,F}} - R_\mathrm{C}R_{\mathrm{L},1} - R_\mathrm{C}R_{\mathrm{L},2} - B_\mathrm{C}^2 R_{\mathrm{L},1}R_{\mathrm{L},2} + R_\mathrm{C}^2 R_{\mathrm{L},1}R_{\mathrm{L},2}}, \tag{3.11c}$$

$$S_{12} = B_\mathrm{C} + \frac{F_\mathrm{C}^2 T_{\mathrm{L,F}} + T_\mathrm{C}F_\mathrm{C}R_{\mathrm{L},1} + T_\mathrm{C}F_\mathrm{C}R_{\mathrm{L},2} + B_\mathrm{C}T_\mathrm{C}^2 R_{\mathrm{L},1}R_{\mathrm{L},2} + B_\mathrm{C}F_\mathrm{C}^2 R_{\mathrm{L},1}R_{\mathrm{L},2} - 2T_\mathrm{C}F_\mathrm{C}R_\mathrm{C}R_{\mathrm{L},1}R_{\mathrm{L},2}}{1 - B_\mathrm{C}T_{\mathrm{L,F}} - R_\mathrm{C}R_{\mathrm{L},1} - R_\mathrm{C}R_{\mathrm{L},2} - B_\mathrm{C}^2 R_{\mathrm{L},1}R_{\mathrm{L},2} + R_\mathrm{C}^2 R_{\mathrm{L},1}R_{\mathrm{L},2}}. \tag{3.11d}$$

3.3.2 Approximate Scattering Parameters

Equations (3.11) are lengthy and cumbersome, and provide little insight into the scattering phenomenon that they represent. However, the aforementioned non-idealities are usually weak parasitic effects in the design bandwidth, corresponding to small quantities. The parameters $F_{\mathrm{C}}, R_{\mathrm{C}}, R_{\mathrm{L},1}, R_{\mathrm{L},2}$ in (3.4) are therefore small quantities that may be ignored when appearing in orders larger than one. Keeping thus only the zero and first order terms reduces (3.11) to the much simpler relations

$$S_{11} \approx R_{\mathrm{C}} + \frac{T_{\mathrm{C}}^2 R_{\mathrm{L},1} + T_{\mathrm{C}} F_{\mathrm{C}} T_{\mathrm{L,F}}}{1 - B_{\mathrm{C}} T_{\mathrm{L,F}}}, \tag{3.12a}$$

$$S_{21} \approx B_{\mathrm{C}} + \frac{T_{\mathrm{C}}^2 T_{\mathrm{L,F}}}{1 - B_{\mathrm{C}} T_{\mathrm{L,F}}}, \tag{3.12b}$$

$$S_{22} \approx R_{\mathrm{C}} + \frac{T_{\mathrm{C}}^2 R_{\mathrm{L},2} + T_{\mathrm{C}} F_{\mathrm{C}} T_{\mathrm{L,F}}}{1 - B_{\mathrm{C}} T_{\mathrm{L,F}}}, \tag{3.12c}$$

$$S_{12} \approx B_{\mathrm{C}}. \tag{3.12d}$$

In order to obtain the simplified expressions (3.12), we had to pass through the complicated and insightless relations Eqs (3.11). However, these relations may also be arrived at in a much simpler and more insightful manner using the flow graph technique, which will additionally, and most importantly, provide us with an efficient approach for the practical design of the active loaded C-section device.

The signal flow graph corresponding to the C-section in Fig. 3.5 is shown in Fig. 3.6. In this graph, two main paths, the forward (upper) and backward (lower) paths, couple to each other *only* via the non-idealities (all of the paths in-between). An ideal C-section, excluding the non-ideality paths, would include only either the forward path (port 1 excited) or the backward path (port 2 excited).

Taking account all the paths in Fig. 3.6 will naturally lead to the exact scattering parameters, but we apply here some simplifications. In the following discussion, the subscripts F and B refer to the forward and backward paths, respectively. Now we take S_{11} signal flow graph as the simplification example, where we study the signal propagating from port 1_{F} to port 1_{B}. Assuming small non-idealities, we perform the following sequence of simplifications : i) Due to the absence of excitation at port 2, node 2_{B} and all connected paths are removed. Moreover, node 2_{F} and all connected paths, not contributing to backward propagation towards port 1, are also removed, resulting in the flow graph shown in Fig. 3.7(a). ii) The return paths from the backward to the forward directions, namely the paths $R_{\mathrm{C}} : \mathrm{a_B} \rightarrow \mathrm{a_F}$ and $R_{\mathrm{L},2}$:

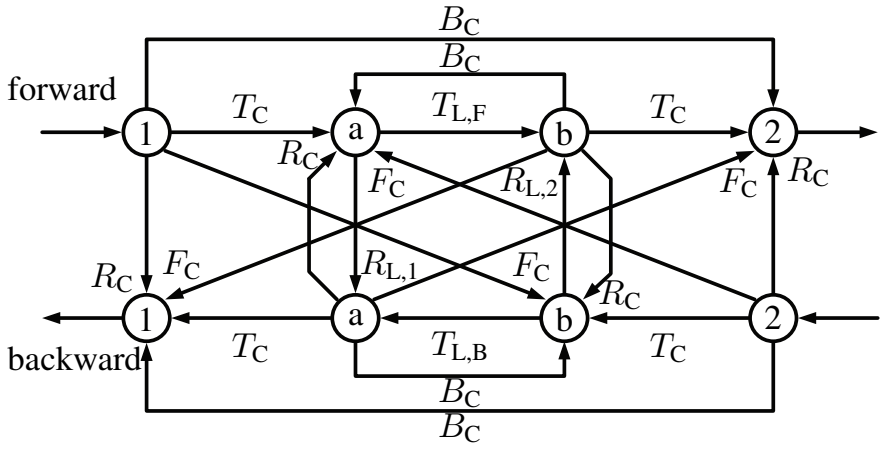

Figure 3.6 Signal flow graph modeling the active C-section in Fig. 3.5.

$b_B \rightarrow b_F$ are removed, because they give rise to non-ideality terms of order higher the the first order, which results into the flow graph of Fig. 3.7(b). iii) Considering transistor load, where $|T_{L,B}| \approx 0$, we finally omit the path $T_{L,B}$ and the node b_B, which leads to the final flow graph in Fig. 3.7(c).

Denoting $v_{i,F/B}$ the voltage at node i for forward/backward propagation, the reflection signal at port 1, i.e. $v_{1,B}$, is

$$v_{1,B} = R_C v_{1,F} + F_C v_{b,F} + T_C R_{L,1} v_a,F = R_C v_{1,F} + (F_C T_{L,F} + T_C R_{L,1}) \frac{T_C v_{1,F}}{1 - T_{L,F} B_C}, \quad (3.13)$$

leading to overall input reflection coefficient

$$S_{11} = \frac{v_{1,B}}{v_{1,F}} = R_C + \frac{T_C^2 R_{L,1} + T_C F_C T_{L,F}}{1 - B_C T_{L,F}}, \quad (3.14)$$

which is identical to (3.12a). Following similar simplification procedures leads to the signal flow graphs for S_{21}, S_{22} and S_{12} shown in Figs 3.8(a), (b) and (c), respectively. Their corresponding scattering parameters derived from the flow graphs are also found to be identical to Eqs (3.12b), (3.12c) and (3.12d).

3.3.3 Resonance and Convergence Conditions

Observing the flow graphs in Figs 3.7(c), 3.8(a) and 3.8(b) corresponding to S_{11}, S_{21} and S_{22}, respectively, one finds that they all have a feedback path due to the backward coupling (B_C), and the closed feedback loop transfer function is $B_C T_{L,F}$, as in the denominator of (3.12a), (3.12b) and (3.12c). The transfer phase and amplitude of $B_C T_{L,F}$ correspond to resonance

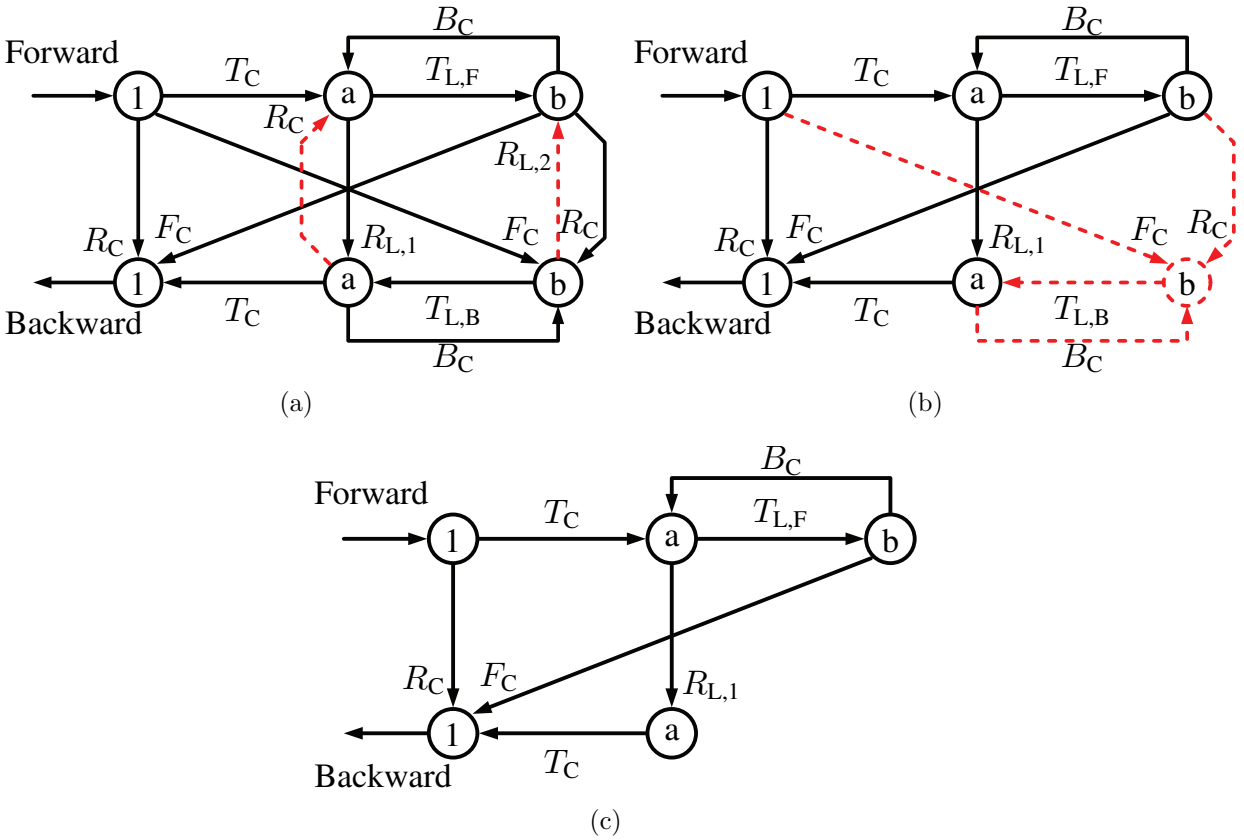

Figure 3.7 Progressive simplification of Fig. 3.6 for S_{11} : (a) removing higher-order paths (red dashed lines), (b) omitting negligible load backward transmission (red dashed lines), (c) final chart.

and convergence conditions, respectively [15].

At resonance frequency, ω_r, the loop transfer function is purely real, i.e. $B_C T_{L,F} \in \mathbb{R}$, and $|S_{11}|$, $|S_{21}|$ and $|S_{22}|$ are maximum. The loop phase for resonance condition is

$$\angle[T_{L,F}(\omega_r)B_C(\omega_r)] = \angle T_{L,F}(\omega_r) + \angle B_C(\omega_r) = 2\pi n, \quad (n \in \mathbb{Z}). \tag{3.15a}$$

At the resonance frequency, the loop transfer amplitude should be smaller than 1, i.e. $|B_C(\omega_r)T_{L,F}(\omega_r)| < 1$, to ensure $|S_{11}|$, $|S_{21}|$ and $|S_{22}|$ being convergent, i.e. $|S_{11}|$, $|S_{21}|$, $|S_{22}| < \infty$. The loop amplitude for convergence condition is equivalent to

$$|T_{L,F}(\omega_r)| < \frac{1}{|B_C(\omega_r)|}. \tag{3.15b}$$

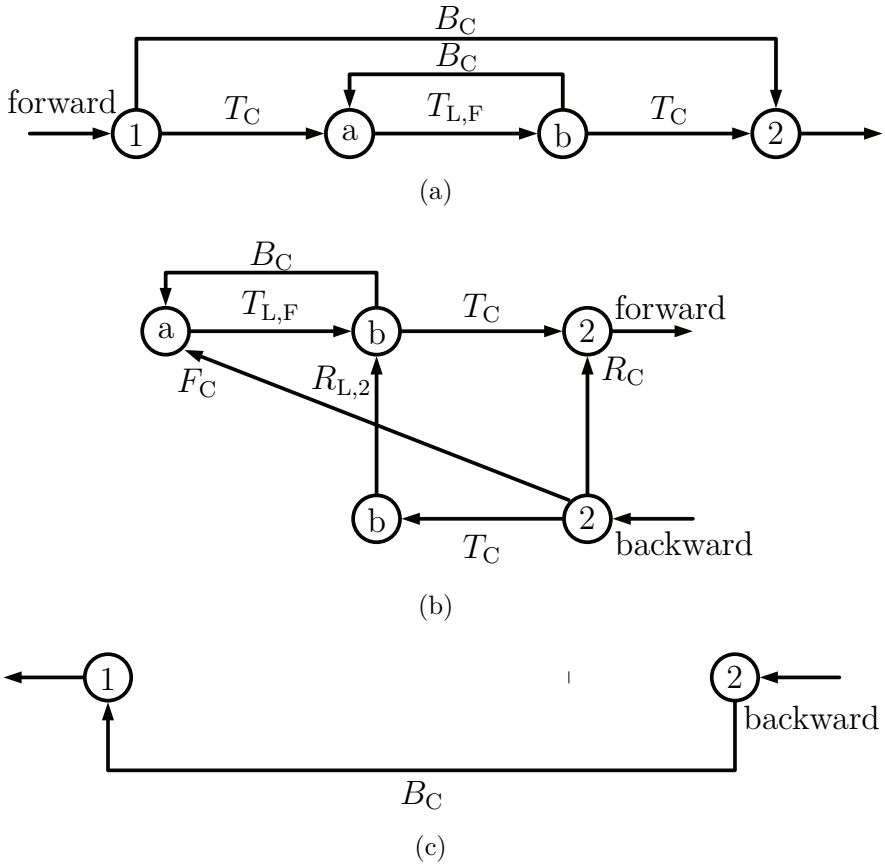

Figure 3.8 Simplified signal flow graphs of Fig. 3.6 for (a) S_{21}, (b) S_{22}, and (c) S_{12}.

3.3.4 Verification of the Exact and Approximate Formulas

To verify the analytical scattering parameters given by Eqs (3.11) and (3.12), one my compare them against the circuit-simulated ones. For this purpose, we use a microstrip coupled-line coupler (with non-zero F_C and R_C) and transistor load (with non-zero $R_{L,1}$ and $R_{L,2}$). Their responses are plotted in Fig. 3.9.

The coupler and load responses in Fig. 3.9 are next inserted into (3.11) (analytical exact) and (3.12) (analytical approximate), and the results are compared against ADS circuit-simulated results (exact) using the same coupler and load models. As an example, Fig. 3.10(a) plots $|S_{11}|$ for different values of $|T_{L,F}|$; the differences between analytical exact parameters [Eq. (3.11a)], analytical approximate parameters [Eq. (3.12a)] and simulated results are undistinguishable. Figure 3.10(b) shows the relative error of the analytical results [Eqs. (3.11a), (3.12a)] with respect to the simulated ones, where this error being defined as

$$\text{Error}_{ij} = \frac{|S_{ij,\text{analytical}}| - |S_{ij,\text{simulated}}|}{|S_{ij,\text{simulated}}|} \times 100\%, \tag{3.16}$$

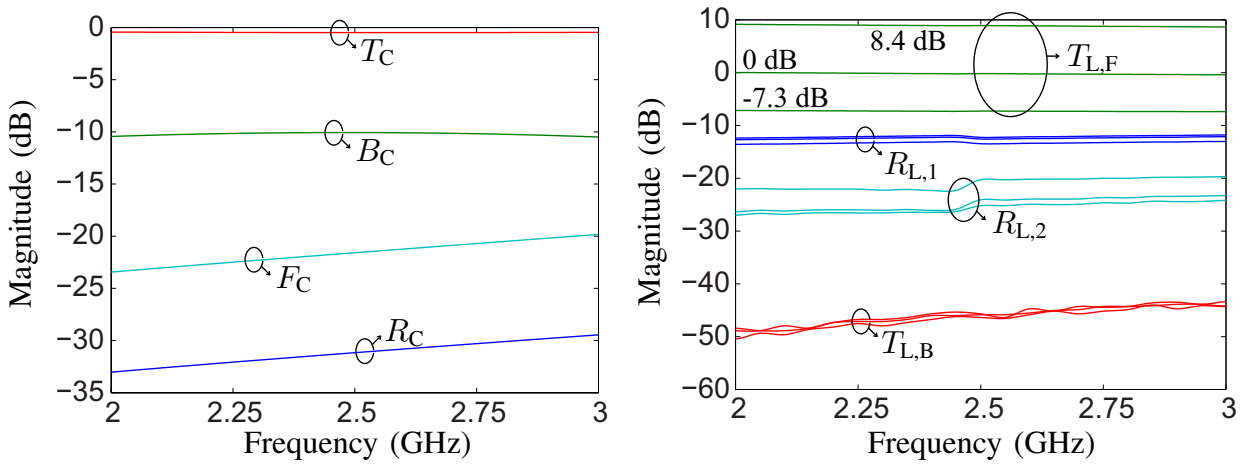

(a) (b)

Figure 3.9 Scattering parameter versus frequency. (a) Simulated transfer amplitudes of a microstrip coupler. (b) Measured transfer amplitudes of a transistor load (variable gain amplifier S2P model of Avago VMMK-3503) corresponding to forward transmission (variable gain) $|T_{\mathrm{L,F}}| = 8.4$, 0 and -7.3 dB, respectively, and $T_{\mathrm{L,B}} \approx -50$ dB which may be practically ignored.

with $S_{ij,\mathrm{analytical}}$ being obtained by (3.11) or by (3.12). The largest error corresponds, as expected, to the approximate formula, Eq. (3.12a), but it does not exceed 5%, confirming that the approximate parameters are practically satisfactory. Excellent agreement is also observed for Eqs. (3.12b), (3.12c) and (3.12d).

Note that when the load has gain, such as for instance $|T_{\mathrm{L,F}}| = 8.4$ dB, the overall C-section may be poorly matched as shown in Fig. 3.10(a). The corresponding matching will be considered with the practical prototype design example in Sec. 3.4.3.

3.4 Gain-Loss Equalized Phaser Based on Active C-Section

This section first characterizes the transfer (S_{21}) group delay and amplitude responses of an Active C-section, and then proposes the gain-loss equalized phaser, finally designs, fabricates and experimentally demonstrates the prototypes.

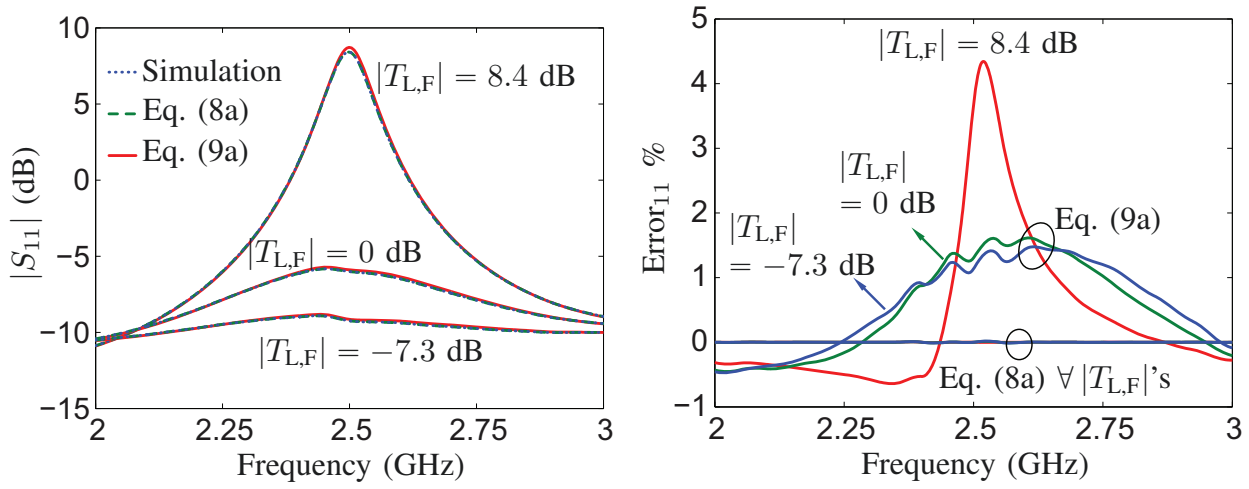

(a) (b)

Figure 3.10 Comparison of the exact [Eq. (3.11a)] and approximate [Eq. (3.12a)] scattering parameters with circuit-simulated scattering parameter using the model in Fig. 3.5 with the coupler and load responses in Fig. 3.9. (a) S_{11} for different $|T_{L,F}|$'s. (b) Corresponding error, defined by (3.16), for Eqs. (3.11a) and (3.12a). The resonance frequency, as defined in (3.15a), is $f_r = 2.5$ GHz, and the corresponding scattering pole, defined in (3.15b), is found from Fig. 3.9(a) as $|T^p_{L,F}| = 1/|B_C(f_r)| = 10$ dB.

3.4.1 Transfer Group Delay and Amplitude Characterization

The information of the amplitude and group delay resides in the transfer function given by (3.12b), which is reproduced below :

$$S_{21} \approx B_C + \frac{T_C^2 T_{L,F}}{1 - B_C T_{L,F}}. \tag{3.17}$$

The parameters in (3.17) are coupler backward coupling and through coefficients, and load forward transmission coefficient, namely B_C, T_C and $T_{L,F}$, and given by

$$B_C(\omega) = \frac{jk \sin\theta}{\sqrt{1-k^2}\cos\theta + j\sin\theta}, \tag{3.18a}$$

$$T_C(\omega) = \frac{\sqrt{1-k^2}}{\sqrt{1-k^2}\cos\theta + j\sin\theta}, \tag{3.18b}$$

and

$$T_{L,F}(\omega) = A_{L,F}(\omega) e^{j\phi_{L,F}(\omega)}, \tag{3.18c}$$

respectively [15, 100], with parameters k being the maximum coupling occurring at the quarter-wavelength frequency ω_0, and $\theta = \pi\omega/2\omega_0$ being the electrical length of the coupler at any frequency ω.

Inserting (3.18a), (3.18b) and (3.18c) into (3.17) yields

$$S_{21} = T_{\mathrm{L}} \frac{\sqrt{1-k^2}\cot\theta + k/A_{\mathrm{L}}\sin\phi_{\mathrm{L}} - j\left(1 - k/A_{\mathrm{L}}\cos\phi_{\mathrm{L}}\right)}{\sqrt{1-k^2}\cot\theta + kA_{\mathrm{L}}\sin\phi_{\mathrm{L}} + j\left(1 - kA_{\mathrm{L}}\cos\phi_{\mathrm{L}}\right)} = |S_{21}|\, e^{j\phi_{21}}, \tag{3.19a}$$

where

$$|S_{21}| = A_{\mathrm{L}} \sqrt{\frac{\left(\sqrt{1-k^2}\cot\theta + k/A_{\mathrm{L}}\sin\phi_{\mathrm{L}}\right)^2 + \left(1 - k/A_{\mathrm{L}}\cos\phi_{\mathrm{L}}\right)^2}{\left(\sqrt{1-k^2}\cot\theta + kA_{\mathrm{L}}\sin\phi_{\mathrm{L}}\right)^2 + \left(1 - kA_{\mathrm{L}}\cos\phi_{\mathrm{L}}\right)^2}}, \tag{3.19b}$$

$$\angle S_{21} = -\arctan\frac{1 - k/A_{\mathrm{L}}\cos\phi_{\mathrm{L}}}{\sqrt{1-k^2}\cot\theta + k/A_{\mathrm{L}}\sin\phi_{\mathrm{L}}} - \arctan\frac{1 - kA_{\mathrm{L}}\cos\phi_{\mathrm{L}}}{\sqrt{1-k^2}\cot\theta + kA_{\mathrm{L}}\sin\phi_{\mathrm{L}}} + \phi_{\mathrm{L}}, \tag{3.19c}$$

Inspecting (3.19b) and (3.19c) reveals that reversing the load transmission amplitude, i.e. $A_{\mathrm{L}} \to 1/A_{\mathrm{L}}$, reverses the loaded C-section transfer function amplitude, $|S_{21}|$, while keeping the transfer phase $\angle S_{21}$, and hence also the group delay, τ_{21}, unchanged, i.e.

$$|S_{21}(A_{\mathrm{L}}, \omega)| = \frac{1}{|S_{21}(1/A_{\mathrm{L}}, \omega)|}, \tag{3.20a}$$

$$\angle S_{21}(A_{\mathrm{L}}, \omega) = \angle S_{21}(1/A_{\mathrm{L}}, \omega),\ \tau_{21}(A_{\mathrm{L}}, \omega) = \tau_{21}(1/A_{\mathrm{L}}, \omega). \tag{3.20b}$$

Figure 3.11 shows the active C-section transfer group delays and amplitudes. We see that the equalized gain and loss pair exhibits identical group delay and symmetric amplitudes about $|S_{21}| = 0$ dB, thus confirming that the lumped active C-section, as a practical implementation of its distributed counterpart in Sec. 3.2, exhibits identical group delay and amplitude characteristics.

Apart from tuning the height of group delay peak, the position of group delay peak, ω_{r}, or resonance frequency, can be also tuned by varying the load transmission phase, ϕ_{L}, as shown in Fig. 3.12. The value of resonance frequency, ω_{r} is determined by using (3.15a).

3.4.2 Combining Gain-Loss Equalized C-Section Pair

An all-pass gain-loss equalized pair is formed by cascading a gain C-section and a loss C-section, as shown in Fig. 3.13, with appropriately tuned gain amplitude, $|T_{\mathrm{L,gain}}| = G$, and

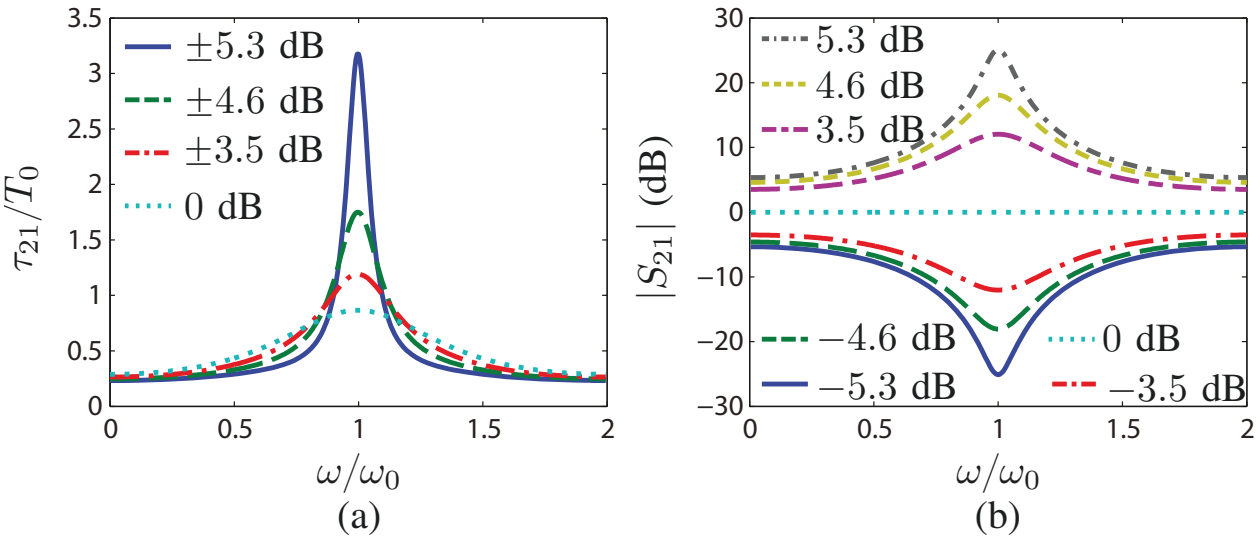

Figure 3.11 Simulated responses [Eq. 3.19] of active C-section with maximum coupling factor $k = -6$ dB ($k = 0.5$) at the coupler quarter wavelength frequency ω_0, resonance frequency $\omega_r = \omega_0$ ($\phi_L \equiv 0$) and varying load transfer amplitudes $A_L = \{0, \pm 3.5, \pm 4.6, \pm 5.3\}$ dB. (a) Normalized transfer group delays τ_{21}/T_0, $T_0 = 2\pi/\omega_0$. (b) Transfer amplitudes $|S_{21}|$. (L. Zou, et al [15], T-MTT, ©2017 IEEE)

loss amplitude, $|T_{L,loss}| = L$, such that $G = 1/L$. The group delay of the resulting gain-loss pair is twice that of a single gain or loss loaded C-section, as shown in Fig. 3.14(a), while the transfer amplitude becomes all-pass [Fig. 3.14(b)]. In addition to combining equalized gain loss amplitudes so as to provide an all-pass response, the gain and loss load elements must exhibit the same transfer phase, for all the reconfigurable states (i.e. all $|T_L|$'s). Any offset between the phases of the gain and loss elements, i.e. $\Delta\phi = \phi_{L,gain} - \phi_{L,loss} \neq 0$, results in different gain and loss resonance frequencies, $\omega_{r,gain} \neq \omega_{r,loss}$ according to (3.15a), which leads to fluctuations ($|S_{21}| \neq 1$) in the gain-loss pair transmission amplitude around the design resonance frequency, as will be shown in Sec. 3.4.3.

3.4.3 Prototype Design and Experimental Demonstration

Design of Active C-Section

For a practical design of active C-section, we shall also consider its matching ($|S_{11}|$ and $|S_{22}|$). Since the load is typically implemented using transistor, whose backward transmission coefficient is essentially 0 [$T_{L,B}$ in Fig. 3.9(b)], the excitation is practically only applied at port 1 of the active C-section, we thus only consider $|S_{11}|$ for practical matching design.

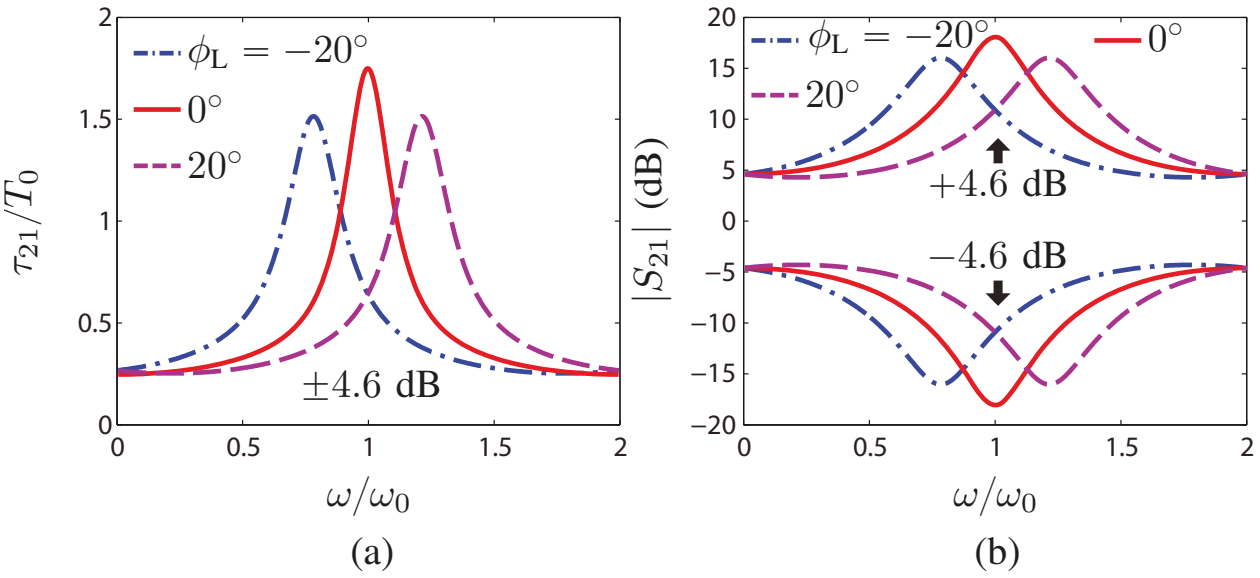

Figure 3.12 Simulated responses [Eq. 3.19] of active C-section with maximum coupling factor $k = -6$ dB ($k = 0.5$) at ω_0, $A_L = \pm 4.6$ dB, resonance frequency ω_r tuned by varying $\phi_L = \{-20°, 0°, 20°\}$. (a) Normalized transfer group delays τ_{21}/T_0, $T_0 = 2\pi/\omega_0$. (b) Transfer amplitudes $|S_{21}|$. (L. Zou, et al [15], T-MTT, ©2017 IEEE)

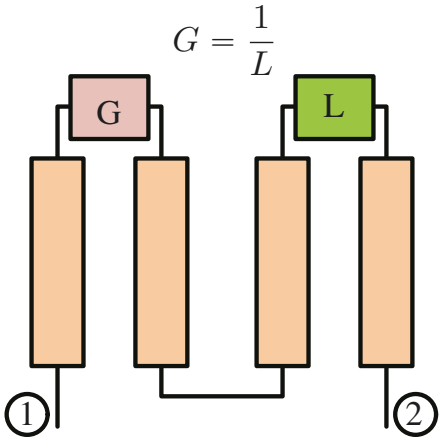

Figure 3.13 Proposed all-pass loss-gain equalized pair formed by cascading a gain loaded C-section and a loss loaded C-section, where the gain is the reverse of the loss, $G = 1/L$. (L. Zou, et al [15], T-MTT, ©2017 IEEE)

Ideally, if $R_C = F_C = R_{L,1} = 0$, S_{11} given by (3.12a) is always zero, and consequently, $|T_L|$ can be safely tuned toward the pole given by (3.15b).

In practice, however, R_C, F_C, $R_{L,1} \neq 0$, and $|S_{11}|$ has been shown in Fig. 3.10(a) that it may exceed 0 dB, i.e. reflection gain. In order to ensure satisfactory matching, one may adopt the

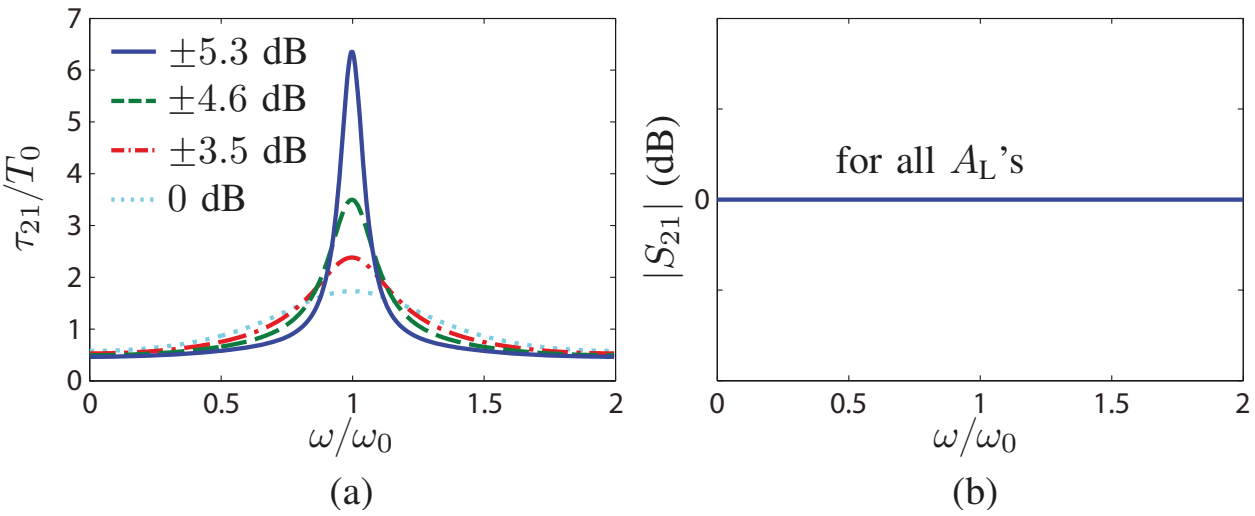

Figure 3.14 Simulated responses of the gain-loss equalized pair in Fig. 3.13 with maximum coupling factor $k = 0.5$ at ω_0, load transmission phase $\phi_L \equiv 0$ and different load transmission amplitudes $A_L = \{0, \pm 3.5, \pm 4.6, \pm 5.3\}$ dB. (a) Normalized group delay τ_{21}/T_0. (b) All-pass transfer amplitude $|S_{21}|$. (L. Zou, et al [15], T-MTT, ©2017 IEEE)

following strategies :

1. restricting the maximum load gain $|T_L|_{max}$ below the limit defined by (3.15b), which, however, limits the group delay tuning range ;
2. minimizing the non-idealities, R_C, F_C, $R_{L,1}$;

We have calculated that the combination of $|T_L|_{max} < 7$ dB, $|F_C| < -40$ dB, $|R_{L,1}| < -25$ dB for coupling $k = -10$ dB results in overall matching better than -20 dB and maximum group delay of around 3 ns.

The active C-section is implemented here in microstrip technology for easiest fabrication and testing. Unfortunately, due to their imperfect transverse electromagnetic nature, and corresponding unequal even and odd mode phase velocities ($v_o > v_e$), microstrip couplers suffer from relatively poor isolation [100] ($F_C \neq 0$). To minimize matching degradation due to non-zero F_C, one should thus increase the natural isolation of the coupler. Corresponding equalization of even and odd velocities may be achieved by different approaches [103–105], we use here capacitive compensation, which consists in inserting a coupling enhancing capacitance (0.3 pF here) in the gap between the two transmission lines, as shown in the fabricated microstrip coupler in Fig. 3.15(a).

The fabricated loss-gain load is shown in Fig. 3.15(b) with parts specifications. It is composed of the cascade of an internally matched variable gain-loss (VGL) chip, whose gain/loss is

tuned, on the same chip, by varying the control bias voltage, and a fixed stabilization and matching enhancement attenuator (ATT). Both the VGL internal matching and the ATT matching and attenuation contribute to the stability of the overall device.

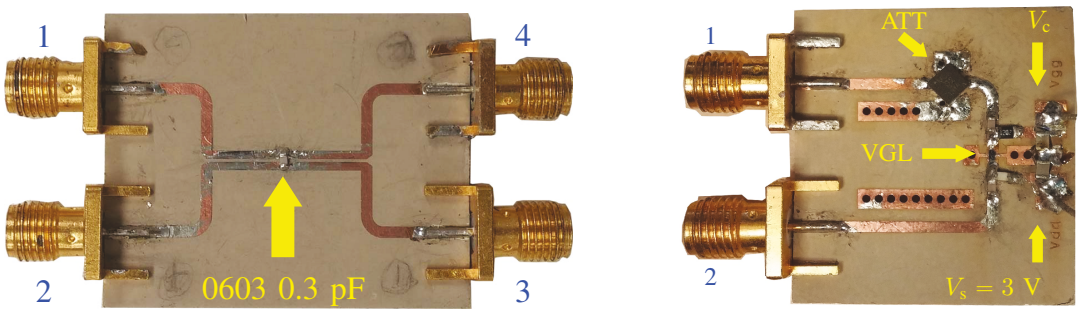

(a) (b)

Figure 3.15 Fabricated prototypes of coupler and the load on Rogers RO6010 50 mil substrate with $\epsilon_r = 10.2$, 0.5 oz cladding. (a) Capacitance compensated, even-odd mode phase velocity equalized microstrip coupler (b) Variable gain loss (VGL) load composed a VGL chip (Avago VMMK-3503 : internal matching, $0.5 - 18$ GHz operation, from 12 dB gain to 11 dB loss, 23 dB tuning range by varying V_c from 1.8 V to 0.65 V) and a fixed matching enhancement attenuator ATT (Minicircuit GAT-4+ : 4 dB attenuation). (L. Zou, et al [15], T-MTT, ©2017 IEEE)

We perform all the measurements for the prototypes shown in this chapter by using the TRL calibration technique [106] to eliminate the influence by the connectors, which typically introduces error in phase (group delay) measurement. The capacitive compensation [Fig. 3.15(a)] used here is restricted to a single frequency, which is here designed to be 2.5 GHz. Consequently, the bandwidth is limited to the range $2.4 - 2.65$ GHz around 2.5 GHz, where the targeted isolation, $|F_C| < -40$ dB, is guaranteed, the backward coupling coefficient is -10 dB at the designed frequency. The attenuator based stabilization [Fig. 3.15(b)] used here ensures the load matching ($|R_{L,1}|$) to be smaller than -25 dB and the maximum load gain ($|T_{L,F}|_{max} = 6.7$ dB here) to be smaller than 7 dB in the satisfactory coupler isolation frequency range ($2.4 - 2.65$ GHz). Moreover, it is found that the maximum load phase variation corresponding to different gains and losses is within 5°, i.e.

$$\max[\Delta\phi_L(|T_{L,F}|)] = \phi_L|_{|T_{L,F}|=6.7\text{ dB}} - \phi_L|_{|T_{L,F}|=-6.7\text{ dB}} < 5°. \tag{3.21}$$

The corresponding effect of $\Delta\phi_L$ on gain-loss amplitude equalization will be shown in the next subsection.

Figure 3.16 shows the fabricated active C-section, where the resonance frequency, ω_r, can be

tuned by adjusting the electrical length (ϕ_L) of the load so as to satisfy (3.15a).

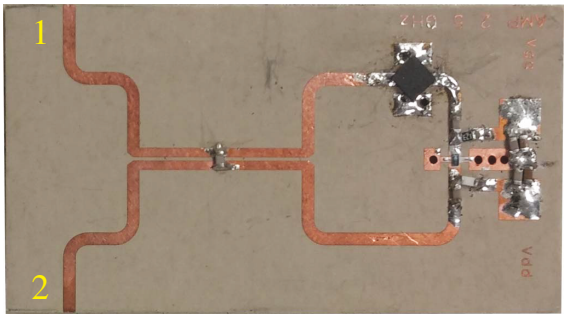

Figure 3.16 Fabricated loaded active C-section with the coupler and the load (ϕ_L may be different) in Fig. 3.15. (L. Zou, et al [15], T-MTT, ©2017 IEEE)

The corresponding measured amplitudes and group delays, with varied load loss and gain, are plotted in Fig. 3.17. Consistently with the analysis presented in Sec. 3.4.1, the forward transmission amplitudes are symmetric about 0 dB while the group delays are identical.

Combined Gain-Loss C-Section Pair

Figure 3.18 shows the fabricated equalized gain-loss C-section pair. The corresponding measured amplitudes and group delays, with varied load Loss and gain, are plotted in Fig. 3.19. Consistently with the analysis presented in Sec. 3.4.2, the combined pair transfer amplitudes are nearly flat while combined pair group delays are twice of the gain or loss C-section [compare to Fig. 3.17(b)]. Moreover, the fluctuation of $|S_{21}|$ (within ± 1 dB) near the resonance frequency (2.45 GHz), shown in Fig. 3.18(b), is attributed to the offset (within 5°) between the gain and loss load transmission phases, as discussed in Sec. 3.4.2 in (3.21).

Group Delay Engineered Reconfigurable Cascade Gain-Loss Phaser

Cascading gain-loss C-section pairs tuned at different resonance frequencies allows to synthesize reconfigurable group delay responses in real time with all-pass amplitude response over a certain bandwidth. To demonstrate this, we fabricated three gain-loss equalized pairs, tuned at $\omega_{r1} = 2.35$, $\omega_{r2} = 2.45$ and $\omega_{r3} = 2.6$ GHz, respectively, by adjusting the load lengths so as to satisfy (3.15a). The experimental setup and complete device under test are shown in Fig. 3.20. The 3-unit reconfigurable phaser is formed by cascading the three gain-loss equalized C-section pairs. The scattering matrix and group delay were measured on a vector network analyzer. The two power supplies provide a source voltage of $V_s = 3$ V, and a control voltage of V_c, respectively.

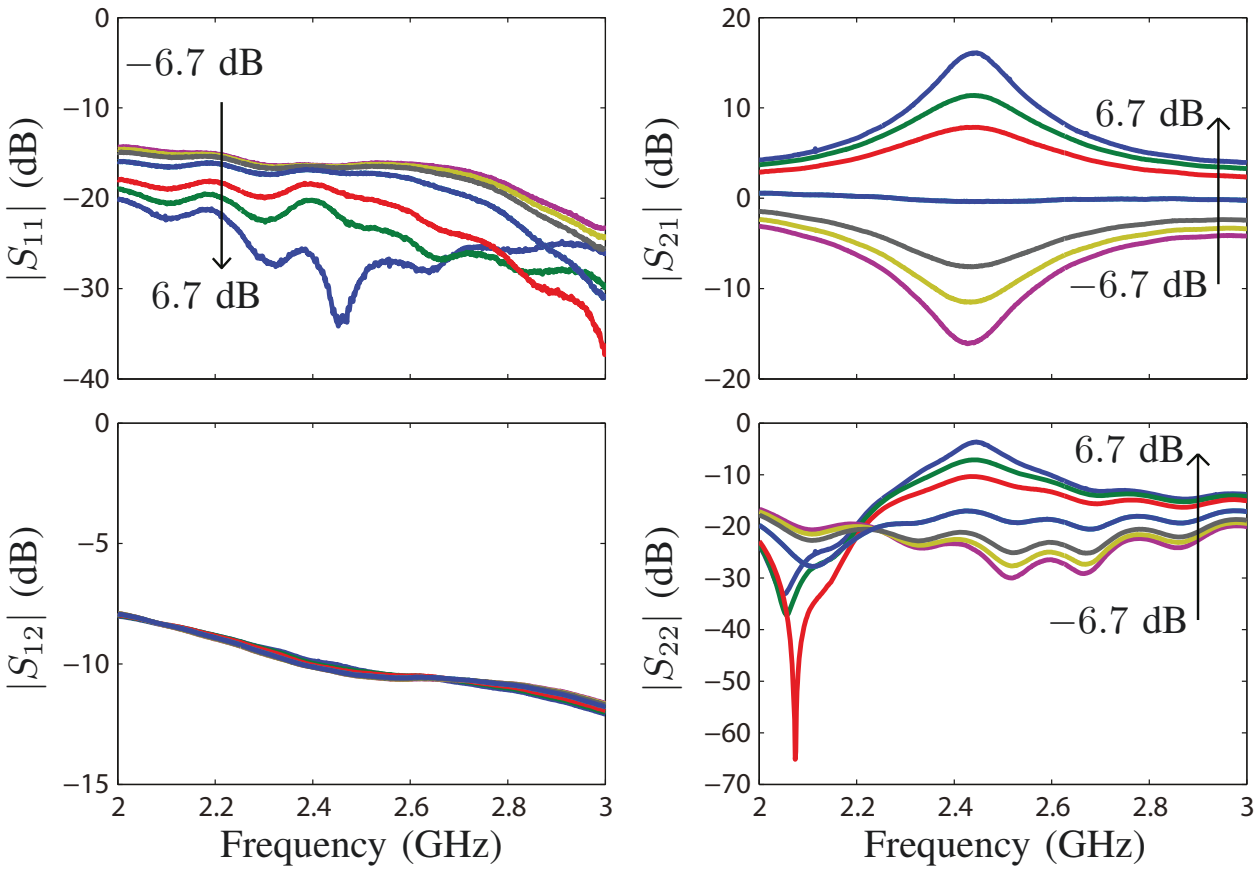

(a)

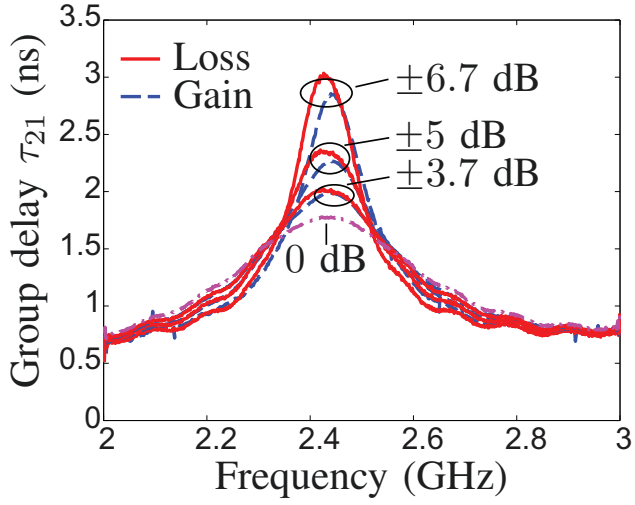

(b)

Figure 3.17 Measured responses of the active C-section in Fig. 3.16 with varying gains and losses $|T_{\mathrm{L}}| = \{0, \pm 3.7, \pm 5, \pm 6.7\}$ dB. (a) Amplitudes. (b) Group delays. (L. Zou, et al [15], T-MTT, ©2017 IEEE)

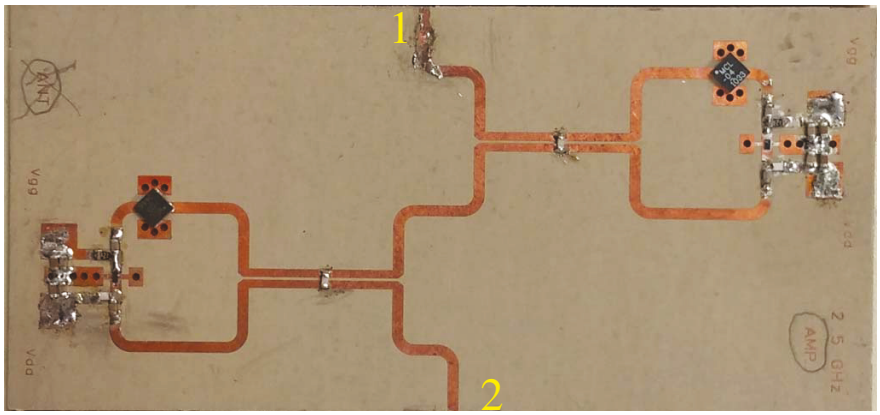

Figure 3.18 Fabricated equalized gain-loss C-section pair composed of two of the active C-sections in Fig. 3.16 with equalized gain and loss, respectively. (L. Zou, et al [15], T-MTT, ©2017 IEEE)

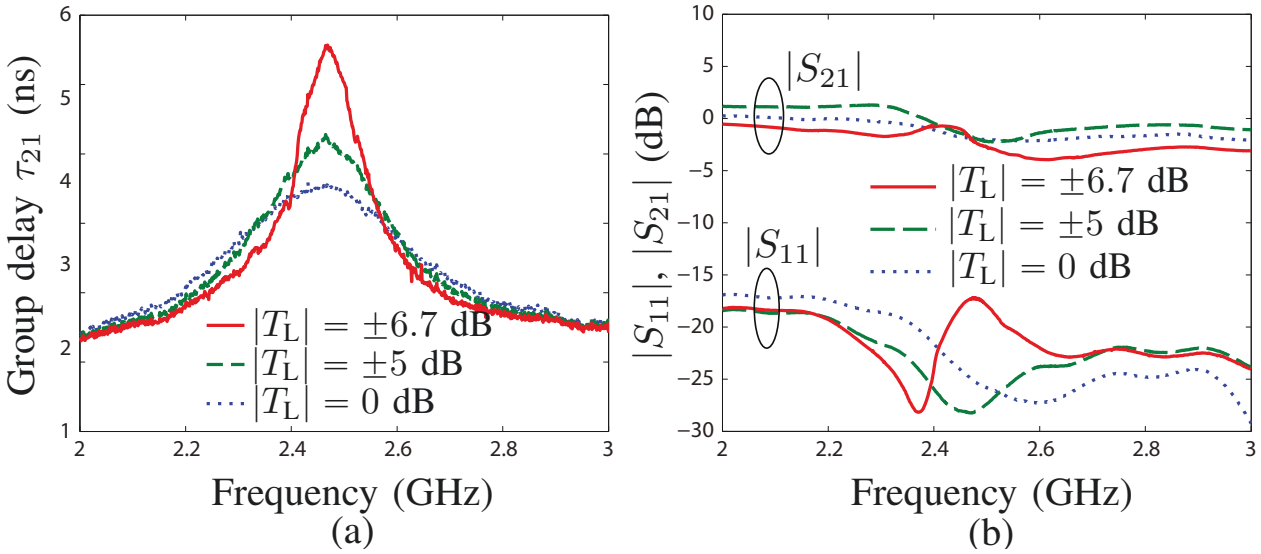

Figure 3.19 Measured responses of the gain-loss C-section pair in Fig. 3.18. (a) Group delays. (b) Amplitudes. (L. Zou, et al [15], T-MTT, ©2017 IEEE)

In Fig. 3.21 the control voltages (V_c) of the 3 gain-loss pairs (6 voltages in all) are tuned (by the potential meters) to produce up-chirp and down-chirp linear group delay responses [6], with 5 ns/GHz and -12 ns/GHz slopes, respectively. This demonstrates the central point of the gain-loss equalized phaser : the group delay response of the gain-loss equalized phaser can be reconfigured in real time with essentially all-pass transfer amplitude.

We shall now study the design flexibility that is available in tuning the group delay slope. First we shall keep in mind that the maximum achievable positive slope in an gain-loss

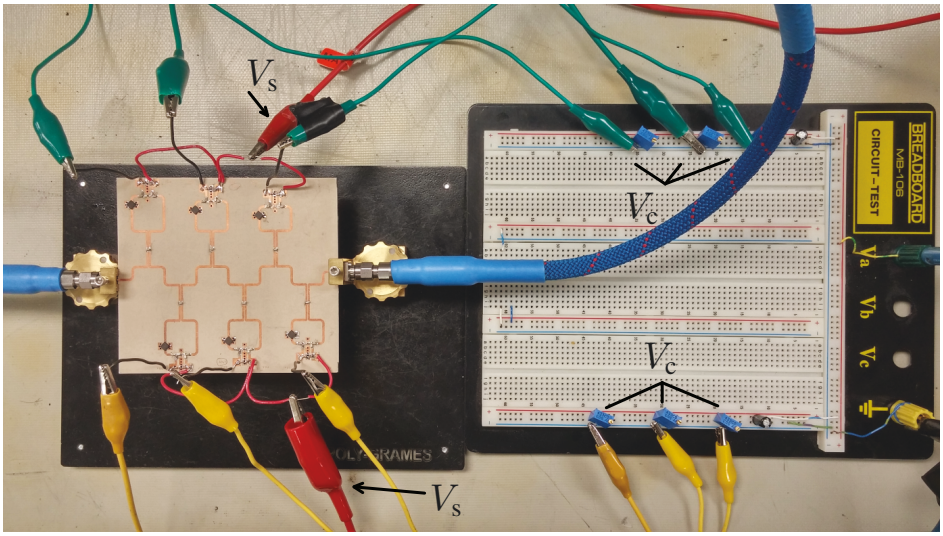

Figure 3.20 Experimental setup and device under test, where a 3-unit gain-loss reconfigurable phaser is formed by cascading three gain-loss equalized C-section pairs tuned at $\omega_{r1} = 2.35$, $\omega_{r2} = 2.45$ and $\omega_{r3} = 2.6$ GHz, respectively. (L. Zou, et al [15], T-MTT, ©2017 IEEE)

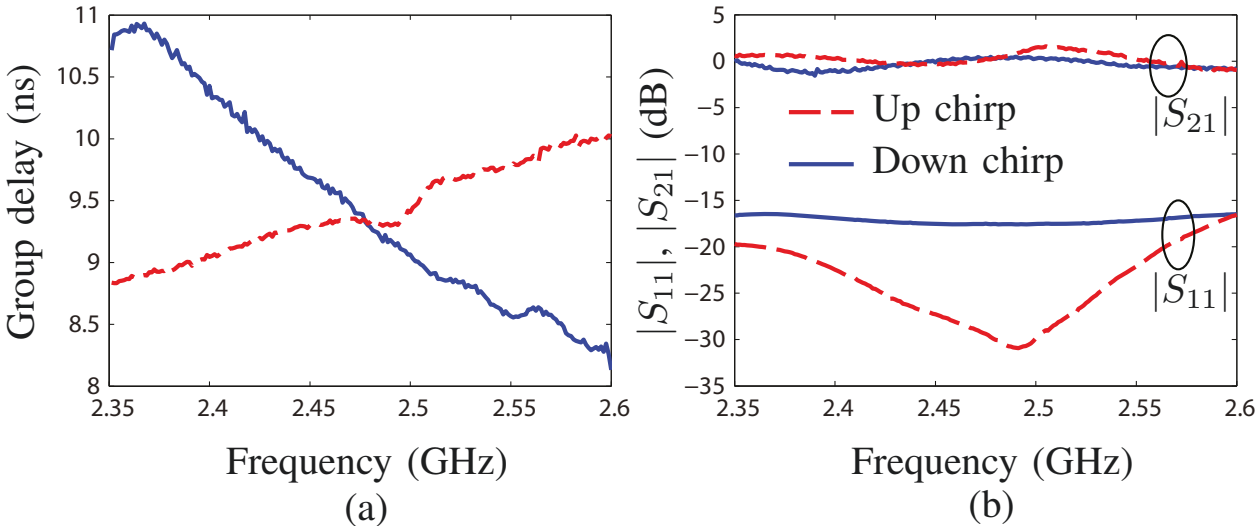

Figure 3.21 Experimental setup and device under test, where a 3-unit gain-loss reconfigurable phaser is formed by cascading three gain-loss equalized C-section pairs tuned at $\omega_{r1} = 2.35$, $\omega_{r2} = 2.45$ and $\omega_{r3} = 2.6$ GHz, respectively. (L. Zou, et al [15], T-MTT, ©2017 IEEE)

phaser is always less than the maximum negative slope. Indeed, the maximum and minimum achievable group delays, corresponding to maximum and zero gain/loss, respectively, are always higher for C-sections tuned at lower frequencies, since these frequencies correspond to larger load lengths, and hence larger overall group delay. As a result, the maximal group

delay slope (or swing) is necessarily less for positive chirp than for negative chirp responses. This is graphically illustrated in Fig. 3.22 for the GL phasers (2.35 and 2.6 GHz).

An estimation of the maximum achievable positive (negative) slope, $\sigma^{+}_{\max}$ ($\sigma^{-}_{\max}$), for a given gain-loss phaser is the difference between the maximum (minimum) peak at high frequency and the minimum (maximum) peak at low frequency divided by the operation bandwidth, i.e. in the case of Fig. 3.22,

$$\sigma^{+}_{\max} = \frac{5.4 - 3.71}{2.6 - 2.35} = 6.76 \text{ ns/GHz}, \tag{3.22a}$$

$$\sigma^{-}_{\max} = \frac{3.31 - 7.32}{2.6 - 2.35} = -16.04 \text{ ns/GHz}. \tag{3.22b}$$

The minimum group delay slope would be zero, corresponding to the summation of group delays with equal height.

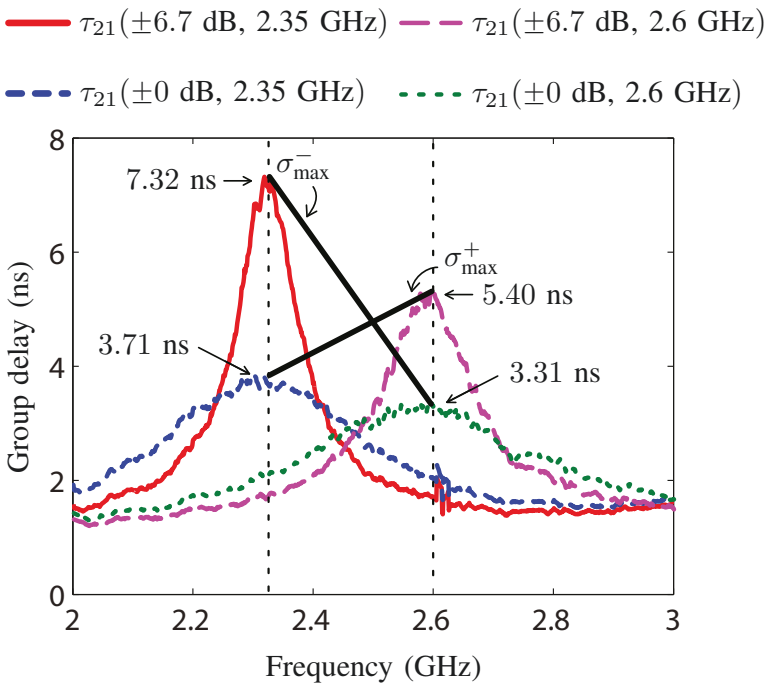

Figure 3.22 Measured gain-loss pair group delays corresponding to maximum gain-loss (±6.7 dB, high peak) and zero gain-loss (low peak), for the 2.35 and 2.6 GHz gain-loss C-section pairs. (L. Zou, et al [15], T-MTT, ©2017 IEEE)

Figure 3.23 shows group delay slopes other than those shown in Fig. 3.21(a), within the range given by (3.22). Relaxing the slope limitation requires adding sections, especially at high or low frequencies, for larger positive or larger negative slope, respectively.

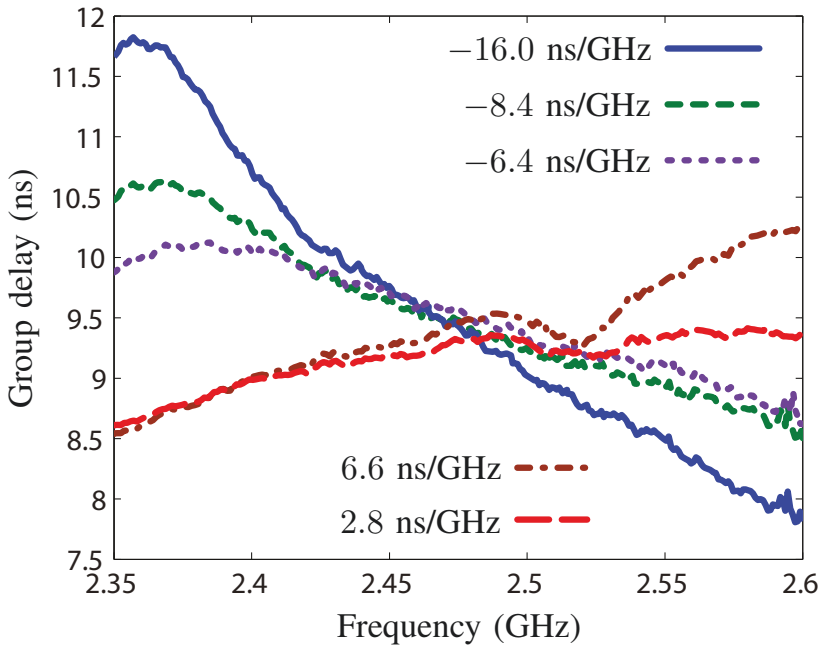

Figure 3.23 Different measured group delay slopes, σ's [$\sigma = (\tau_{\max} - \tau_{\min})/B$ with bandwidth B], obtained by the fabricated gain-loss equalized phaser in Fig. 3.20. (L. Zou, et al [15], T-MTT, ©2017 IEEE)

Finally, the group delay linearity may be improved by adding sections tuned between the high and low frequencies for better curve-fitting the specified group delay shapes, as is also the case in purely passive structures.

3.5 Noise Figure Characterization

3.5.1 Loaded C-Section Noise Figure

We shall first compute the noise figure of a single loaded C-section, with the aid of Fig. 3.24, where we assume the coupler is lossless and hence only the load contributes to noise generation. The noise powers added by the load, $N_{\text{add,L}}$ (without feedback) and by the loaded C-section, N_{add}, are

$$N_{\text{add,L}} = kBT_{\text{e,L}}, \tag{3.23a}$$

$$N_{\text{add}} = kBT_{\text{e}}, \tag{3.23b}$$

respectively, where $k = 1.38 \times 10^{-23}$ J/K is the Boltzmann constant, B is the bandwidth, $T_{\text{e,L}} = (NF_{\text{L}} - 1)T_0$ is the load equivalent noise temperature, and $T_{\text{e}} = (NF - 1)T_0$ is the loaded C-section equivalent noise temperature, with NF_{L} and NF being the load and C-

section noise figures, respectively, and $T_0 = 290$ K being the environment temperature.

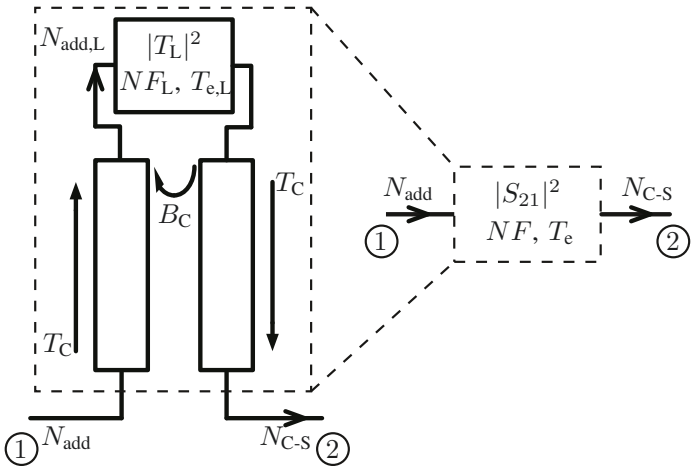

Figure 3.24 Graphical aid for the calculation of the noise figure of a single loaded C-section. (L. Zou, et al [15], T-MTT, ©2017 IEEE)

The noise power generated by the loaded C-section, $N_{\text{C-S}}$, is then the C-section added noise power, N_{add}, multiplied by the squared magnitude of the C-section transfer function, given by (3.17), which depends itself on the load added noise power, $N_{\text{add,L}}$, i.e.

$$\begin{aligned} N_{\text{C-S}} &= N_{\text{add}}|S_{21}|^2 \\ &= N_{\text{add,L}}|T_{\text{L}}T_{\text{C}} + T_{\text{L}}B_{\text{C}}T_{\text{L}}T_{\text{C}} + T_{\text{L}}B_{\text{C}}^2T_{\text{L}}^2T_{\text{C}} + \ldots|^2 \\ &= N_{\text{add,L}}\left|\frac{T_{\text{L}}T_{\text{C}}}{1 - T_{\text{L}}B_{\text{C}}}\right|^2. \end{aligned} \tag{3.24}$$

Inserting (3.23a) and (3.23b) into the right-hand side of the third and first equality in (3.24), respectively, leads to

$$T_{\text{e}} = T_{\text{e,L}}\frac{1}{|S_{21}|^2}\left|\frac{T_{\text{L}}T_{\text{C}}}{1 - T_{\text{L}}B_{\text{C}}}\right|^2, \tag{3.25}$$

from which the loaded C-section noise figure is obtained as

$$\begin{aligned} NF &= 1 + \frac{T_{\text{e}}}{T_0} \\ &= 1 + \frac{T_{\text{e,L}}}{T_0}\frac{1}{|S_{21}|^2}\left|\frac{T_{\text{L}}T_{\text{C}}}{1 - T_{\text{L}}B_{\text{C}}}\right|^2 \\ &= 1 + (NF_{\text{L}} - 1)\frac{1}{|S_{21}|^2}\left|\frac{T_{\text{L}}T_{\text{C}}}{1 - T_{\text{L}}B_{\text{C}}}\right|^2. \end{aligned} \tag{3.26}$$

As will be shown later, only the gain-loaded C-section plays a significant role in the C-

section pair. The noise figure of the gain-loaded C-section may be calculated as follows. Since $|T_{\mathrm{L,gain}}| > 1$ and, typically $|B_{\mathrm{C}}| < -10$ dB (loose coupling) and $|T_{\mathrm{C}}| \approx 1$, Eq. (3.17) reduces to

$$S_{21} \approx \frac{T_{\mathrm{L,gain}} T_{\mathrm{C}}^2}{1 - T_{\mathrm{L,gain}} B_{\mathrm{C}}}. \tag{3.27}$$

Hence (3.26) reduces to

$$NF_{\mathrm{gain}} \approx 1 + \frac{NF_{\mathrm{L,gain}} - 1}{|T_{\mathrm{C}}|^2} \approx NF_{\mathrm{L,gain}}, \tag{3.28}$$

where the last approximation follows from $|T_{\mathrm{C}}| \approx 1$. Another special case here is the loss C-section noise figure, which, given the passive nature of loss C-section, is [98]

$$NF_{\mathrm{L,loss}} = \frac{1}{|T_L|^2}, \tag{3.29a}$$

$$NF_{\mathrm{loss}} = \frac{1}{|S_{21,\mathrm{loss}}|^2}. \tag{3.29b}$$

Figure 3.25 shows the loaded C-section noise figures obtained by (3.26), and compared against ADS circuit simulation results. The perfect agreement validates (3.26). Moreover, the gain noise figure, NF_{gain} is very close to $NF_{\mathrm{L,gain}} = 3$ dB, which validates the approximation made in (3.28).

3.5.2 Gain-Loss Pair Noise Figure

For best overall noise performance, the first stage should have a low noise figure and high gain [98]. Therefore, we place the gain section before loss section, and find the gain-loss pair noise figure as [98]

$$\begin{aligned} NF_{\mathrm{pair}} &= NF_{\mathrm{gain}} + \frac{NF_{\mathrm{loss}} - 1}{|S_{21,\mathrm{gain}}|^2} \\ &= NF_{\mathrm{gain}} + \frac{1/|S_{21,\mathrm{loss}}|^2 - 1}{|S_{21,\mathrm{gain}}|^2} \\ &= NF_{\mathrm{gain}} + \left(1 - \frac{1}{|S_{21,\mathrm{gain}}|^2}\right) \\ &\approx NF_{\mathrm{L,gain}} + 1, \end{aligned} \tag{3.30}$$

where (3.29b) and the identity (3.20a) has been used in the second and third equality, respectively, and (3.28) has been used in the last approximation, indicating that the the contribution to the overall gain-loss pair noise figure comes from the gain section.

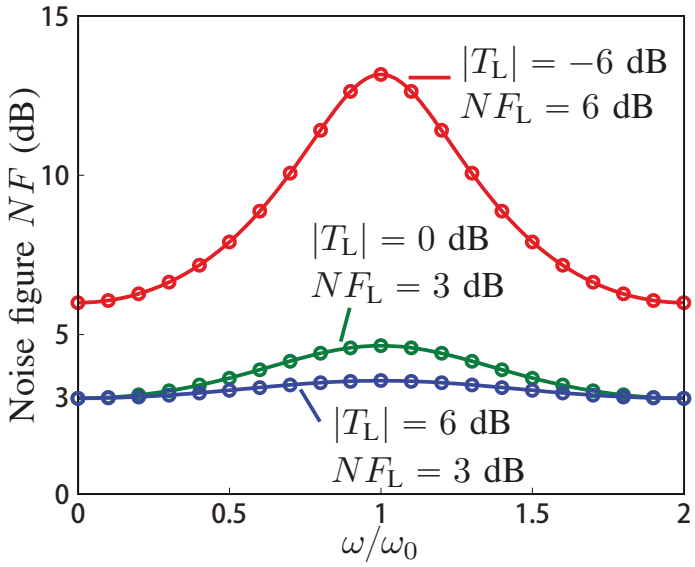

Figure 3.25 Loaded C-section (coupling factor $k = -10$ dB) noise figures corresponding to different load transfer functions, $T_{\rm L}$'s, and load noise figures, $NF_{\rm L}$'s. Circles : ADS circuit simulation results, solid lines : analytical results corresponding to (3.26). (L. Zou, et al [15], T-MTT, ©2017 IEEE)

3.5.3 N-Cascaded Gain-Loss Pairs Noise Figure

Next, we consider the cascade of N gain-loss pairs. The total noise figure is [98]

$$\begin{aligned} NF_{\rm casc} =& NF_{\rm pair1} + \frac{NF_{\rm pair2} - 1}{|S_{21,\rm pair1}|^2} + \frac{NF_{\rm pair3} - 1}{|S_{21,\rm pair1}|^2 |S_{21,\rm pair2}|^2} + \dots \\ =& -(N-1) + \sum_{n=1}^{N} NF_{\rm pair(n)}, \end{aligned} \tag{3.31}$$

where the identity $|S_{21,\ \rm pair(n)}| = 1$ has been used. Inserting (3.30) into (3.31) yields

$$NF_{\rm casc} = \sum_{n=1}^{N} NF_{\rm L,gain(n)} + 1. \tag{3.32}$$

One may naturally optimize the gain load noise figure for minimum overall noise figure. A more efficient approach would be to connect a high gain low noise amplifier before the overall cascade device [98].

3.5.4 Dynamic Range of the Fabricated ASP

The noise floor, N_{floor}, is equivalent to the added noise of the cascaded ASP, corresponding to

$$N_{\text{floor}} = N_{\text{add,casc}} = kBT_{\text{e,casc}} = kB(NF_{\text{casc}} - 1)T_0, \tag{3.33}$$

and the system dynamic range extends from the noise floor, defined by (3.33), to the input 1 dB compression point of the ASP.

For the fabricated ASP, shown in Fig. 3.20, the gain load is the cascade of a 4 dB attenuator (4 dB noise figure) and a 3.5 dB noise figure amplifier, corresponding to the gain load noise figure $NF_{\text{gain}(n)} = 5.6234$ (7.5 dB) [98] for $n = 1, 2, 3$. Thus, the cascade noise figure is

$$NF_{\text{casc}} \approx 3 \cdot NF_{\text{gain}(n)} + 1 = 17.87, \tag{3.34}$$

contributing to the noise floor given by

$$\begin{aligned} N_{\text{floor}} &= kBT_0(NF_{\text{casc}} - 1) \\ &= 1.38 \times 10^{-23} \times 250 \times 10^6 \times 290 \times (17.87 - 1) \\ &= 1.5875 \times 10^{-11} \text{ W} = -78 \text{ dBm}. \end{aligned} \tag{3.35}$$

Denoting S_{i} the input signal power of the cascade ASP, the power reaching the amplifier, $P_{\text{in, AMP}}$, is

$$P_{\text{in, AMP}} = S_{\text{i}} \cdot |T_{\text{C}}|^2 \cdot |S_{21,\text{ATT}}|^2. \tag{3.36}$$

This power should be smaller than the amplifier 1 dB compression point P_{1dB}, which is here 0 dBm according to Fig. 7 in the datasheet of Avago VMMK-3503. Given $|T_{\text{C}}|^2 \approx 1$ and $|S_{21,\text{ ATT}}|^2 = 4$ dB, the upper limit of the input power is found as

$$S_{\text{i}} < \frac{P_{\text{1dB}}}{|S_{21,\text{ATT}}|^2} = 4 \text{ dBm}. \tag{3.37}$$

Finally, the input power dynamic range, given by

$$-78 \text{ dBm} < S_{\text{i}} < 4 \text{ dBm},$$

is found as 82 dB.

3.6 Summary and Perspective

This Chapter first shows the amplitude imbalance issue for an all-pass phaser, because the loss is proportional the the group delay for any natural passive phaser. Then, the gain-loss equalized concept is introduced for real all-pass amplitude and reconfigurable group delay. A practical lumped active loaded C-section implementation of such gain/loss C-section is proposed, analyzed, and experimentally demonstrated, to show the capability of equalizing amplitude and tuning group delay function in real time. Note that it not only solves the amplitude imbalance issue associated with passive phaser, also its group delay swing can be enhanced by tuning values of the gain-loss pair.

It will enable radio analog signal processing (R-ASP) systems requiring dynamic adaptability, as for instance dispersion code multiple access (DCMA) [16]. Also, it is found that for a single loaded active C-section, its transfer function is similar to that of a integrator [107], when the load is gain ; similar to that of a differentiator [108], when the load is loss. Moreover, the gain/loss equalized C-section pair exhibits Hilbert transform [109] like transfer function. Therefore, active phaser may find applications for various mathematical operations.

CHAPTER 4 DISPERSION CODE MULTIPLE ACCESS (DCMA) CONCEPT AND PROOF-OF-CONCEPT FOR HIGH-SPEED WIRELESS COMMUNICATIONS

Part of this chapter is excerpt from the author's works, [16] and [4].

4.1 Introduction

High-speed wireless communications require large spectral resources, i.e. ultra wide bandwidth (UWB), available only towards the higher range of the microwave spectrum. For instance, 5G communication systems will operate in the millimeter-wave regime [110–112]. Unfortunately, currently existing low-frequency and small-bandwidth standards are not directly transposable to millimeter-wave and THz systems [21, 113], and it is therefore highly desirable to explore other UWB technologies.

Impulse Processing (IP) is a particularly promising UWB technology for high-speed wireless communications given its frequency scalability and transceiver simplicity with typical carrierless transmitter and non-coherent receiver. Combining IP-UWB with an efficient *multiple access technique* allows accommodating more simultaneous users and hence higher spectral efficiency. Conventional IP multiple access techniques include time hopping and frequency hopping. IP time hopping multiple access divides time frames into multiple user chips and distributes these chips according to a time hopping code to minimize error probabilities [114, 115]. However, this technique typically requires digital processing, which impairs its frequency scalability. A purely analog IP frequency hopping multiple access has been exclusively used in optics so far. This analog technique consists in rearranging the spectral contents of signals in time, using dispersion controlled devices such as Bragg fiber gratings [9], so as to encode ultra-short pulses according to a dispersive time-frequency mapping scheme [116–118]. The purely analog nature of this technique attractively leads to real-time processing, and hence low signal latency and high-speed transmission. However, its application to radio signal typically requires a microwave photonics approach [119], which involves lossy, complex, expensive and non-integrable electro-optical technology.

Radio Real-time Analog Signal Processing (RR-ASP) represents a promising alternative to IP-UWB technology for wireless communications [6]. The radio Dispersion Code Multiple Access (DCMA) has been reported in [80, 101] as an efficient RR-ASP UWB multiple access technique. DCMA may be considered as the wireless and radio counterpart of Bragg grating

based multiple access [116] in optics. This chapter introduces the DCMA concept mathematically and demonstrates a prototype DCMA system experimentally. The chapter is organized as follows. First, Sec. 4.2 conceptually and mathematically describes a general DCMA system. Next, Sec. 4.3 introduces the Chebyshev coding as a convenient coding scheme for DCMA. Then, Sec. 4.4 provides the experimental proof-of-concept of a DCMA system in a LOS configuration.

4.2 DCMA Concept

4.2.1 Principle of Operation and Notation

Figure 4.1 shows the conceptual schematic of a DCMA system composed of N transmitter-receiver (TX-RX) pairs, which may be placed anywhere. The signal sent from TX_i is a modulated UWB pulse train, $s_i(t)$. This signal is encoded by the corresponding phaser into the new signal $e_i(t)$, which is intended to be received by RX_i as $r_i(t)$. To ensure such transmission from TX_i to RX_i, the corresponding encoding and decoding phaser transfer functions must be assigned a pair of group delay frequency functions (dispersion codes), $\tau_{\mathrm{TX}i}(\omega)$ and $\tau_{\mathrm{RX}i}(\omega)$, that are matched (or phase-conjugated), i.e.

$$\tau_{\mathrm{TX}i}(\omega) + \tau_{\mathrm{RX}i}(\omega) = \text{constant}. \tag{4.1}$$

The system operates in a wireless environment, whose channel, that is generally based on statistical model, may be described by the transfer function

$$C_{ik}(\omega) = \mathcal{F}[c_{ik}(t)], \quad i,k \in \{1,2,\ldots,N\}, \tag{4.2}$$

between TX_k and RX_i, where $c_{ik}(t)$ is the corresponding impulse response and $\mathcal{F}$ represents the Fourier transform operation. , When all of the N pairs are simultaneously active, the decoding phaser at RX_i recovers the desired signal, $\tilde{s}_i(t)$, which is a distorted replica of $s_i(t)$ due to both channel fading and interference originating from the $N-1$ undesired transmitters, $x_i(t)$, called multiple access interference (MAI).

4.2.2 Mathematical Description

In this section, we shall provide the mathematical description of the overall DCMA system operation. A matched pair of dispersion codes, corresponding to (4.1), may be expressed as

$$\tau_{\mathrm{TX}_i}(\omega) = \tau_0 + \tau_i(\omega), \tag{4.3a}$$

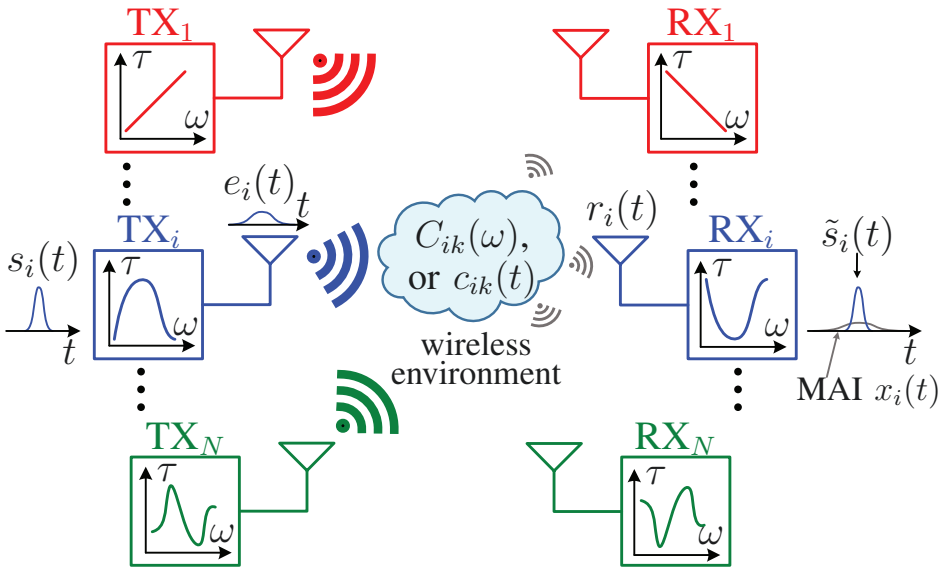

Figure 4.1 Schematic representation of an $N \times N$ dispersion code multiple access (DCMA) communication system (L. Zou, et al [16], TWC, © [2017] IEEE).

$$\tau_{\mathrm{RX}_i}(\omega) = \tau_0 - \tau_i(\omega). \tag{4.3b}$$

Assuming bandwidth-limited (e.g. bandpass) and lossless phasers, the corresponding transfer functions may be written

$$H_{\mathrm{TX}_i}(\omega) = \mathrm{rect}\left(\frac{\omega - \omega_0}{\Delta\omega}\right) e^{-j\omega\tau_0} e^{j\phi_i(\omega)}, \tag{4.4a}$$

$$H_{\mathrm{RX}_i}(\omega) = \mathrm{rect}\left(\frac{\omega - \omega_0}{\Delta\omega}\right) e^{-j\omega\tau_0} e^{-j\phi_i(\omega)}, \tag{4.4b}$$

where $\phi_i(\omega) = -\int_{\omega_0-\Delta\omega/2}^{\omega} \tau_i(\omega')\, d\omega'$ is a dispersive (non-linear) phase function of frequency, and $\omega_0 = 2\pi f_0$ and $\Delta\omega = 2\pi\Delta f$ are center frequency and bandwidth, respectively, of the system.

The signal arriving at RX_i is

$$R_i(\omega) = \left(\sum_{k=1}^{N} E_k C_{ik}\right)(\omega) + N(\omega) = \left(\sum_{k=1}^{N} S_k H_{\mathrm{TX}_k} C_{ik}\right)(\omega) + N(\omega), \tag{4.5}$$

which is the sum of the encoded signals from all the transmitters propagated through their respective channels plus noise $N(\omega)$. One finds the decoded signal by multiplying (4.5) with

$H_{\mathrm{RX}_i}(\omega)$, i.e.

$$Z_i(\omega) = H_{\mathrm{RX}_i}(\omega)\left(\sum_{k=1}^{N} S_k H_{\mathrm{TX}_k} C_{ik}\right)(\omega) + N(\omega) = \tilde{S}_i(\omega) + X_i(\omega) + N(\omega), \tag{4.6a}$$

with

$$\tilde{S}_i(\omega) = \left(S_i H_{ii} C_{ii}\right)(\omega), \tag{4.6b}$$

$$X_i(\omega) = \left[\sum_{\substack{k=1 \\ k\neq i}}^{N} S_k H_{ik} C_{ik}\right](\omega). \tag{4.6c}$$

The cascaded transfer functions (excluding the channel response) from TX_i to RX_i, $H_{ii}(\omega)$ and from TX_k to RX_i, $H_{ik}(\omega)$ are the product of (4.4b) and (4.4a) with i replaced by k for $H_{ik}(\omega)$, leading to

$$H_{ii}(\omega) = (H_{\mathrm{TX}_i} H_{\mathrm{RX}_i})(\omega) = \mathrm{rect}\left(\frac{\omega-\omega_0}{\Delta\omega}\right) e^{-j\omega(2\tau_0)}, \tag{4.7a}$$

$$H_{ik}(\omega) = (H_{\mathrm{TX}_k} H_{\mathrm{RX}_i})(\omega) = \mathrm{rect}\left(\frac{\omega-\omega_0}{\Delta\omega}\right) e^{j\phi_{ik}(\omega)}, \tag{4.7b}$$

with cascaded phase

$$\phi_{ik}(\omega) = -\int_{\omega_0-\Delta\omega/2}^{\omega} \tau_{ik}(\omega')d\omega', \quad k \neq i, \tag{4.8}$$

and the cascaded group delay $\tau_{ik}(\omega)$ is the sum of (4.3b) and (4.3a) for i replaced by k, i.e.

$$\tau_{ik}(\omega) = \tau_{\mathrm{TX}_k}(\omega) + \tau_{\mathrm{RX}_i}(\omega) = 2\tau_0 + \tau_k(\omega) - \tau_i(\omega), \ k \neq i. \tag{4.9}$$

The corresponding cascaded impulse responses are then

$$h_{ii}(t) = \mathcal{F}^{-1}\left[H_{ii}(\omega)\right] = 2\Delta f \frac{\sin[\pi\Delta f(t-2\tau_0)]}{\pi\Delta f(t-2\tau_0)} \cos[2\pi f_0(t-2\tau_0)], \tag{4.10a}$$

whose envelope is the sinc function and peak amplitude, at $t = 2\tau_0$, is proportional to the system bandwidth (Δf), and

$$h_{ik}(t) = \mathcal{F}^{-1}\left[H_{ik}(\omega)\right] = (h_{\mathrm{TX}_k} * h_{\mathrm{RX}_i})(t), \tag{4.10b}$$

where "$*$" denotes the convolution product, and $h_{\mathrm{TX}_k}(t)$ $h_{\mathrm{RX}_i}(t)$ are the impulse responses of the corresponding encoding and decoding phasers, respectively.

The waveform corresponding to $Z_i(\omega)$ in (4.6a) is thus

$$z_i(t) = \mathcal{F}^{-1}\left[Z_i(\omega)\right] = \tilde{s}_i(t) + x_i(t) + n(t), \tag{4.11a}$$

with

$$\tilde{s}_i(t) = \mathcal{F}^{-1}\left[\tilde{S}_i(\omega)\right] = s_i(t) * h_{ii}(t) * c_{ii}(t), \tag{4.11b}$$

$$x_i(t) = \mathcal{F}^{-1}\left[X_i(\omega)\right] = \sum_{\substack{k=1 \\ k\neq i}}^{N} s_k(t) * h_{ik}(t) * c_{ik}(t), \tag{4.11c}$$

and $n(t)$ typically being Additive White Gaussian Noise (AWGN), whose time sample value n is normal distribution random variable with zero mean and power σ_{N}^2 (variance), i.e. $n = \mathcal{N}\left(0, \sigma_{\mathrm{N}}^2\right)$. Throughout the the chapter, all the plotted impulse responses and time-domain signals are normalized by the peak of $h_{ii}(t)$, $2\Delta f$, as

$$\hat{h}_{ik}(t) = \frac{h_{ik}(t)}{2\Delta f},\ \forall\, i,k,\ \hat{z}_i(t) = \frac{z_i(t)}{2\Delta f},\ \hat{\tilde{s}}_i(t) = \frac{\tilde{s}_i(t)}{2\Delta f},\ \hat{x}_i(t) = \frac{x_i(t)}{2\Delta f},\ \hat{n}(t) = \frac{n(t)}{2\Delta f}. \tag{4.12}$$

Successful transmission requires that $z_i(t) = \tilde{s}_i(t) + x_i(t) + n(t)$ be higher than a specified threshold if the transmitted bit is a 1 and $z_i(t) = x_i(t) + n(t)$ be lower than that threshold if the transmitted bit is a 0.

4.3 Chebyshev Dispersion Coding Functions

4.3.1 Chebyshev Coding Selection

In addition to phase conjugation in user pairs, expressed in (4.1) and enforced in (4.4), DCMA requires dispersion code diversity to accommodate multiple user pairs. A set of appropriate functions should therefore be selected as dispersion codes. In multiple access technologies based on coherent detection schemes, such as for instance OFDMA or CDMA, the optimal coding functions form orthogonal sets, and corresponding MAI signals are ideally not affecting detection [85]. However, as pointed out in Sec. 4.1, DCMA is fundamentally based on non-coherent (threshold) detection. While being an advantage in terms of simplicity and cost, this fact makes orthogonal sets irrelevant in typical wireless channels, and other dispersion coding functions must therefore be identified.

In [101], we used Chebyshev polynomials of the first kind, $T_m(x)$, as the dispersion coding functions, because these polynomials all exhibit identical peak-to-peak amplitudes (-1 to $+1$) as x varies between -1 and $+1$ [120], leading to identical maximal MAI $[x_i(t)]$ time

spreads in all the receivers. These identical time spreads correspond to identical average MAI powers, as will be shown later in this section. Another reason for this choice is the fact that Chebyschev phasers have recently become available, in non-uniform transmission-line C-section technology [121]. Note that the dispersion codes used in optical multiple access are typically stair-case group delay functions [116–118]. However, these functions involve broad idle frequency guard bands between adjacent group delay stairs, due to the sinc-type frequency slicing by Bragg grating fibers, which represents a waste of spectral resources that is unaffordable at RF in addition to extra constraints on the phasers design. Also, the delay swing of the stair-case delay scales with the number of total users, leading to stronger inter-symbol interference if data rate is not reduced. Moreover, to achieve the best possible interference mitigation performance for the stair-case profile, synchronization between users are required, thus complicating the system design.

For a given group delay swing of $\Delta\tau = \tau_{\max} - \tau_{\min}$, the i^{th} Chebyschev dispersion coding function pair may by written as

$$\tau_{\text{TX}_i}(\omega) = \tau_0 + \frac{\Delta\tau}{2} T_{m_i}\left(\frac{\omega - \omega_0}{\Delta\omega/2}\right), \tag{4.13a}$$

$$\tau_{\text{RX}_i}(\omega) = \tau_0 - \frac{\Delta\tau}{2} T_{m_i}\left(\frac{\omega - \omega_0}{\Delta\omega/2}\right), \tag{4.13b}$$

where

$$T_{m_i}(x) = \cos(m_i \arccos x), \quad m_i \in \mathbb{Z} \text{ and } x \in [-1, 1],$$

is the m_i^{th} order Chebyshev polynomial of the first kind. Then, one may use the encoding set

$$\mathbf{C} = [m_1, \ldots, m_i, \ldots, m_N], \quad m_i \neq m_k, \tag{4.14}$$

whose elements may take any integer values with the only restriction that all these values appear only once. For convenience, we define $-T_{m_i}(x) = T_{-m_i}(x)$ $(m_i > 0)$ for the phase-conjugated functions. Figure 4.2 plots the first four Chebyshev group delay functions, corresponding to $\mathbf{C} = [1, 2, 3, 4]$.

4.3.2 Delay – Waveform Relationships

In order to better understand the relationships between the group delay function coding pairs (4.13) and the related DCMA waveforms, we shall now investigate a few important coding sets. We shall assume, for simplicity, the scenario where 1) $s_i(t) = \delta(t - t_{\text{Tx}_i})$, i.e. the

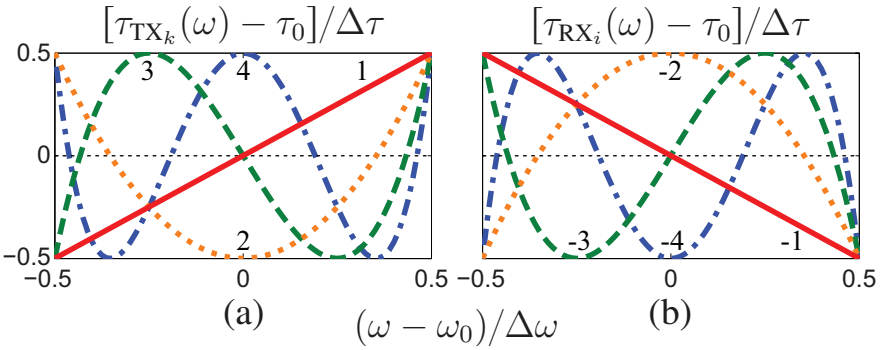

Figure 4.2 First few normalized Chebyshev dispersion function coding pairs, corresponding to $\mathbf{C} = [1, 2, 3, 4]$ with group delay swing $\Delta\tau$ and bandwidth Δf. (a) Encoding codes. (b) Corresponding (phase-conjugated) decoding codes (L. Zou, et al [16], TWC, © [2017] IEEE).

excitation signal energy is flat across the system bandwidth, 2) $t_{\mathrm{Tx}_i} = t_{\mathrm{Tx}_k} = 0$, $\forall\, i, k$, i.e. all the transmitters are synchronized, 3) $c_{ik}(t) = \delta(t)$, $\forall\, i, k$, i.e. all the channels are identical and shorted, and 4) $\sigma_{\mathrm{N}} = 0$, i.e. no noise is present. In this scenario, Eqs. (4.11) reduce to

$$\tilde{s}_i(t) = h_{ii}(t), \quad x_i(t) = \sum_{\substack{k=1 \\ k\neq i}}^{N} h_{ik}(t), \quad z_i(t) = \tilde{s}_i(t) + x_i(t). \tag{4.15}$$

Figure 4.3 plots the cascaded group delay pairs $\tau_{ik}(\omega)$ (first four columns), and the decoded waveform envelope $|\hat{z}_i(t)|$ and corresponding MAI envelope $|\hat{x}_i(t)|$ (last column). In the first four columns, the diagonal graphs ($k = i$) are matched cascaded group delays, $\tau_{ii}(\omega)$, which are constant over the entire system bandwidth. These group delays correspond to the desired signals $\tilde{s}_i(t) = h_{ii}(t)$ analytically given by (4.10a). The off-diagonal graphs ($k \neq i$) are unmatched cascaded group delays, $\tau_{ik}(\omega)$, corresponding to MAI, $h_{ik}(t)$ numerically computed by (4.10b). The corresponding group delay swing is

$$\Delta\tau_{ik} = \max\left[\tau_{ik}(\omega)\right] - \min\left[\tau_{ik}(\omega)\right] \leq 2\Delta\tau, \tag{4.16}$$

which is approximately equal to the spread of $h_{ik}(t)$.

Figure 4.3(a) corresponds to the coding set in Fig. 4.2, i.e. $\mathbf{C} = [1, 2, 3, 4]$, including thus mixed odd and even Chebyshev functions, while Figs. 4.3(b) and 4.3(c) correspond to the cases of all-odd and all-even Chebyshev functions, $\mathbf{C} = [1, -1, 3, -3]$ and $\mathbf{C} = [2, -2, 4, -4]$, respectively. An overall comparison of the corresponding signal waveforms (last column sets) reveals that the MAI peak level and hence the corresponding Bit Error Probability (BEP), is lowest for the all-odd set [Fig. 4.3(b)], intermediate for the mixed odd-even set [Fig. 4.3(a)]

and highest for the all-even set [Fig. 4.3(c)], as first noted in [101]. Moreover, one may observe a key difference of group delay profiles between the all-odd [Fig. 4.3(b)] and all-even [Fig. 4.3(c)] coding sets. The group delay profiles of the former are anti-symmetric (odd-symmetric) about the center frequency (ω_0), while those of the latter are symmetric (even-symmetric) about the center frequency. These symmetries are at the origin of the results, as shall be qualitatively explained later.

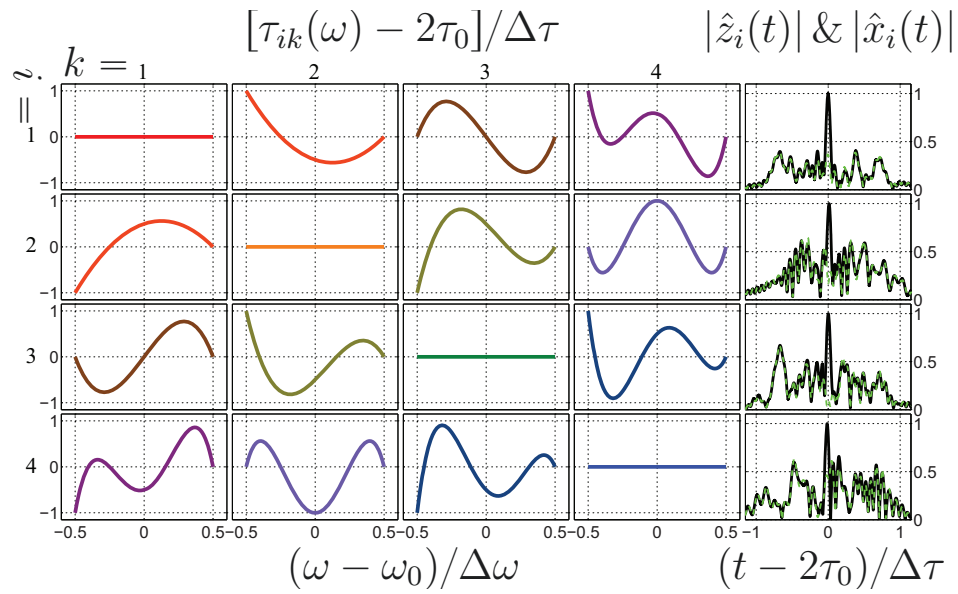

(a)

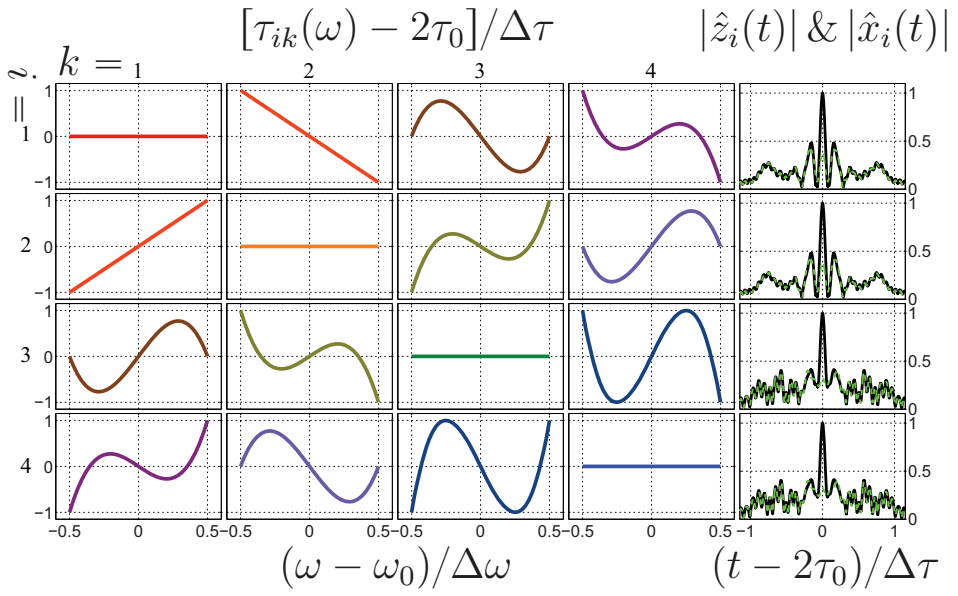

(b)

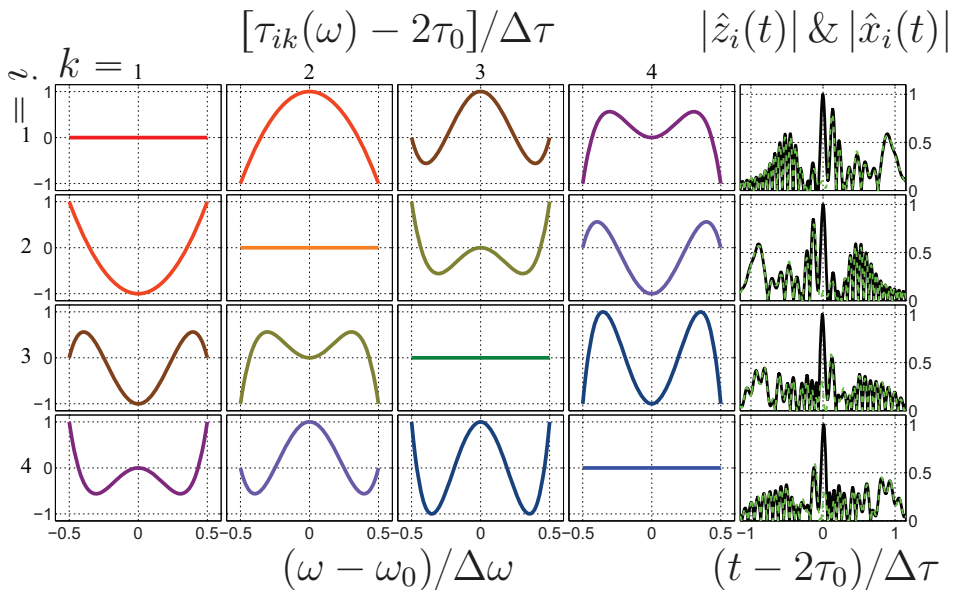

(c)

Figure 4.3 Normalized cascaded group delay functions, $\tau_{ik}(\omega)$ [Eq. (4.9) with (4.13)] (first four columns) and signal envelopes computed by (4.15) with (4.10) and (4.13), $\Delta\tau = 4$ ns and $\Delta f = 4$ GHz] (last column) with decoded signal evelope, $|\hat{z}_i(t)|$, in solid black lines and MAI, $|\hat{x}_i(t)|$, in dashed green lines. (a) Coding set corresponding to Fig. 4.2 (mixture of even and odd functions). (b) All-odd coding set, $\mathbf{C} = [1, -1, 3, -3]$ (odd functions). (c) All-even coding set : $\mathbf{C} = [2, -2, 4, -4]$ (even functions). It is seen that the MAI peak level is lowest in (b), intermediate in (a) and highest in (c) (L. Zou, et al [16], TWC, © [2017] IEEE).

Figure 4.4 provides graphical aids for qualitative study of the relationship between group delay profiles (including symmetry property) and the corresponding waveforms for the all-odd [Fig. 4.4(a)] and all-even [Fig. 4.4(b)] sets. In each case, the left column plots three cascaded group delay profiles $\tau_{ik}(\omega)$, selected out from Fig. 4.3, with a fixed i and all the k's that $k \neq i$. The right column plots the envelope waveform of the corresponding MAI contribution, $|h_{ik}(t)|$.

In general, it may be seen that group delay profile determines the distribution of the spectral contents (energy) of the signal in time. First, the group delay swing, $\Delta\tau_{ik}$, determines the time spread of $h_{ik}(t)$, which is widened by (sinc) ringing due to the chosen (rectangular) spectrum [Eq. (4.7b)]. Second, the group delay minima and maxima regions of $\tau_{ik}(\omega)$, highlighted by grey boxes in the figure, determine the peak level of $h_{ik}(t)$. This fact may be best explained by an example. Consider the $(i, k) = (1, 3)$ (middle) case in Fig. 4.4(a). Around the delay minima-maxima regions (left column), $\tau'_{ik}(\omega) \approx \delta\tau/\delta\omega$ is small, corresponding to relatively small $\delta\tau$ and large $\delta\omega$ ($\propto$ energy), and hence high energy concentration and high waveform amplitude in a short time span ($\delta\tau$). A particular case is the linear group delay (no minima-

maxima) [Fig. 4.4(a), $(i,k) = (1,2)$], which leads to uniform energy distribution and flat amplitude level over the entire time span. Another particular case is when there are multiple minima-maxima regions with the same delay [Fig. 4.4(b), $(i,k) = (1,3)$ and $(i,k) = (1,4)$], where the energies at different frequencies but identical delay times simply accumulate in the corresponding time span.

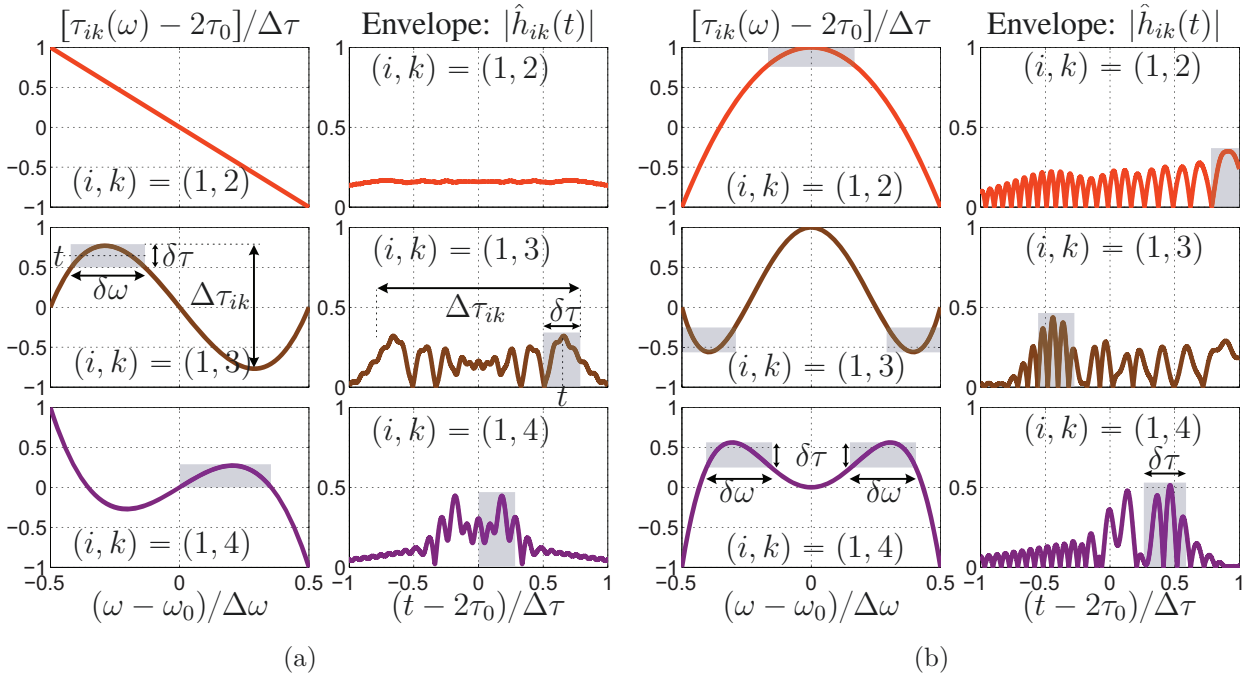

Figure 4.4 Graphical explanation of the relationships between the cascaded group delay sets $\tau_{ik}(\omega)$ [Eq. (4.9) with (4.13)] in Fig. 4.3 and MAI contribution, $|\hat{h}_{ik}(t)|$ (envelope) [inverse Fourier transform of Eq. (4.10b) with (4.7b) and (4.13)] using particular examples in Fig. 4.3. (a) $i = 1$, $k = 2,3,4$ in Fig. 4.3(b) (all-odd coding set). (b) $i = 1$, $k = 2,3,4$ in Fig. 4.3(c) (all-even coding set) (L. Zou, et al [16], TWC, © [2017] IEEE).

Note that, in practice, the transmitters are not synchronized and the channel delays are random, so that conditions 2) and 3) for the scenario leading to (4.15) do not hold, which results in the partial MAI, $h_{ik}(t)$, being randomly shifted in time. This random time shifting would incur the worst case scenario for the total MAI, $x_i(t)$, when the peaks of all the contributions $h_{ik}(t)$ occur at the same time and add up constructively. The best way to minimize such a worst-case MAI peak is to minimize the peak of each $h_{ik}(t)$, which is achieved when the cascaded group delay profiles are anti-symmetric [Fig. 4.4(a)] (odd-symmetric about the center frequency) and hence equalize the energy distribution in both halves of the time span, whereas symmetric group delay profiles [Fig. 4.4(b)] (even-symmetric about the center frequency) would instead tend to accumulate energy in half of the time span. This explains

why the all-odd coding set is superior to the all-even coding set in terms of minimizing MAI peak level. Therefore, we will only use the all-odd coding set in the system design. Mathematically, one easily verifies that even transfer magnitude (rectangular here) and even phase (corresponding to odd group delay) corresponds to an even transfer function, and hence an even impulse response by Fourier transformation, while even magnitude and odd phase (corresponding to even group delay) corresponds to impulse response that is neither even nor odd [120]. Appendix A mathematically proves the delay-waveform parity relationship.

4.3.3 Delay Swing – Bandwidth Product

Apart from the aforementioned MAI peak power (amplitude) due the energy concentration in time, the MAI average power is also of great concern since it is involved in the Signal-to-Interference Ratio (SIR). We shall show that the MAI average power is in fact linearly proportional to the group delay swing and bandwidth product. For this purpose, we use the Parseval theorem [120] to express the energy of $h_{ik}(t)$ as

$$E = \int_{-\infty}^{\infty} |h_{ik}(t)|^2 \, dt = \int_{-\infty}^{\infty} |H_{ik}(2\pi f)|^2 \, df, \tag{4.17}$$

where $H_{ik}(2\pi f) = H_{ik}(\omega)$ is the cascaded transfer function [Eq. (4.7b)]. Given the transfer magnitude (rectangular), Eq. (4.17) reduces to

$$\int_{-\infty}^{\infty} |h_{ik}(t)|^2 \, dt = 2 \int_{f_0 - \Delta f/2}^{f_0 + \Delta f/2} 1 \, df = 2\Delta f = E, \tag{4.18}$$

where the factor 2 includes the negative frequencies of $|H_{ik}(\omega)|$. The total MAI energy simply corresponds to $N-1$ identical contributions, i.e. $(N-1)E$. Then, assuming the total MAI spread $2\Delta\tau$, neglecting the (sinc) ringing due to the finite (rectangular) spectrum [1], the average power of $x_i(t)$ is found as

$$P_{\mathrm{X}} \approx \frac{(N-1)E}{2\Delta\tau} = \frac{(N-1)\Delta f}{\Delta\tau}, \tag{4.19}$$

1. In the ideal case of an all-pass phaser, i.e. $|H_{ik}(f)| = 1$, the impulse response of the desired signal is the Dirac function, corresponding to constant group delay, and the MAI has a time span of $2\Delta\tau$, corresponding to the cascaded TX and RX group delay swings. However, a practical phaser is rather band-pass, with rectangular amplitude spectrum and bandwidth Δf. Then the impulse response is a sinc function, with infinite time span, and the MAI also exhibits an infinite time span, with decay outwards from the all-pass interval of $2\Delta\tau$. However, it may easily be verified that the spill of the impulse responses over the $2\Delta\tau$ interval is negligible, due to the relatively high concentration of the sinc function corresponding to the relatively wide bandwidth spectrum. For the desired signal, for $\Delta f = 5$ GHz and $\Delta\tau =$ ns, the energy beyond the interval is approximately 0.01 dB, while for the MAI that energy is less than 0.2 dB.

which is identical for all receivers, i.e. independent of i. Then, SIR corresponds to the peak power of $h_{ii}(t)$ [Eq. (4.10a)], which is $P_{\mathrm{S}} = 4\Delta f^2$, divided by P_{X}, leading to

$$\mathrm{SIR} = \frac{P_{\mathrm{S}}}{P_{\mathrm{X}}} = \frac{4\Delta\tau\Delta f}{N-1}. \tag{4.20}$$

The term $\Delta\tau\Delta f$ is called Delay Swing-Bandwidth Product (DSBP), and Eq. (4.20) clearly states that the SIR is linearly proportional to DSBP. Note that the signal peak power (P_{S}) is proportional to Δf^2, the MAI average power (P_{X}) is proportional to $\Delta f/\Delta\tau$, increasing Δf increases both P_{S} and P_{X} with P_{S} increased faster, while increasing $\Delta\tau$ decreases only P_{X}, leading to the SIR globally linearly proportional to the DSBP.

4.3.4 Sensitivity to Group Delay Imperfections

Since the group delay functions are produced by analog components, phasers, whose actual responses may slightly deviate from the ideal specified ones, due to fabrication tolerance, circuit interconnection mismatching, etc., we shall study the sensitivity of the SIR of the signal and MAI to group delay imperfections. For this purpose, we will add a perturbation, $\upsilon_{ik}(\omega)$, to the cascaded TX_k-RX_i delay functions, $\tau_{ik}(\omega)$, and compare the resulting powers, P_{S} and P_{X} in the SIR [Eq. (4.20)] :

$$\tilde{\tau}_{ik}(\omega) = \tau_{ik}(\omega) + \upsilon_{ik}(\omega), \text{ with } \upsilon_{ik}(\omega) = \mathcal{N}(0, \sigma^2_{\tau_{ik}}), \tag{4.21}$$

where $\upsilon_{ik}(\omega)$ is assumed to follow a normal distribution with 0 mean and variance $\sigma^2_{\tau_{ik}}$. The group delay perturbation further expands the initial pair delay swings ($2\Delta\tau$) and hence the corresponding waveform time spans, which reduces the MAI power (P_{X}) according to (4.19). However, the deviation is typically much smaller than $2\Delta\tau$, and the reduction of P_{X} may be non-significant.

For a perfectly matched (ideal) delay, i.e. $\tau_{ii}(\omega) =$ constant, the desired signal energy concentrates in narrow time span that essentially corresponds to the main-lobe width ($2/\Delta f$) of the sinc function. The mismatch delay deviation ($\sigma_{\tau_{ii}}$) may be comparable to $1/\Delta f$, and may therefore significantly alter the signal power. Figures 4.5(a) and (b) show an illustrative example with random group delay variation. The delay variation is set within $[-1, +1]$ ns around the ideal matched one, leading to increased side-lobe in $[-1, +1]$ ns and decreased main-lobe power, respectively, as can be seen in Fig. 4.5(b). Figures 4.5(c) shows that the main-lobe power (P_{S}), and hence the SIR in (4.20) monotonically decreases as $\sigma_{\tau_{ii}}$ increases.

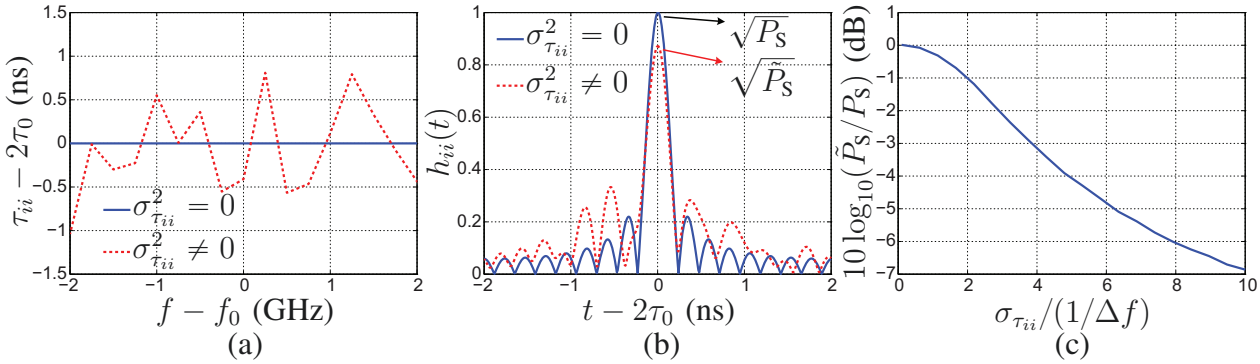

Figure 4.5 Delay mismatch in the (TX_i,RX_i) pairs [violation of (4.1)]. (a) Test (4 GHz bandwidth spectrum) group delay pair without [Eq. (4.1)] and with [Eq. (4.21)] mismatch. (b) Corresponding impulse responses envelopes. (c) Degradation of (maximal) power versus deviation from matching [$\sigma^2_{\tau_{ii}}$ in (4.21)] normalized by $1/\Delta f$ (half sinc main lobe width $\forall\, \Delta f$) (L. Zou, et al [16], TWC, © [2017] IEEE).

4.4 DCMA Proof-of-Concept System Implementation

This section presents a proof-of-concept 2×2 DCMA system implementation, based on first-order (odd) Chebyshev coding, and demonstrates a corresponding data communication experiment in a LOS channel. The system is designed to operate in the X-band, near which RF phaser technology has been best demonstrated so far, with the following specifications :

- Bit rate : 200 Mb/s/channel (limited by our data generator and could be higher for the chosen bandwidth), corresponding to bit period of 5 ns ;
- Center frequency : $f_0 = 10$ GHz (X-band center) ;
- Pulse bandwidth : $\Delta f = 4$ GHz from 8 to 12 GHz (X-band width), comparable to what is easily available in the millimeter-wave band, such as for instance 60 GHz.

The proposed prototype system architecture for the 2×2 DCMA is shown in Fig. 4.6. The digital data generator produces two streams of baseband data, which are modulated and narrowed into UWB RF pulse trains by the UWB pulse modulator and generator, respectively, in each of the two transmitters ($k = 1, 2$). The corresponding UWB RF pulses are then encoded by respective phasers, amplified, and radiated by the antennas to the air, where they mix together. The two resulting signals, received by the two RX antennas, are decoded by the phasers, whose outputs are power-detected and finally displayed on the oscilloscope. The digital data generator is the Anritsu MP1630B digital analyzer, which is capable of generating baseband data with bit rate up to 200 Mb/s. The oscilloscope is the Agilent DSO81204B digital oscilloscope, that captures RF signals with frequency up to 12 GHz. Since the system

frequencies ($8-12$ GHz) are below the oscilloscope maximum measurable frequency, in the experiment we eliminate the power detector and, instead, simply square the acquired digital data stream (numerical power detection). At higher system operating frequencies, towards the millimeter-wave regime, direct UWB analog-to-digital conversion (ADC) may become an expensive or even not off-the-shelf solution. One should therefore use a real power detector. Amplification may be required depending on the communication distance. The other parts of the system will be introduced in the following sections.

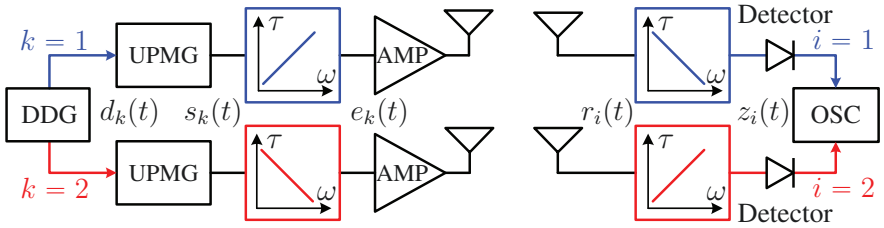

Figure 4.6 Proposed system architecture for the proof-of-concept 2×2 DCMA. "DDG", "UPMG", "AMP" and "OSC" stand for digital data generator, UWB pulse modulator and generator, power amplifier and oscilloscope, respectively (L. Zou, et al [16], TWC, © [2017] IEEE).

4.4.1 UWB Pulse Modulator and Generator (UPMG)

The UPMG in Fig. 4.6 performs two functions : baseband Differential On-Off Keying (DOOK) modulation and UWB RF Pulse Generation (PG), as schematically shown in Fig. 4.7.

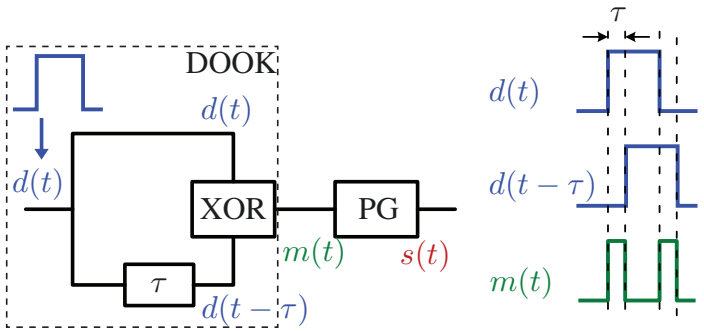

Figure 4.7 UWB pulse modulator and generator (UPMG) schematic with corresponding notations, where the part in the dash box in the baseband DOOK modulator and "PG" is the UWB RF pulse generator (L. Zou, et al [16], TWC, © [2017] IEEE).

Differential On-Off Keying (DOOK) Pulse Modulator

DOOK modulation is less used than non-differential On-Off Keying (OOK) modulation in practice. However, we adopt it here because the baseband data stream from the digital data generator is in the Non-Return-to-Zero (NRZ) format [122] and because the UWB RF pulse generator we use here is based on rising-edge triggering [4]. To properly trigger the pulse generator, OOK modulation would require to first transform NRZ into Return-to-Zero (RZ) [122] format, which requires iteratively detecting the level of the NRZ data every bit period, and hence requires a synchronized clocking circuit, whereas, DOOK modulation requires only detection of the rising and falling edges of the NRZ data, which may be easily done by using an XOR chip, as will be shown latter.

DOOK modulation produces mono-pulse when there is a change of state, i.e. rising or falling edge, occurring in the input data stream. This operation may be accomplished by an XOR chip. For detecting the change of state, the data stream $d(t)$ in Fig. 4.7 is divided into two paths, one of which is delay by τ. The two signals, namely $d(t)$ and $d(t-\tau)$ are compared by the XOR chip, which generates $m(t) = 1$ when the two inputs are different, and otherwise $m(t) = 0$. The width of the output mono-pulse $m(t)$ is equal to the delay, τ. Figure 4.8 shows the fabricated DOOK modulator corresponding to the dash-box part in Fig. 4.7.

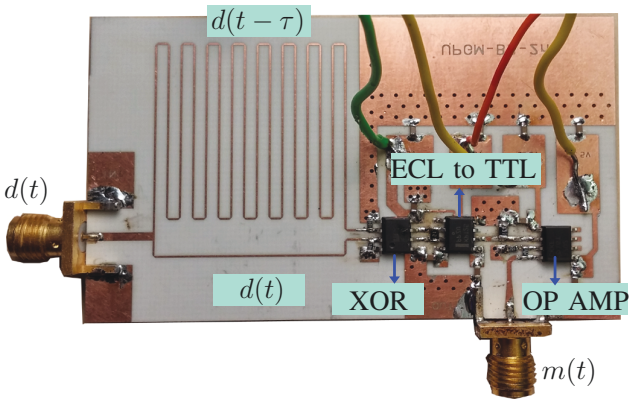

Figure 4.8 The fabricated baseband DOOK modulator corresponding to the dash-box part in Fig. 4.7, where "OP AMP" stands for operational amplifier, and the ECL-to-TTL converter and the OP AMP are used to control the voltage level of the output $m(t)$.

UWB RF Pulse Generator

Following the DOOK modulator is the UWB RF pulse generator ("PG"), based on a pair of step recovery diodes (SRDs), which further narrows down the pulse width of $m(t)$ to the

pico-second range. Part of this section is excerpt from the author's work, L. Zou, et al, [4], MWCL, ©2017 IEEE.

• *Principle*

The transient behaviour of a PN junction in response to a step voltage from the forward to the reverse bias regimes is shown in Fig. 4.9. Initially, the PN junction is forward biased with current i_{F}. When the voltage v_{i} changes polarity, the junction is not switched off immediately, but rather takes time τ_1 (storage phase), with current $i_{\mathrm{R,transient}}$, to neutralize the charges stored in the depletion region and progressively raise the junction barrier [123]. Note that during the whole storage phase, the junction maintains low resistance and almost constant junction voltage, i.e. $v_{\mathrm{j}} \approx V_{\mathrm{T}}$. Near the end of the storage phase, the raising junction barrier increases the resistance, finally switching off the junction for a decay time τ_2 (decay phase), which is extremely short (in the picosecond range) for an SRD [123]. Assuming constant i_{F} and sufficient forward biasing duration, τ_{F}, the charge stored in the forward biasing state is [123]

$$Q_{\mathrm{S}} = i_{\mathrm{F}}\tau_{\mathrm{L}}\left(1 - e^{-\tau_{\mathrm{F}}/\tau_{\mathrm{L}}}\right) \approx i_{\mathrm{F}}\tau_{\mathrm{L}}. \tag{4.22}$$

where τ_L is the minority carrier lifetime, which is intrinsic to the PN junction. The approximation in (4.22) holds when $\tau_{\mathrm{F}} > \tau_{\mathrm{L}}$, corresponding to static, i.e. time independent, Q_{S}. Now assuming constant $i_{\mathrm{R,transient}}$, the storage phase time is [123]

$$\frac{\tau_1}{\tau_{\mathrm{L}}} = \ln\left[1 + \frac{i_{\mathrm{F}}\left(1 - e^{-\tau_{\mathrm{F}}/\tau_{\mathrm{L}}}\right)}{i_{\mathrm{R,transient}}}\right] \approx \ln\left(1 + \frac{i_{\mathrm{F}}}{i_{\mathrm{R,transient}}}\right), \tag{4.23}$$

which indicates that τ_1 may be controlled by the ratio $(i_{\mathrm{F}}/i_{\mathrm{R,transient}})$ if $\tau_{\mathrm{F}} > \tau_{\mathrm{L}}$. We shall next present our pulse generator based on this SRD transient physics.

Figure 4.10 shows the schematic of the proposed SRD-pair pulse generator corresponding to the "PG" part in Fig. 4.7. The generator is triggered by the rising edge of the input voltage through PIN diode D1, that is always ON for blocking possible negative input voltages. Its core is the parallel connection of SRDs D2 and D3, biased at their cathode by DC $V_s < 0$ through R_1 current limiter, C_2 by-pass capacitor and RF choke L, with R_2 controlling the pulse width, as will be shown later. Finally, Schottky diode D4, operates as a pulse formation switch. The resistor $R_0 = 50\ \Omega$ ensures input matching during the pulse production, and the capacitor C_1 blocks DC input. The parasitic elements L_{p}, C_{p}, L_{g}, namely the SRD package inductance, capacitance, and grounding via inductance, respectively, are shown in dashed line, and will be discussed later.

Let the excitation v_1 be square-wave, the ADS circuit-simulated results are shown in Fig. 4.11.

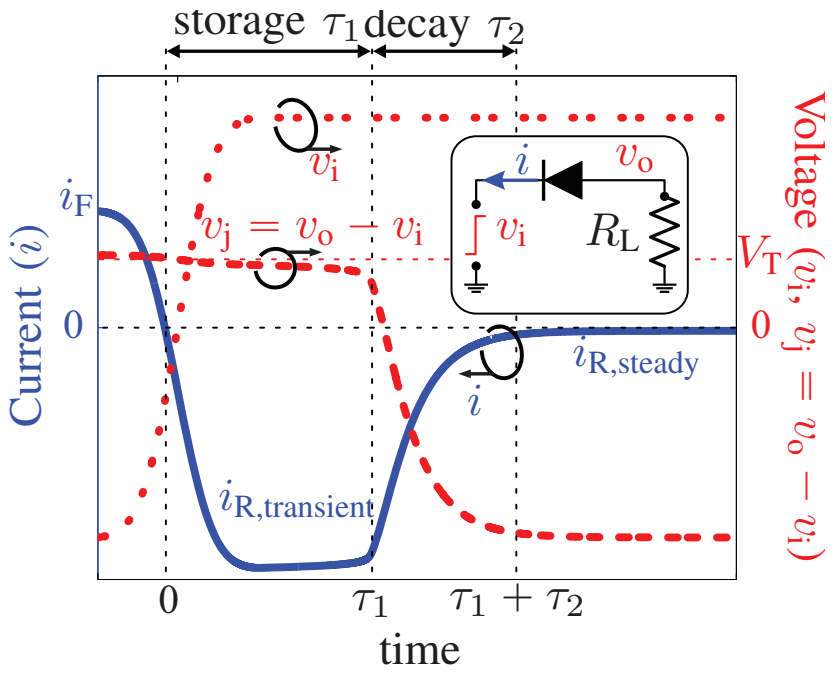

Figure 4.9 PN junction transient current i (solid blue) and junction voltage v_j (dash red) in response to a step voltage v_i (dot red) from the forward to the reverse bias regimes. (L. Zou, et al, [4], MWCL, © [2017] IEEE)

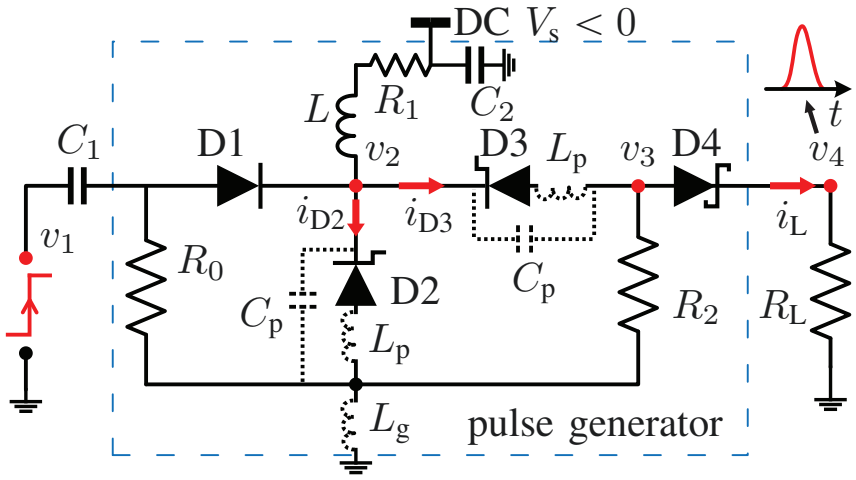

Figure 4.10 Proposed SRD-pair pulse generator. (L. Zou, et al, [4], MWCL, © [2017] IEEE)

According to the results, the circuit operation may be decomposed into five phases as described next.

• Phase 1 ($t < t_1$) : D2 and D3 are forward biased, and D4 is off. The excitation v_1 is close to 0 V, so the D2 and D3 forward currents are such that $i_{F,D2} \gg i_{F,D3}$ due to the existence of R_2 in the D3 loop. The junction voltages $v_{j,D2} = -v_2$ and $v_{j,D3} = v_3 - v_2$, where $v_3 < 0$

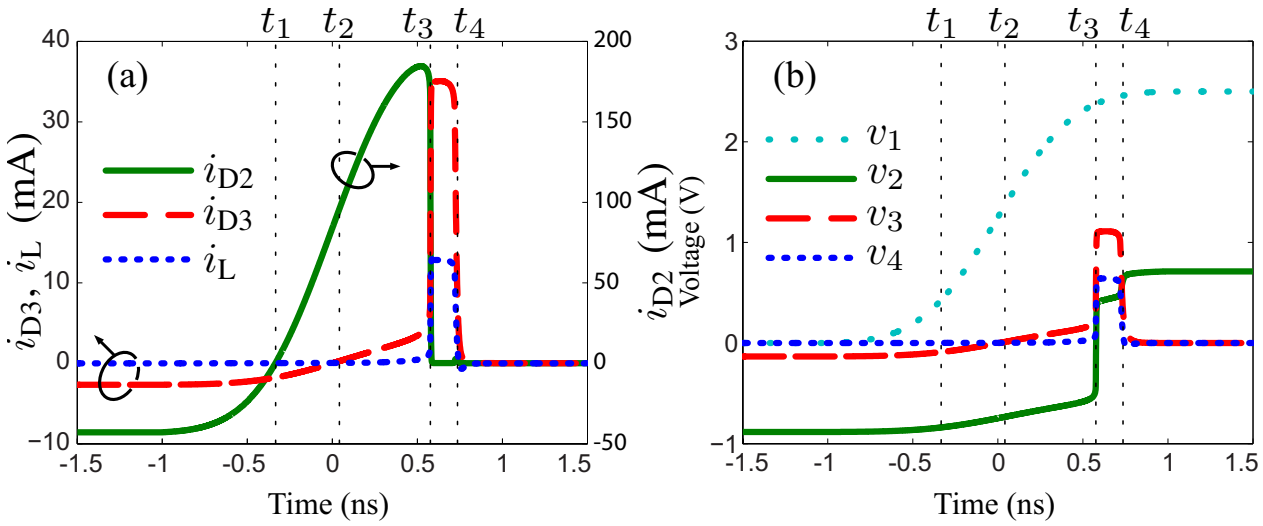

Figure 4.11 Circuit-simulated (a) currents (polarities referred to current directions indicated in Fig. 4.10), (b) voltages, with $V_s = -3.5$ V, $R_1 = 25\ \Omega$, $R_2 = 50\ \Omega$, $L_p = C_p = L_g = 0$ and spice models D1 : Avago HMPS-2822, D2 and D3 : Aeroflex MMDB30-0805, D4 : Skyworks SMS7630-061-0201. (L. Zou, et al, [4], MWCL, © [2017] IEEE)

due to the current flowing in R_2 from the ground to node 3, so that D4 is off and $v_4 = 0$.

• Phase 2 ($t_1 < t < t_2$) : D2 is in storage regime, D3 is still forward biased, and D4 is still off. The excitation v_1 starts rising, driving D2 ($i_{R,D2} > 0$) into storage regime before D3 due to the smaller resistance in the D2 current loop than that in the D3 one and hence faster current changing rate ($\partial i_{D2}/\partial t > \partial i_{D3}/\partial t$) in response to the rising edge of v_1. According to Fig. 4.9, $v_{j,D2} = -v_2$ varies only slightly in storage regime, and $v_3 < 0$ because D3 is still forward biased, and hence keeping D4 off.

• Phase 3 ($t_2 < t < t_3$) : D2 and D3 are both in storage regime, D4 is still off. The voltage v_1 eventually also drives D3 into storage regime ($i_{R,D3} > 0$). Since $i_{F,D2}/i_{R,D2} \ll i_{F,D3}/i_{R,D3}$, we have $\tau_{1,D2} < \tau_{1,D3}$ according to (4.23), and therefore D2 will switch off before D3. In the meanwhile, v_3 follows v_2, with insufficient variation to switch D4 on.

• Phase 4 ($t_3 < t < t_4$) : D2 is off, D3 is still in storage regime, D4 is on. The SRD D2 abruptly switches off at t_3, while D3 remains in storage regime. Consequently, v_2, and following v_3, abruptly increase, which switches D4 on, and therefore generates at the output the rising edge of v_4. Moreover, the off-switching of D2, and the on-switching of D4, which makes R_L parallel to R_2, together boost $i_{R,D3}$, starting to shorten the D3 storage time, which would otherwise be longer as expected in Phase 3.

• Phase 5 ($t > t_4$) : D2, D3, D4 are all off. The D3 storage phase suddenly ends at t_4,

nullifying $i_{\mathrm{R,D3}}$ and v_3, and hence switching D4 off, which results in the falling edge of v_4.

When the input level goes back to zero, the generator returns to the regime of Phase 1, waiting for the next voltage step to resume the aforementioned pulse formation cycle.

Let us now examine the factors determining the pulse width. Equation (4.23) assumes constant $i_{\mathrm{R,transient}}$ over the entire storage phase τ_1. As explained above, the storage phase for D3 is from t_2 to t_4. However, since $i_{\mathrm{R,D3}}(t_2 < t < t_3) \ll i_{\mathrm{R,D3}}(t_3 < t < t_4)$, the storage time essentially reduces to the interval $[t_3, t_4]$, and $i_{\mathrm{R,transient}}$ in (4.23) should be replaced by $i_{\mathrm{R,D3}}(t_3 < t < t_4)$ for the effective storage time of D3. Since this interval ($[t_3, t_4]$) corresponds to the pulse duration, this duration can be approximated as

$$T \approx \tau_L \ln\left[1 + \frac{i_{\mathrm{F,D3}}}{i_{\mathrm{R,D3}}(t_3 < t < t_4)}\right], \tag{4.24}$$

with an accuracy that is proportional to $i_{\mathrm{R,D3}}(t_2 < t < t_3)$ and hence inversely proportional to R_2, i.e. the closer $i_{\mathrm{R,D3}}$ to zero in $[t_2, t_3]$ (associated with larger R_2), the better the accuracy, as will be shown later in Fig. 4.12(a). Using Ohm law, one may further write (4.24) in the form

$$T \approx \tau_L \ln\left(1 + r\frac{R_2||R_{\mathrm{L}}}{R_2}\right) = \tau_L \ln\left(1 + r\frac{R_{\mathrm{L}}}{R_2 + R_{\mathrm{L}}}\right), \tag{4.25}$$

where r is the ratio of v_3 in the forward bias regime to v_3 in the $[t_3, t_4]$ interval. Equation (4.25) reveals that, for given R_{L}, one may adjust R_2 to control the pulse width. This is confirmed by the simulation results in Fig. 4.12(a), which also shows the result for the approximation in (4.25). Finally, Fig. 4.12(b) plots the pulse magnitude, which is seen to be essentially flat versus R_2 when $R_2 \geq R_{\mathrm{L}} = 50$ Ohm. Note that the curves in Fig. 4.12 are restricted to $R_2 > 50$ Ohm, which is the practically meaningful tunability range, since $\lim_{R_2 \to 0} v_3 = 0$ which maintains D4 off all the time (Fig. 4.10). The pulse repetition rate (PRR) is the same as the PRR of the trigger. The minimum triggering period, P_{min}, is naturally such that $P_{\mathrm{min}} > \tau_{\mathrm{F}} > \tau_{\mathrm{L}}$, according to (4.22) and (4.23). Hence, $\mathrm{PRR}_{\mathrm{max}} = 1/P_{\mathrm{min}} < 1/\tau_{\mathrm{L}}$, where we have here $\tau_{\mathrm{L}} \approx 3$ ns, i.e. $\mathrm{PRR}_{\mathrm{max}} < 333$ MHz. In the experiment, we will use a PPR of 100 MHz. The maximum pulse width here is 200 ps, corresponding to $R_2 = 50$ Ohm in Fig. 4.12(a), while the minimum achievable pulse width should correspond to the rising or falling time of the SRD, which is 30 ps here. Thanks to the pulse forming mechanism, i.e. transient state that releases a small amount of charges stored in the PN junction, we achieve narrower pulse width and higher PRR, but lower peak amplitude than conventional stub-based generators. Appendix B compares different UWB pulse generation technologies in Table B.1.

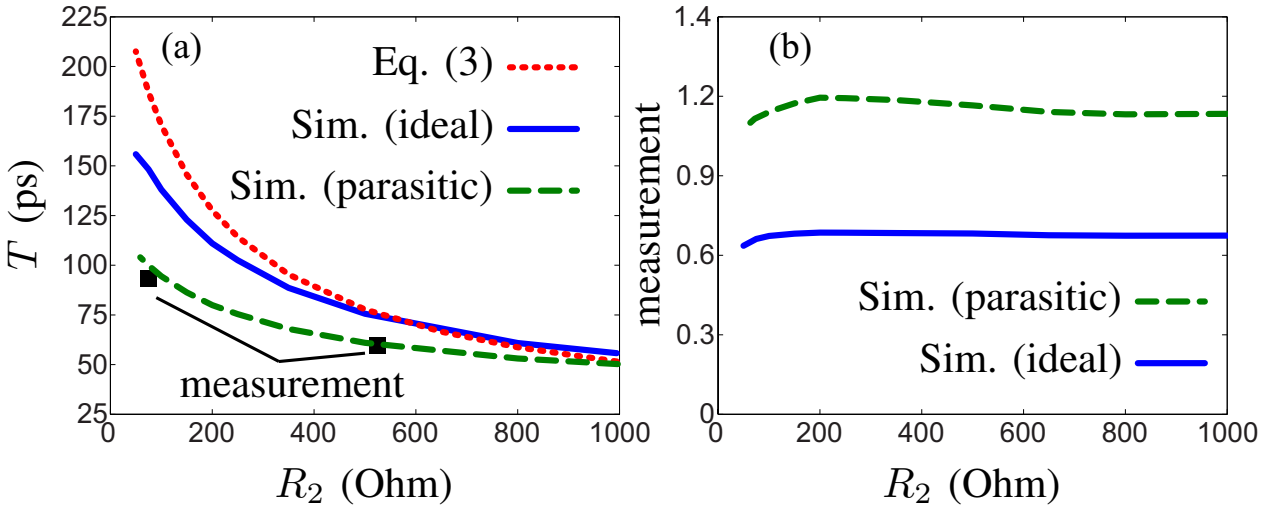

Figure 4.12 UWB pulse controlled by the resistor R_2 in Fig. 4.10. (a) Computed [Eq. (4.24) with simulated currents] and circuit-simulated pulse width versus R_2 for ideal and parasitic [finite transmission lines and $L_p = 0.4$ nH, $C_p = 0.06$ pF, $L_g = 73$ pH (Fig. 4.10)] cases, indicated with the measurement results for $R_2 = 50$, 560 Ω (two black squares) read from Fig. 4.14. (b) Simulated pulse magnitude versus R_2. (L. Zou, et al, [4], MWCL, © [2017] IEEE)

• *UWB Pulse Generator Experimental Demonstration*

Figure 4.13 shows the fabricated prototype, whose diode models are identical to those used for simulation in Fig. 4.11, and where R_1 consists of two 0805 51 Ω resistors in parallel, R_0 is a 0603 50 Ω resistor, and R_2 is a 0603 50 or 560 Ω resistor, L and C are high-impedance line (RF "choke") and by-pass capacitor, respectively, which, with the sectorial stubs, form a low-pass filter. The square wave trigger (0/2.5 V and PPR = 100 MHz, 50% duty cycle, $\tau_F = 5$ ns $> \tau_L = 3$ ns) was produced by the Anritsu MP1630B digital analyzer, the DC supply was $V_s = -3.5$ V, and the output waveforms were captured by the Agilent DSO81204B oscilloscope. The experimental results are shown in Fig. 4.14 (solid red). The half-magnitude pulse widths are 94 and 62 ps for $R_2 = 50$ Ω and 560 Ω, respectively, which are different from the corresponding simulation pulse widths in Fig. 4.12(a). Ringing tails are also observed. To understand the cause of the pulse width discrepancy between simulation and experiment and the experimental ringing tails, one should note that the transmission line lengths are assumed to be zero in Fig. 4.10 and in the corresponding simulation results in Fig. 4.11 and Fig. 4.12. However, in the fabricated prototype, nonzero-length transmission lines delay the multiple internal reflections between diodes, which are not perfectly matched, hence generating successive replicas of the intended output pulse corresponding to the ringing

tail. Moreover, the spurious pulses may constructively or destructively interfere with the main one, resulting in wider or shorter pulse width compared to the simulated on in Fig. 4.12(a). Finally, the parasitic elements in Fig. 4.10 also contribute to waveform distortion. One may identify the causes of distortion by including finite-length transmission lines and parasitic elements in the simulation, as shown by the dash-blue curves in Fig. 4.14. Among the parasitic elements, we identify the inductance in series with D2, i.e. L_{p} and L_{g}, as the critical parasitic elements, which lead to high-amplitude spikes due to the inductor transient response to a rapid current change [124].

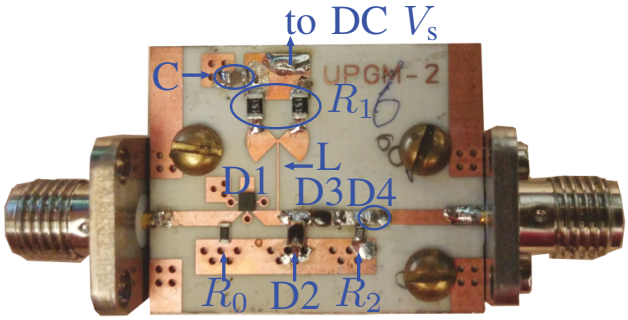

Figure 4.13 Experimental prototype on RO4003 (20 mil) substrate. (L. Zou, et al, [4], MWCL, © [2017] IEEE)

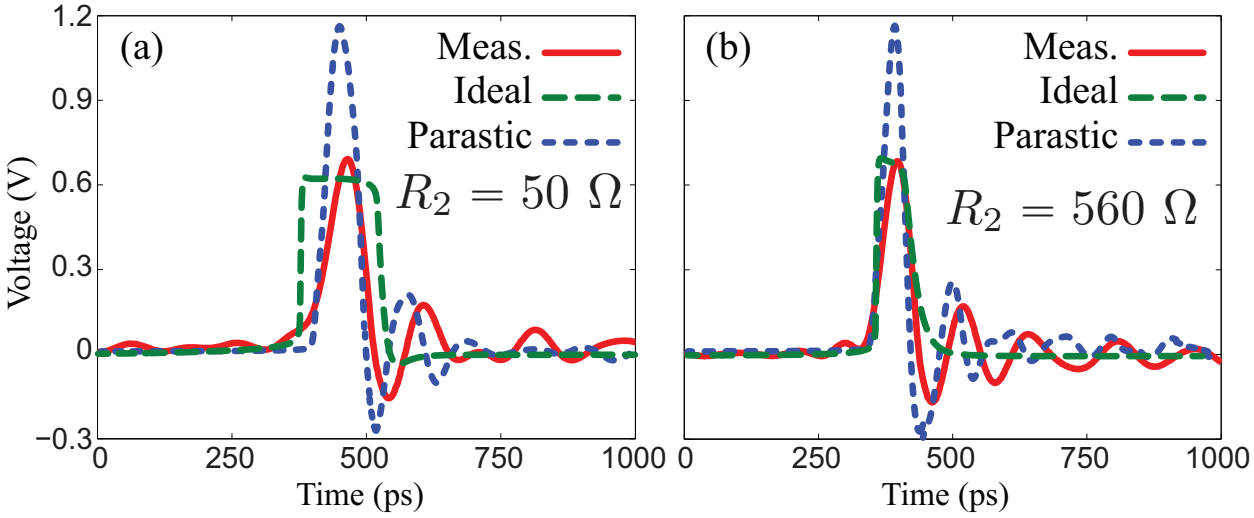

Figure 4.14 Results for measurement and simulations of ideal and parasitic (transmission lines and $L_{\mathrm{p}} = 0.4$ nH, $C_{\mathrm{p}} = 0.06$ pF, $L_{\mathrm{g}} = 73$ pH) cases. (a) $R_2 = 50\ \Omega$ and (b) $R_2 = 560\ \Omega$. (L. Zou, et al, [4], MWCL, © [2017] IEEE)

Figure 4.15 shows the temperature behavior of the generator. It is observed that pulse width

increases with increased temperature. Moreover, pulse widening also corresponds to reduced ringing, consistently with our interference explanation of the relation between the pulse width and ringing effect.

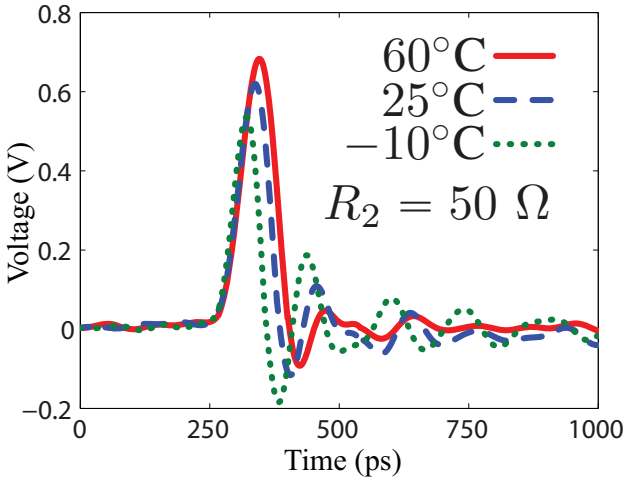

Figure 4.15 Measured output pulses at different temperatures (L. Zou, et al, [4], MWCL, © [2017] IEEE).

Note that the output from the pulse generator is mono-pulse, which still contains a DC component and cannot be radiated efficiently. To remove the DC component in the output of the D4 in Fig. 4.13, a short-end stub following D4 is used, which is not shown here, to transform the mono-pulse into mono-cycle [2].

UPMG Experimental Results

Figure 4.16 shows the measured input data stream, $d(t)$, DOOK modulated pulses, $m(t)$ in response to the rising or falling edges of $d(t)$, and the UWB RF pulses, $s(t)$, respectively, corresponding to the notations in Fig. 4.7. Here, the bit duration of $d(t)$ is 5 ns corresponding to bit rate 200 Mb/s, which is constraint here by the instrument (DDG – Anritsu MP1630B – in Fig. 4.6). The duration of $m(t)$, generated by the DOOK modulator, is 3 ns equal to the delay difference (τ) between the two path in Fig. 4.7. Finally $m(t)$ triggers the UWB RF pulse generator at its rising edges, yielding ultra-short RF pulses, $s(t)$.

Figure 4.17(a) shows a zoom on a single RF pulse of $s(t)$ with its envelop, and Fig. 4.17(b) shows its spectrum amplitude $|S(f)|$. The pulse waveform is not perfectly mono-cycle due to ringing [4]. We may use a bandpass filter, not shown in Fig. 4.7, to keep only the desired portion ($8 - 12$ GHz) of the spectrum so as to meet the system design specification. Within this bandwidth, the spectrum power density variation is found to be smaller than 2 dB.

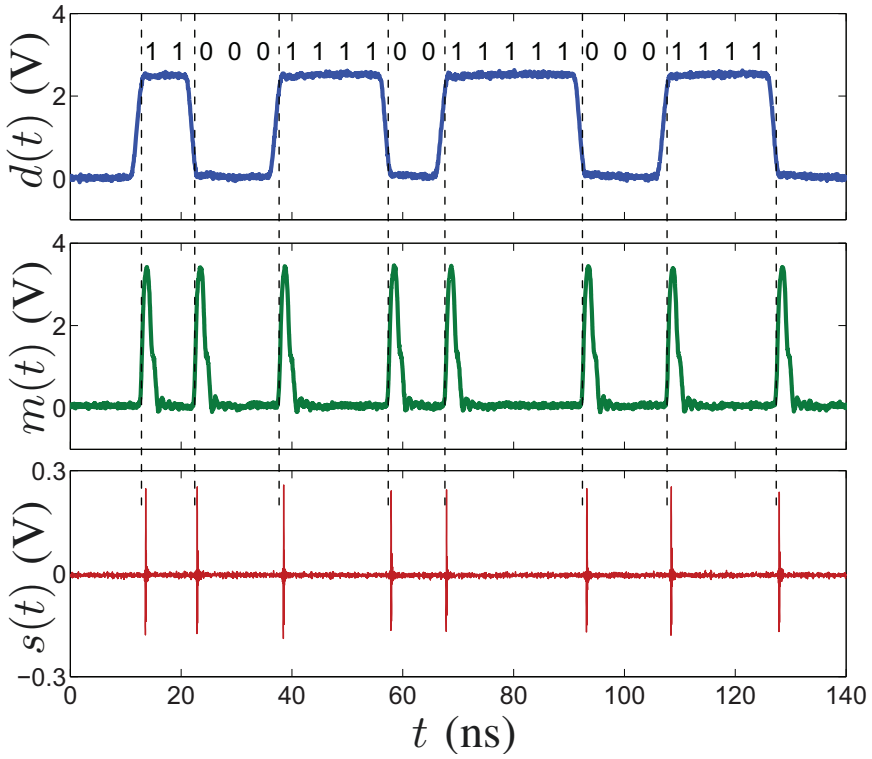

Figure 4.16 Waveforms at the corresponding nodes of the UPMG in Fig. 4.7. $d(t)$: input of the UPMG, generated by the DDG (Anritsu MP1630B) in Fig. 4.6. $m(t)$: baseband pulses produced by the DOOK modulator in response to the rising and falling edges of $d(t)$. $s(t)$: ultra-short RF pulses generated by the UWB pulse generator (L. Zou, et al [16], TWC, © [2017] IEEE).

4.4.2 LOS Wireless Channel

In the proof-of-concept system to be detailed next, we select a Vivaldi antenna for its wide bandwidth, high directivity and low dispersion [125–127]. This antenna is practically well suited for directive LOS UWB applications. The Vivaldi antennas implemented here exhibit return loss higher than 10 dB and broadside gain higher than 8 dB over the bandwidth.

From the system point of view, the relevant channel response includes the antenna responses. For the LOS experiment to be performed here, four identical antennas are configured as shown in Fig. 4.18. Two TX and two RX antennas are placed side by side with separation of 40 mm, which is larger than one wavelength of the lowest frequency, 8 GHz. The TX and RX antenna pairs are placed face to face, with distance d_{ii} being approximately 1 m, which satisfies the far-field condition. In this configuration, the $d_{ik} = \sqrt{d_{ii}^2 + s^2} = 1,001$ mm $\approx d_{ii} = 1,000$ mm, and the difference between communication distances d_{ik} and d_{ii} is only about 1 mm, corresponding to 3 ps delay difference. The corresponding reception angle difference is of only 2.3°, and the

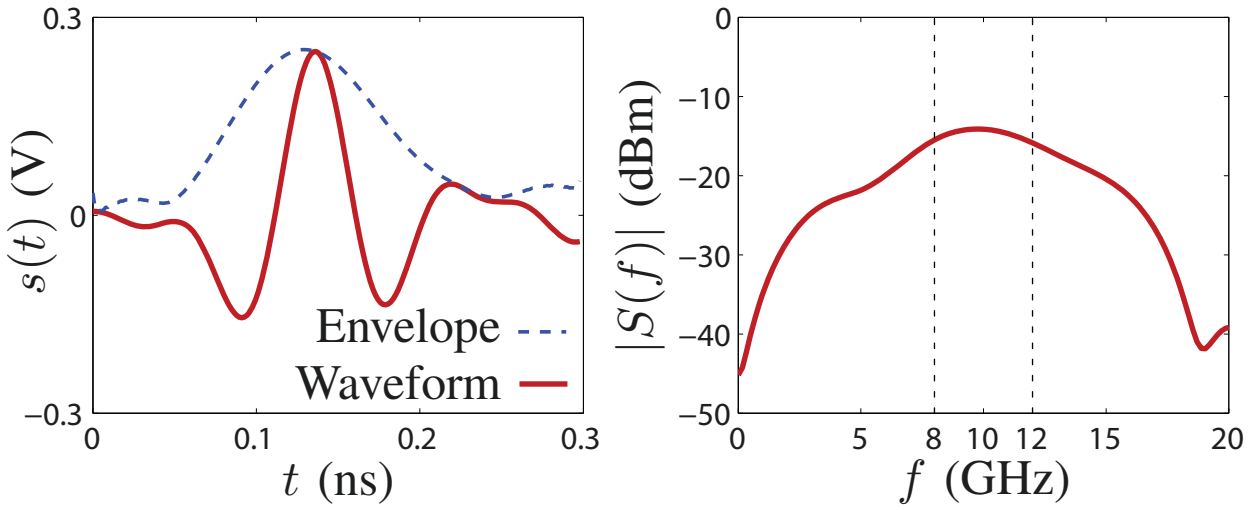

Figure 4.17 Single UWB RF pulse. (a) Zoom on a single pulse, with its Gaussian-like envelop. (b) Spectrum of a single pulse, with the DC component being essentially removed ($|S(0)| < -45$ dB) (L. Zou, et al [16], TWC, © [2017] IEEE).

antenna gains may hence be assumed identical for all the communication links. Therefore, if two transmitters are sending signals at same time (synchronized) and same level, each receiver will receive the signal and the interference at the same time with indistinguishable magnitude before any further processing.

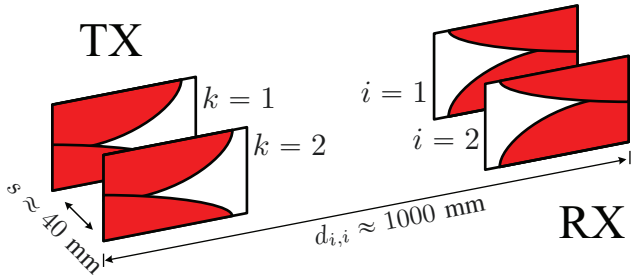

Figure 4.18 Vivaldi antenna setup for the measurement of the wireless channel responses (L. Zou, et al [16], TWC, © [2017] IEEE).

The LOS channel may be described by the transfer function $C_{ik}(\omega) = |C_{ik}(\omega)|\angle C_{ik}(\omega)$. For the LOS channel considered here, the magnitude response, $|C_{ik}(\omega)|$, includes free-space attenuation and antenna gain, as given by the Friis formula [85]. The former is inversely proportional to frequency, while the latter is proportional to frequency for a fixed antenna aperture, and hence the combination of the two yields a weakly frequency-dependent response. Moreover, the channel delay, $t_{ik}(\omega) = -\partial\angle C_{ik}/\partial\omega$, includes free-space delay, which

is naturally non-dispersive, and antenna delay, which is weakly dispersive for Vivaldi antennas [126, 127]. Figure 4.19 plots the measured channel magnitudes and delays, which are indeed essentially flat, indicating that both channel magnitudes and delays may be considered as weakly or negligibly frequency-dependent. Moreover, note that magnitudes and delays for the different channels are almost identical, due to the configuration described in the previous paragraph. Therefore, the impulse responses of the four channels may be uniquely written as $c_{ik}(t) = \delta(t), \forall\, i, k$.

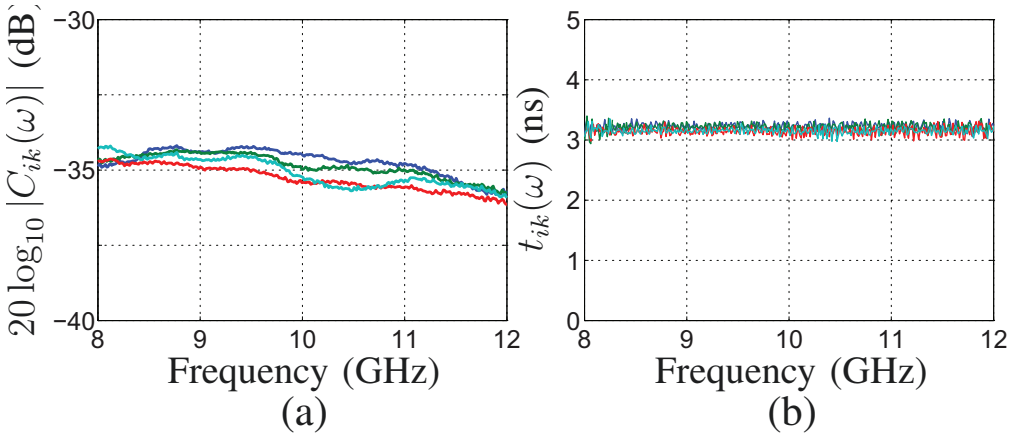

Figure 4.19 Measured channel, corresponding to the configuration in Fig. 4.18, using a vector network analyzer. (a) Channel magnitudes, $|C_{ik}(\omega)|$, found to be approximately -35 dB with variation smaller 2 dB. b) Channel delays, $t_{ik}(\omega)$, found to be approximately 3.2 ns (L. Zou, et al [16], TWC, © [2017] IEEE).

4.4.3 Chebyshev Coding Phasers

As mentioned in Sec. 4.3, we choose first-order (odd) Chebyshev coding, corresponding to the coding set $\mathbf{C} = [1, -1]$, and set the group delay swing $\Delta\tau = 1$ ns. This group delay swing yields SIR = 16 or 12 dB according to (4.20). The corresponding phasers are implemented in multilayered broadside-coupled stripline C-section technology [128] using a Low-Temperature Cofired-Ceramic (LTCC) fabrication process for high fabrication accuracy. Figure 4.20(a) shows the fabricated phaser, and Figs. 4.20(b) and (c) plot the measured results for the $+1$ and -1 order phasers. The matched pair delay (not shown here) has $\sigma_{\tau_{ii}} = 0.3$ ns $(1.2/\Delta f)$, corresponding to a signal power (SIR) degradation of 0.7 dB compared to the perfectly matched pair according to Fig. 4.5(c).

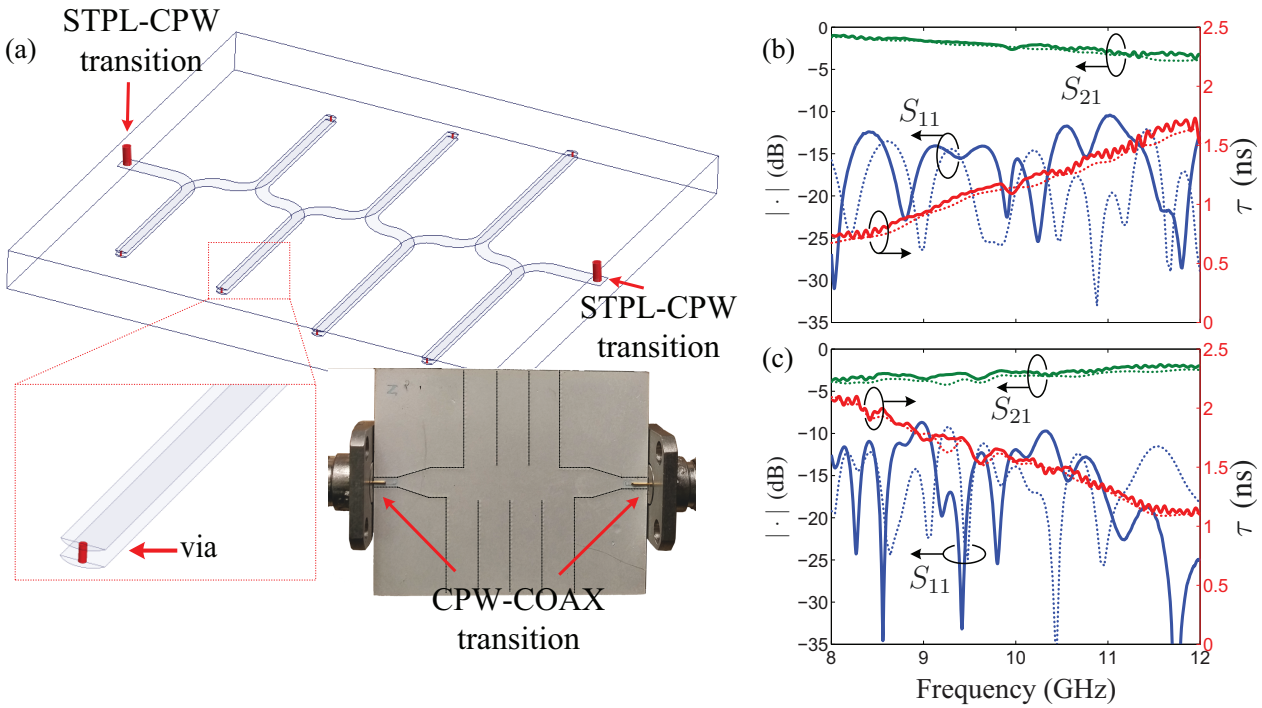

Figure 4.20 Broadside-coupled stripline C-section LTCC phaser. (a) Internal structure (simulation layout) and global photograph, including stripline-CPW-coaxial (STPL-CPW-COAX) transitions and inner shorting vias connecting coupled lines. (b) Measured (solid) and simulated (dotted) group delay (τ) and amplitude responses ($|S_{11}|$ and $|S_{21}|$) for the $+1^{\text{th}}$ order phaser. (c) Idem for the -1^{th} order phaser (L. Zou, et al [16], TWC, © [2017] IEEE).

4.5 DCMA Proof-of-Concept System Experimental Demonstration

The experimental proof-of-concept system corresponding to the proposed architecture in Fig. 4.6 is shown in Fig. 4.21. As already mentioned, the power detectors in Fig. 4.6 are not included in the system since power detection is to be done by taking square of the envelope of the waveform data captured by the oscilloscope. The bit period, which is the reverse of the bit rate, $T_{\text{b}} = 1/R_{\text{b}}$, should be larger than the MAI spread, which here is $2\Delta\tau = 2$ ns, to avoid intersymbol interference. Therefore, the theoretical maximal bit rate here would ideally approach 500 Mb/s/channel given the 2 ns MAI spread. Here we restrict the bit rate to 200 Mb/s/channel which corresponds to the maximal rate of the instrumentation.

Figure 4.22 shows the system experimental results (waveforms) at different nodes in Fig. 4.6. Figure 4.22(a) is the data stream, $d_k(t)$, from the digital data generator. The modulated UWB RF pulses, $s_k(t)$, corresponding to the rising and falling edges of $d_k(t)$ based on DOOK modulation, have been shown in Fig. 4.7. Figure 4.22(b) plots the signals, $e_k(t)$, encoded by

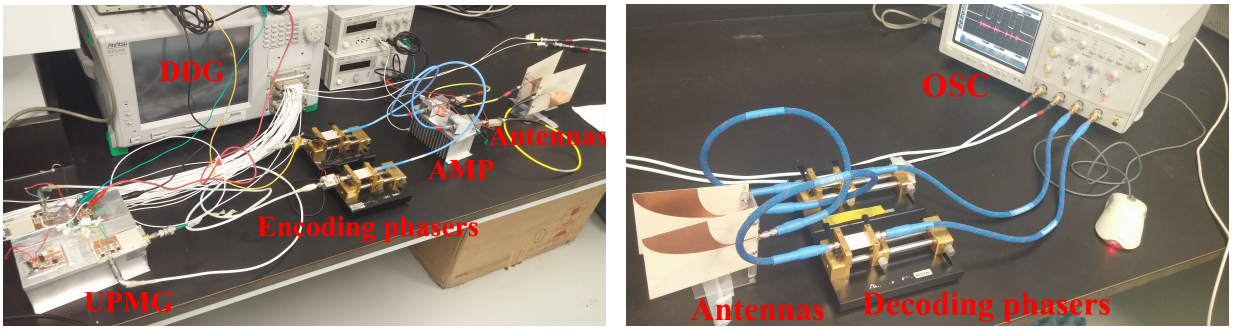

(a) (b)

Figure 4.21 Experimental prototype 2×2 DCMA system corresponding to the architecture in Fig. 4.6. (a) Transmitters. (b) Receivers (L. Zou, et al [16], TWC, © [2017] IEEE).

the respective encoding phasers, which are dispersed versions of $s_k(t)$. Figure 4.22(c) shows the received signal intensities, which correspond to the envelope squares, $|r_i(t)|^2$, and include the MAI from the undesired TX. The MAI peaks are circled out, and found to be roughly at the same level as the desired signals, and hence indistinguishable, at this stage. Note that the squared envelopes of $r_i(t)$ ($|r_i(t)|^2$) here do not correspond to the actual operation of the system at the corresponding nodes in Fig. 4.6; we numerically perform this operation for comparison with the decoded and power detected outputs, $|z_i(t)|^2$, as will be shown in Fig. 4.22(d). Figure 4.22(d) plots the intensity of the signals, $z_i(t)$ [$|z_i(t)|^2$] decoded by the respective decoding phasers. The MAI levels are dramatically reduced compared to those in Fig. 4.22(c), hence allowing to correctly detect the desired information signal. Finally, one may use integration [2] to recover the baseband data stream, $\tilde{d}_i(t)$, not physically performed in the experiment but shown in the black dashed lines in Fig. 4.22(d). The power ratio of the signal peak to the MAI Peak-Envelope-Power (PEP) ranges from 5 to 6. One may find the MAI average power from the PEP and then further obtain the SIR. Ideally, the MAI is a flat-amplitude curve due to the linear group delay, according to the analysis in Sec. 4.3. The MAI average power is typically half of its PEP, and the SIR should then be twice of the power ratio of the signal peak to the MAI PEP, which is about 10 to 12, in reasonable agreement with the value SIR = 16 obtained by (4.20), given the various non-idealities involved in the experiment.

2. This baseband data recovery may be performed digitally as follows : 1) apply threshold detection to the data in Fig. 4.22(d), which results in keeping the pulses, corresponding to rising/falling edges of the baseband signals and suppressing the MAI; 2) keep the polarity of the odd pulses, corresponding to rising edges, unchanged, and reverse the polarity of the even pulses, corresponding to falling edges; 3) integrate the bi-polar pulses in step 2), where positive and negative polarity pulses yield rising and falling edges, respectively, while the nulls between the positive and negative polarity pulses yield constant high level ("1") and low level ("0"), respectively.

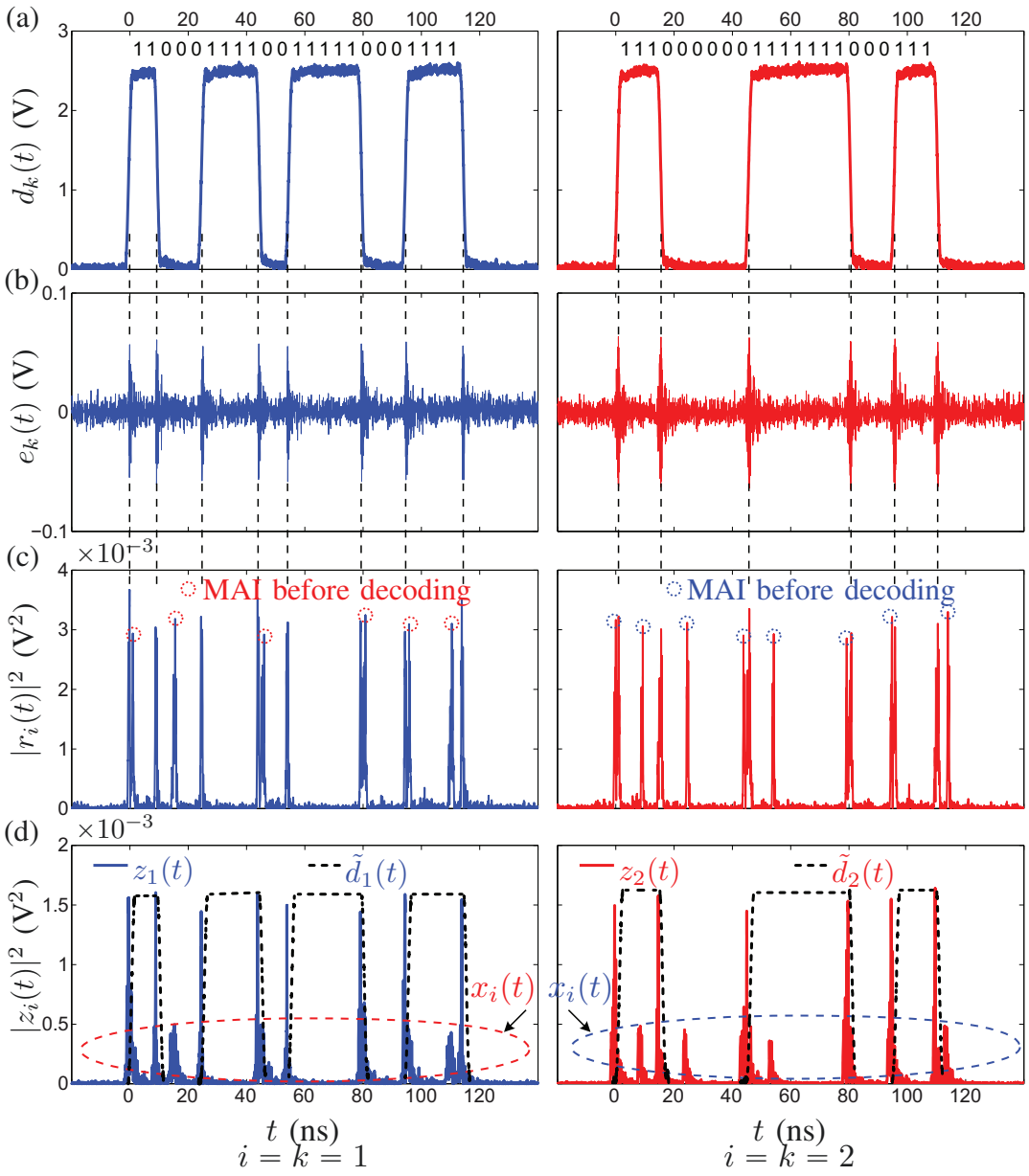

Figure 4.22 Measured waveforms for the system in Fig. 4.21 at the positions of the nodes indicated in Fig. 4.6. (a) Baseband data stream, $d_k(t)$. (b) Encoded waveforms, $e_k(t)$. (c) Received waveform intensity, $|r_i(t)|^2$. (d) Decoded waveform intensity, $|z_i(t)|^2$, and recovered baseband data, $\tilde{d}_i(t)$ by integration of $z_i(t)$ (L. Zou, et al [16], TWC, © [2017] IEEE).

It is also worth mentioning that the time synchronization is simply based on burst triggering the receiver in response to the pulse sent by the transmitter, since different users are discriminated by different power levels. This mechanism is naturally more immune to delay offset in synchronization than that in of the time-hopping technique, where different users are allocated different time slots (chips) for multiple access based on pulse position

modulation [115].

4.6 Summary and Perspective

This chapter proposed the dispersion code multiple access (DCMA) concept as an cost-efficient, energy-efficient and low-latency solution for future high-speed wireless communications. The key to multiple access is proper choice of dispersion code set. The common stair-case delay profiles, with large idle spectrums, used for multiple access in optics can not be directly transplanted to microwave regime where spectrum resources are precious. Therefore we proposed to adopt Chebyshev polynomials as the dispersion code set for their equal group delay swing and hence identical contribution to the MAI power. Then, we experimentally demonstrated the world's first proof-of-concept real-time radio system for wireless data transmission, showing the feasibility of DCMA. Then, we will later characterize the system in terms of bit error probability, which involves variation of a lot of parameters, such as for instance bit rate, bandwidth, user number, signal and interference energy level, wireless channel, etc. Therefore, experimental characterization will be extremely difficult and costly, and Chapter 5 characterizes the DCMA system numerically.

CHAPTER 5 CHARACTERIZATION OF DISPERSION CODE MULTIPLE ACCESS (DCMA) COMMUNICATION SYSTEM

The previous chapter experimentally demonstrated a proof-of-concept 2×2 DCMA system with identical LOS channels $[c_{ik}(t) = \delta(t), \forall i, k]$ and without any specific noise study. This chapter will characterize the performance of a general DCMA system comprised of $N \times N$ TX-RX user pairs, in terms of multiple access interference (MAI), signal to interference ratio (SIR), and bit error probability (BEP). First, Sec. 5.1 characterizes for line-of-sight (LOS) channel, then, Sec. 5.2 for non-line-of-sight (NLOS) channel.

The characterization will be performed analytically and numerically, as it would be excessively involved to perform experimentally, but it will provide the key results relevant to the design of future complex DCMA systems. For simplicity, we shall assume that the environment is time-invariant (static).

Part of this chapter is excerpt from the author's works, [16], and [18], available at URL : `https://arxiv.org/abs/1709.08085`.

5.1 LOS Channel Characterization

5.1.1 Channel Description

The LOS channel impulse response may be found by taking the inverse Fourier transform of the transfer function, $C_{ik}(\omega)$, which implicitly accounts for the antennas and may be obtained by measurement, as in Sec. 4.4.2, or by analytical formulas. For the case of a free-space LOS channel, the application of Friis formula with added delay leads to [85]

$$\begin{aligned} C_{ik}(\omega) &= \frac{\lambda\sqrt{G_{\mathrm{TX}_k}(\omega)G_{\mathrm{RX}_i}(\omega)}}{4\pi d_{ik}} e^{-j\omega t_{ik}} e^{-j\int_{-\infty}^{\omega} t'_{ik}(\omega')\,d\omega'} \\ &= \frac{\sqrt{G_{\mathrm{TX}_k}(\omega)G_{\mathrm{RX}_i}(\omega)}}{2\omega t_{ik}} e^{-j\omega t_{ik}} e^{-j\int_{-\infty}^{\omega} t'_{ik}(\omega')\,d\omega'}, \end{aligned} \tag{5.1}$$

where $G_{\mathrm{TX}_k}(\omega)$ and $G_{\mathrm{RX}_i}(\omega)$ are the power gain functions in the TX_k and RX_i directions, respectively, $t_{ik} = d_{ik}/c$ is the free-space (non-dispersive) delay, c is the speed of light, and $t'_{ik}(\omega)$ is the channel dispersive delay induced by the antennas. As illustrated in Fig. 4.19 and discussed in Sec. 4.4.2, in a practical UWB pulse (as opposed to narrow multi-band) system with UWB low-dispersion antennas, such as for instance Vivaldi antennas, the channel response is essentially frequency independent in both delay, i.e. $\partial t'_{ik}/\partial\omega \approx 0$, and in magnitude,

i.e. $|C_{ik}(\omega)| \approx \sqrt{G_{\mathrm{TX}_k}(\omega_0)G_{\mathrm{RX}_i}(\omega_0)}/(2\omega_0 t_{ik})$, where ω_0 is the center frequency. Therefore, denoting the product of the TX_k and RX_i antenna power gains $G_{ik} = G_{\mathrm{TX}_k}(\omega_0)G_{\mathrm{RX}_i}(\omega_0)$ and shifting the reference time to $t'_{ik}(\omega) = 0$, Eq. (5.1) reduces to the expression

$$C_{ik}(\omega) = \frac{\sqrt{G_{ik}}}{2\omega_0 t_{ik}} e^{-j\omega t_{ik}}, \tag{5.2}$$

whose impulse response is

$$c_{ik}(t) = \frac{\sqrt{G_{ik}}}{2\omega_0 t_{ik}} \delta(t - t_{ik}) = a_{ik}\delta(t - t_{ik}). \tag{5.3}$$

Since the transmission throughput is ultimately determined by SIR, which includes the ratio a_{ii}/a_{ik}, we further normalize (5.3) as

$$c'_{ik}(t) = \frac{a_{ik}}{a_{ii}}\delta(t - t_{ik}) = \frac{\sqrt{G_{ik}/G_{ii}}}{t_{ik}/t_{ii}}\delta(t - t_{ik}), \tag{5.4a}$$

$$c'_{ii}(t) = \delta(t - t_{ii}). \tag{5.4b}$$

5.1.2 MAI Analysis

In order to fully characterize the system in the $c_{ik}(t)$ channel described by (5.4), we shall first determine its MAI in that channel. For simplicity, we idealize the information signal to a train of OOK-modulated Dirac pulses with bit period $T_\mathrm{b} = 2\Delta\tau$, corresponding to the maximal dispersed duration, i.e.

$$s_k(t) = \sum_{\ell=1}^{\infty} d_{k,\ell}\delta(t - \ell T_\mathrm{b} - t_{\mathrm{TX}_k}), \qquad k \in \{1, \ldots, i, \ldots, N\}, \tag{5.5}$$

where $d_{k,\ell} = 1$ or 0 is the ℓ^{th} bit from TX_k, and t_{TX_k} is a random transmitting delay offset taking account for the transmitter asynchronization. Inserting (5.4b) and (5.4a) into (4.11b) and (4.11c), respectively, with (5.5), yields

$$\tilde{s}_i(t) = \sum_{\ell=1}^{\infty} d_{i,\ell}\alpha_{ii}h_{ii}(t - \ell T_\mathrm{b} - t_{\mathrm{TX}_i} - t_{ii}), \tag{5.6a}$$

$$x_i(t) = \sum_{\ell=1}^{\infty}\sum_{\substack{k=1 \\ k\neq i}}^{N} d_{k,\ell}\alpha_{ik}h_{ik}(t - \ell T_\mathrm{b} - t_{\mathrm{TX}_k} - t_{ik}), \tag{5.6b}$$

where

$$\alpha_{ii} \equiv 1, \text{ while } \alpha_{ik} = \frac{\sqrt{G_{ik}/G_{ii}}}{t_{ik}/t_{ii}} \tag{5.6c}$$

is the overall channel amplitude. In practice, one may want to avoid $\alpha_{ik} > \alpha_{ii}$ and reduce α_{ik} for lower MAI and hence higher SIR. The reduction of α_{ik} may be achieved by beamforming, as suggested by (5.6c), so as to decrease the factor G_{ik}/G_{ii}.

Then, the total decoded signal, which is according to (4.11a) the sum of (5.6a), (5.6b) and $n(t)$, becomes

$$z_i(t) = \sum_{\ell=1}^{\infty} d_{i,\ell} h_{ii}(t - \ell T_\mathrm{b} - t_{\mathrm{TX}_i} - t_{ii}) + \sum_{\ell=1}^{\infty} \sum_{\substack{k=1 \\ k \neq i}}^{N} d_{k,\ell} \alpha_{ik} h_{ik}(t - \ell T_\mathrm{b} - t_{\mathrm{TX}_k} - t_{ik}) + n(t), \tag{5.7}$$

Note that the transmitting delay offset, t_{TX_i}, t_{TX_k}, and channel delay, t_{ii}, t_{ik} are all random variables. The transmitting delay meaningfully varies within $[0, T_\mathrm{b}]$, given that $\tilde{s}_i(t)$ and $x_i(t)$ in (5.6) are both periodic functions with period $T_\mathrm{b} = 2\Delta\tau$. Thus,

$$t_{\mathrm{TX}_i},\ t_{\mathrm{TX}_k} = \mathcal{U}\left(0, T_\mathrm{b}\right), \text{ with } T_\mathrm{b} = 2\Delta\tau, \tag{5.8}$$

where $\mathcal{U}\left(0, T_\mathrm{b}\right)$ denotes the uniform distribution with support $[0, T_\mathrm{b}]$. The channel delay is a uniform random variable, corresponding to

$$t_{ii},\ t_{ik} = \mathcal{U}\left(d_{\min}/c, d_{\max}/c\right), \tag{5.9}$$

where $d_{\min}$ and $d_{\max}$ are the minimum and maximum communication distances, and are respectively set to range from 5 to 10 meters in later characterization. Finally, the overall channel amplitude, α_{ik} [Eq. (5.6c)], while being affected by the channel delay ratio t_{ik}/t_{ii}, which is random based on (5.9), depends on the antenna gain ratio, $\sqrt{G_{ik}/G_{ii}}$, which may be tuned using beam forming. Therefore, one is able to control α_{ik} for a desired value. We will later consider two particular cases for α_{ik}^2 (energy), 1) $\alpha_{ik}^2 = \alpha_{ii}^2 \equiv 1$, i.e. all MAI channel energies are equal to the desired signal channel energy, 2) $\alpha_{ik}^2 \equiv 0.1 < \alpha_{ii}^2$, i.e. all MAI channel energies are 10 dB less than the desired signal channel energy.

One may next determine the statistical distribution of the MAI, $x_i(t)$ [Eq. (5.6b)], which is described by the corresponding probability density function (PDF). The analytical derivation of the PDF of MAI is beyond the scope of this dissertation, and readers are referred to specialized works in this area for details. For instance, the authors of [116] use the normal distribution to approximate the MAI distribution in Bragg grating fiber based frequency

hopping multiple access, while the authors of [17] analytically show that MAI asymptotically approaches the normal distribution with increased frames per symbol in time-hopping multiple access. Here, we will numerically show that the MAI distribution in Chebyshev coding DCMA may also be approximated by the normal distribution.

For this purpose, we use the random variable x_i as the time sample of the MAI, so that

$$x_i \in \boldsymbol{x}_i = \{x_{i,1}, \ldots, x_{i,p}, \ldots, , x_{i,L}\}, \text{ where } x_{i,p} = x_i(pt_\mathrm{s}), \quad p \in \mathbb{Z}, \tag{5.10}$$

and t_s is sampling period, $L = 2T_\mathrm{b}/t_\mathrm{s}$ is the sample length, and $x_{i,p}$ is the time sample in (5.6b) at pt_s. At this point, we statistically compute the corresponding mean ($\mu_{\mathrm{X},i}$) and standard deviation ($\sigma_{\mathrm{X},i}$) of x_i as

$$\mu_{\mathrm{X},i} = \frac{1}{L}\sum_{p=1}^{L} x_{i,p}, \quad \sigma^2_{\mathrm{X},i} = \frac{1}{L}\sum_{p=1}^{L}(x_{i,p} - \mu_{\mathrm{X},i})^2, \tag{5.11}$$

with $\sigma^2_{\mathrm{X},i}$ being the average power of MAI $x_i(t)$. For the purpose of plotting the normalized PDF, one first normalizes the random variable x_i and its mean, $\mu_{\mathrm{X},i}$, and standard deviation, $\sigma_{\mathrm{X},i}$, to the peak value of the desired signal [Eq. (4.10a)], i.e.

$$\hat{x}_i = \frac{x_i}{2\Delta f}, \quad \hat{\mu}_{\mathrm{X},i} = \frac{\mu_{\mathrm{X},i}}{2\Delta f}, \quad \hat{\sigma}^2_{\mathrm{X},i} = \frac{\sigma^2_{\mathrm{X},i}}{4\Delta f^2}, \tag{5.12}$$

which provides all the parameters of the normal distribution PDF of $\hat{x}_i$,

$$\mathrm{PDF}_{\mathrm{X},i}(\hat{x}_i) = \frac{1}{\sqrt{2\pi\hat{\sigma}^2_{\mathrm{X},i}}} \exp\left[-\frac{(\hat{x}_i - \hat{\mu}_{\mathrm{X},i})^2}{2\hat{\sigma}^2_{\mathrm{X},i}}\right], \tag{5.13}$$

while the PDF could also be obtained by counting the occurrences of the different values of $\hat{x}_i$.

Note that the normalized MAI variance, $\hat{\sigma}^2_{\mathrm{X},i}$, is the interference to signal power ratio, which is exactly the opposite of SIR, i.e.

$$\mathrm{SIR}_i = \frac{1}{\hat{\sigma}^2_{\mathrm{X},i}}. \tag{5.14}$$

In Sec. 4.3.3, we have derived the MAI power and SIR for the case of equal channel energy ($\alpha^2_{i,k} = \alpha^2_{ii} = 1, \forall\, k$) based on the procedure from (4.17) to (4.20), so as to find the relationship between the DSBP (Delay Swing-Bandwidth Product) and SIR. We shall now extend this relationship to cover the case where the channels have different energies ($\alpha^2_{ik} \neq \alpha^2_{ii}$). Note that each $h_{ik}(t)$ in (5.6b) has a factor α_{ik} and hence energy $\alpha^2_{ik}E$, which leads to the average

power of $x_i(t)$

$$P_{\mathrm{X},i} = \frac{\sum_{\substack{k=1 \\ k\neq i}}^{N} \alpha_{ik}^2 E}{2\Delta\tau} = \alpha_i^2 \frac{(N-1)\Delta f}{\Delta\tau}, \tag{5.15a}$$

$$\text{where } \alpha_i^2 = \frac{1}{N-1} \sum_{\substack{k=1 \\ k\neq i}}^{N} \alpha_{ik}^2 \tag{5.15b}$$

is the arithmetic mean of α_{ik}^2, and $E = 2\Delta f$ is the energy of $h_{ik}(t)$ over one bit period ($T_\mathrm{b} = 2\Delta\tau$). The corresponding SIR is then found as

$$\mathrm{SIR}_i' = \frac{4\Delta f^2}{P_{\mathrm{X},i}} = \frac{4\Delta\tau\Delta f}{\alpha_i^2(N-1)} = \frac{4 \cdot \mathrm{DSBP}}{\alpha_i^2(N-1)}. \tag{5.16}$$

The SIR_i' [Eq. (5.16)] and $P_{\mathrm{X},i}$ [Eq. (5.15a)] may be regarded as the equivalents of the statistical SIR_i [Eq. (5.14)] and $\sigma_{\mathrm{X},i}^2$ [Eq. (5.11)], respectively. The former ones [Eqs. (5.16) and (5.15a)] are easier to obtain than latter ones [Eqs. (5.14) and (5.11)] and, more importantly, provide physical insights : the SIR and MAI power are linearly proportional to $\Delta\tau\Delta f$ (DSBP) and $\Delta f/\Delta\tau$, respectively, which will be confirmed by different numerical examples.

Figure 5.1 shows three examples of 2×2 DCMA coding sets and their corresponding cascaded group delays, waveforms and MAI distributions in a noiseless channel with identical energies ($\alpha_{ik}^2 = \alpha_{ii}^2 = 1$). In these examples, only one MAI contribution exists. For the coding order $m_i \neq \pm 1$ [Eq. (4.14)], the actual MAI distribution agrees well with the normal distribution given by (5.13) [Fig. 5.1(c) second and third columns]. However, when $m_i = \pm 1$, the approximation of normal distribution does not hold [Fig. 5.1(c) first column]. In this case, the MAI is found to correspond to the arcsine distribution [120] [1],

$$\mathrm{PDF}_{\mathrm{X},i}(\hat{x}_i) = \frac{1}{\pi\sqrt{(\hat{x}_i - a)(b - \hat{x}_i)}},\ \hat{x}_i \in [a, b],\ \text{and } b = -a = \sqrt{2}\hat{\sigma}_{\mathrm{X},i}. \tag{5.17}$$

Section 5.1.3 will discuss the $m_i = \pm 1$ codes for the $N = 2$ DCMA system, and exclude $m_i = \pm 1$ for $N \geq 2$.

The MAI distributions are found to be always symmetric about $\hat{x}_i = 0$, i.e. $\mu_{\mathrm{X},i} \equiv 0$, which is easily explained from the fast polar oscillation of $\hat{x}_i(t)$ about zero and the consequent global cancellation in the corresponding average process in (5.11).

The $\hat{\sigma}_{\mathrm{X},i}^2$ [interference to signal ratio : Eq (5.12)] values in Fig. 5.1(c) are computed by (5.11) and normalized by $4\Delta f^2$ based on statistical procedures. It is found that reducing the band-

1. The arcsine distribution exhibits a pair of sharp rays at the polar (boundary) value corresponding to the quasi-uniform amplitude of the waveform [see for instance Fig. 4.4(a) for the $(i,k) = (1,2)$], and decreasing magnitude towards zero, corresponding to faster transitions between positive and negative signal values.

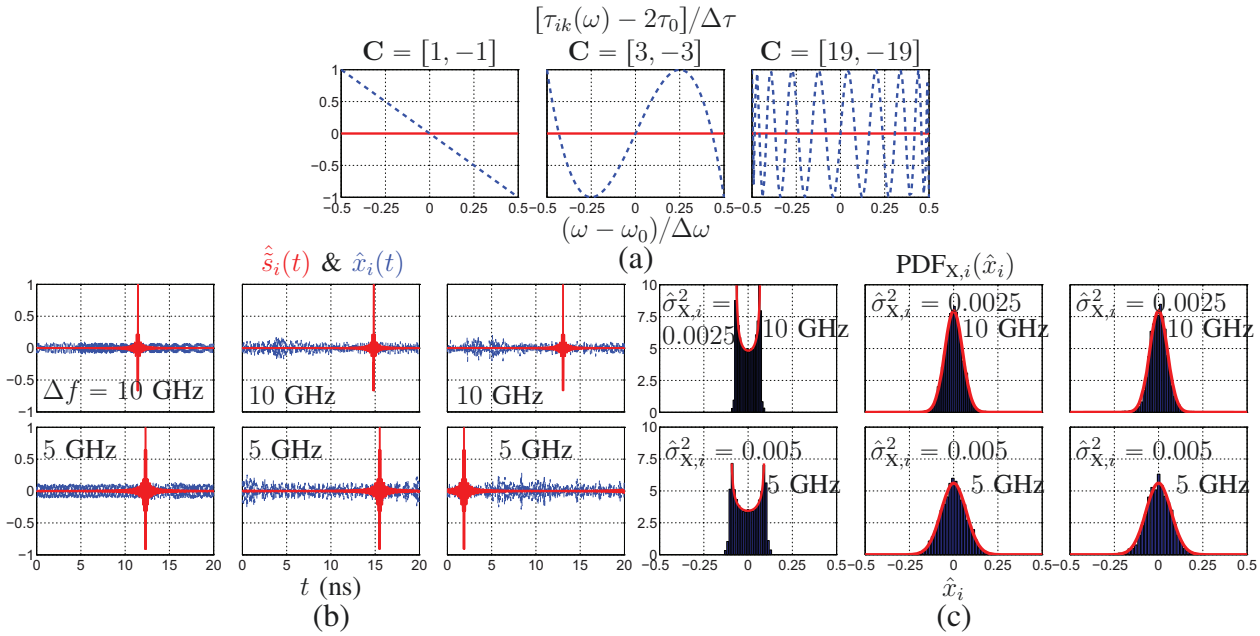

Figure 5.1 Three 2×2 DCMA examples (corresponding to the three columns) with $\sigma^2_{\mathrm{N}} = 0$ (noiseless), $\alpha^2_{ik} \equiv 1\,(\forall\, k \neq i)$. (a) Code sets $\mathbf{C}$ and corresponding cascaded group delays $\tau_{ik}(\omega)$ [Eq. (4.9) with (4.13) and $\Delta\tau = 10$ ns] with $(i, k) = (1, 1)$ (red solid) and $(i, k) = (1, 2)$ (blue dashed). (b) Corresponding waveforms over one bit, $T_{\mathrm{b}} = 2\Delta\tau = 20$ ns : desired signal $\hat{\tilde{s}}_i(t)$ (red solid) and MAI $\hat{x}_i(t)$ (blue dashed) [Eq. (5.6) normalized by $2\Delta f$] for $\Delta f =$ 10 GHz and $\Delta f = 5$ GHz cases. (c) Corresponding actual MAI distribution (blue bars) and approximated arcsine (first column) and normal (second and third columns) distribution (red curves) [Eq. (5.13)] with $\hat{\sigma}^2_{\mathrm{X},i}$ values [interference to signal ratio : Eq. (5.12)] for $\Delta f = 10$ GHz and $\Delta f = 5$ GHz cases (L. Zou, et al [16], TWC, © [2017] IEEE).

width by half doubles $\hat{\sigma}^2_{\mathrm{X},i}$, and hence halves the SIR according to (5.14), i.e. SIR is linearly proportional to Δf, as predicted by the last-but-one equality in (5.16). Similarly, we have numerically verified that fixing Δf and varying $\Delta\tau$ yields SIR linearly proportional to $\Delta\tau$, confirming that SIR is also linearly proportional to $\Delta\tau$, also as predicted by the last-but-one equality in (5.16). Thus, SIR is, globally, linearly proportional to DSBP ($\Delta\tau\Delta f$), as indicated by the last equality in Eq. (5.16).

Figure 5.1(b) plots the normalized DCMA waveforms, $\hat{\tilde{s}}_i(t) = \tilde{s}_i(t)/(2\Delta f)$ and $\hat{x}_i(t) = x_i(t)/(2\Delta f)$ for $\Delta f = 10$ GHz and $\Delta f = 5$ GHz to investigate how SIR is affected by the change of bandwidth. It is seen that the normalized MAIs for $\Delta f = 5$ GHz case are higher than their 10 GHz counterparts, corresponding to lower SIR.

Finally, Fig. 5.2 plots the waveforms and MAIs with $\mathbf{C} = [3, -3, 19, -19]$, $\Delta\tau = 10$ ns and $\Delta f = 10$ GHz in a 4×4 DCMA system. MAI still follows the normal distribution.

The corresponding $\hat{\sigma}^2_{\mathrm{X},i}$ values, computed by (5.11), normalized by $4\Delta f^2$ [Eq. (5.12)], and indicated in the figure, agree with those computed by (5.15a) with different $\alpha^2_{ik}\,(\forall\, k \neq i)$, $N = 4$, $\Delta\tau = 10$ ns and $\Delta f = 10$ GHz and normalized by $4\Delta f^2$. It is observed that the MAI signal reaches the level of the desired signal at around $\alpha^2_{ik} \equiv 10$, corresponding to SIR ≈ 13.3 [Eq (5.14) with $\hat{\sigma}^2_{\mathrm{X}} = 0.075$]. For other Δf, $\Delta\tau$ and N, a different α_{ik} may be required to achieve the same SIR (13.3) according to (5.16) and (5.15b). A study similar to that in Fig. 5.2 may be generally performed for any combination of Δf, $\Delta\tau$ and N to assess the robustness of the system to unequal MAI powers. In case, the SIR is too small, beamforming may be introduced, as will be presented in Sec. 5.1.3.

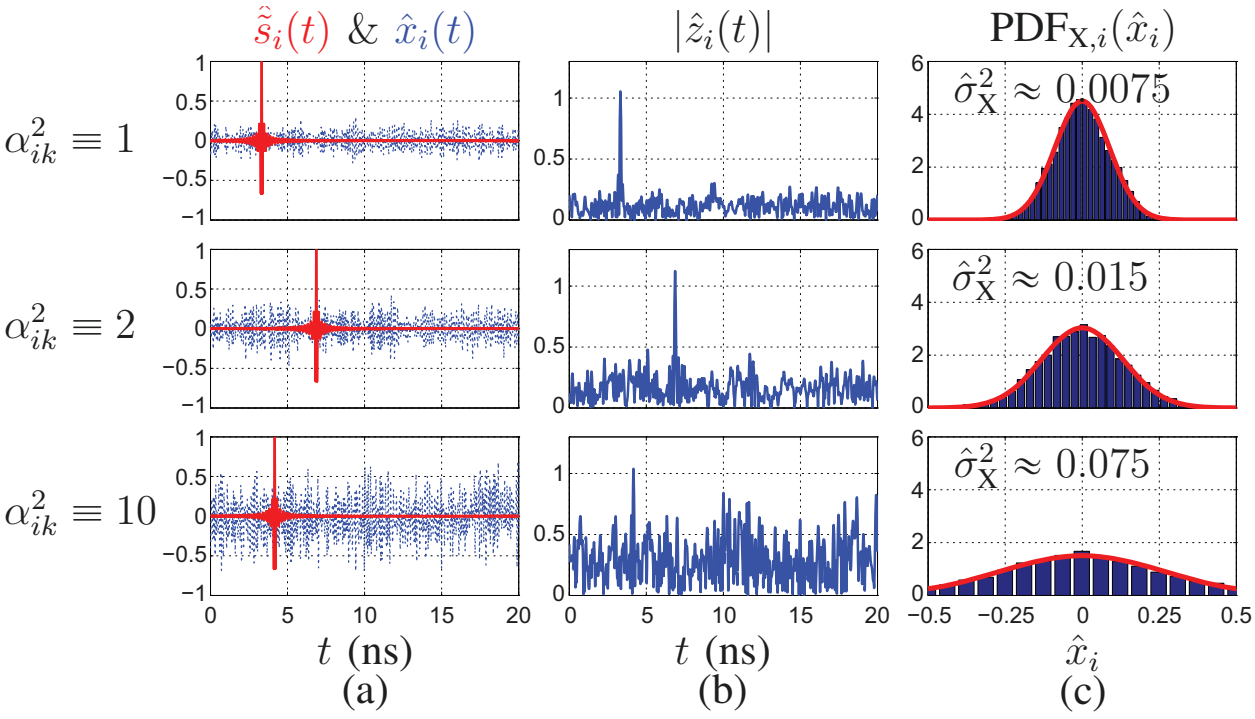

Figure 5.2 Illustration of the effect of unequal MAI powers (α^2_{ik}, $k \neq i$), considering a 4×4 DCMA system with $\mathbf{C} = [3, -3, 19, -19]$, $\Delta\tau = 10$ ns, $\Delta f = 10$ GHz, $\sigma^2_{\mathrm{N}} = 0$ for different $\alpha^2_{ik}\,(\forall\, k \neq i)$. (a) Desired signal, $\hat{\tilde{s}}_i(t)$ (red solid) and MAI, $\hat{x}_i(t)$ (blue dashed) [Eq. (5.6) normalized by $2\Delta f$]. (b) Decoded signal envelope, $|\hat{z}_i(t)|$ [Eq. (5.7) normalized by $2\Delta f$]. (c) Actual MAI distribution (bars) and approximated normal distribution [Eq. (5.13)] with $\hat{\sigma}^2_{\mathrm{X},i}$ values [Eq. (5.12)] (L. Zou, et al [16], TWC, © [2017] IEEE).

5.1.3 BEP Analysis

$N \geq 2$ DCMA System

For $N \geq 2$, we consider here $m_i \neq \pm 1$, in order to avoid different distributions, for simplicity. We may now add the AWGN onto MAI, corresponding to the Signal-to-Noise Ratio (SNR)

$$\mathrm{SNR} = \frac{4\Delta f^2}{\sigma_{\mathrm{N}}^2} = \frac{1}{\hat{\sigma}_{\mathrm{N}}^2}, \tag{5.18}$$

where $\hat{\sigma}_{\mathrm{N}}^2 = \sigma_{\mathrm{N}}^2/(4\Delta f^2)$ is the normalized noise power for the random variable $\hat{n} = n/(2\Delta f)$. Assuming, for simplicity, that SNR [Eq. (5.18)] is identical for all receivers (RX_i), and that MAI and AWGN are statistically independent, the total interference $\hat{u}$ (normalized), which is the sum of the two random variables $\hat{x}_i$ and $\hat{n}$, i.e. $\hat{u} = \hat{x}_i + \hat{n}$, also follows the normal distribution, i.e.

$$\mathrm{PDF}_i(\hat{u}) = \frac{1}{\sqrt{2\pi(\hat{\sigma}_{\mathrm{X},i}^2 + \hat{\sigma}_{\mathrm{N}}^2)}} \exp\left[-\frac{\hat{u}^2}{2(\hat{\sigma}_{\mathrm{X},i}^2 + \hat{\sigma}_{\mathrm{N}}^2)}\right], \tag{5.19}$$

with total zero mean and total variance $\hat{\sigma}^2 = \hat{\sigma}_{\mathrm{X}}^2 + \hat{\sigma}_{\mathrm{N}}^2$. The variance $\hat{\sigma}^2$ is equivalent to the normalized interference power. Therefore, the Signal to Interference and Noise Ratio (SINR) is

$$\mathrm{SINR}_i = \frac{1}{\hat{\sigma}_{\mathrm{X},i}^2 + \hat{\sigma}_{\mathrm{N}}^2} = \frac{1}{\frac{1}{\mathrm{SIR}_i} + \frac{1}{\mathrm{SNR}}}. \tag{5.20}$$

Assume the worst case case scenario $d_{k,\ell} \equiv 1\,(\forall\, k \neq i)$ in (5.6b), i.e. all undersired transmitters are sending only 1's, leading to maximal MAI energy, and assume that the desired signal amplitude is normalized and detected with a threshold of 0.5. When a bit $d_{i,\ell} = 1$ is sent [desired transmitter, Eq. (5.6a)], $1 + \hat{x} + \hat{n} < 0.5$ ($\hat{u} < -0.5$) corresponds to an error, whereas when a bit $d_{i,\ell} = 0$ is sent (desired transmitter), $0 + \hat{x} + \hat{n} > 0.5$ ($\hat{u} > 0.5$) corresponds to an error. The BEP is thus the following integral of (5.19) over $\hat{u} \in (-\infty, -0.5)$ and $\hat{u} \in (0.5, \infty)$ [19] :

$$\begin{aligned} \mathrm{BEP}_i &= \mathrm{P}(\hat{u} < -0.5 | d_{i,\ell} = 1) + \mathrm{P}(\hat{u} > 0.5 | d_{i,\ell} = 0) \\ &= 0.5 \int_{-\infty}^{-0.5} \mathrm{PDF}_i(\hat{u})\, d\hat{u} + 0.5 \int_{0.5}^{-\infty} \mathrm{PDF}_i(\hat{u})\, d\hat{u}, \end{aligned} \tag{5.21}$$

where equal transmission probability (0.5) has been assumed for bits 1 and 0. Inserting (5.19) into (5.21) yields after some algebraic manipulations

$$\mathrm{BEP}_i = \frac{1}{\sqrt{2\pi}} \int_{\mathrm{SINR}_i/2}^{\infty} \exp\left(-\frac{x'^2}{2}\right) dx' = \mathrm{Q}\left(\frac{\sqrt{\mathrm{SINR}_i}}{2}\right) \tag{5.22}$$

Particularly, when $\sigma_{\mathrm{N}}^2 = 0$ (noiseless channel),

$$\mathrm{BEP}_i|_{\sigma_{\mathrm{N}}^2=0} = \mathrm{Q}\left(\frac{\sqrt{\mathrm{SIR}_i}}{2}\right), \tag{5.23}$$

with SIR_i given by (5.14) or (5.16). The overall BEP is the average of BEP_i over all receivers, i.e.

$$\mathrm{BEP} = \frac{1}{N}\sum_{i=1}^{N}\mathrm{BEP}_i. \tag{5.24}$$

Figure 5.3 plots BEP as function of N for a DCMA system with the all-odd coding set

$$\mathbf{C} = [3, -3, \ldots, N+2],\ N \text{ is odd, or } = [3, -3, \ldots, N+1, -(N+1)],\ N \text{ is even}, \tag{5.25}$$

in noiseless channels with unique channel energy $[\alpha_{ik}^2 \equiv 1\,(\forall\, k \neq i)]$. This scenario typically resembles that of a downlink communication, where all the channels share a unique transmitting antenna and send signals at the same power level, such that the desired signal and MAI arrive at the receiver with same energy. We see that, in this case, the BEP with argument given by (5.14) and (5.16) are identical. Changing the group delay swing and changing the bandwidth have identical effect on the BEP. In general, the BEP degrades as N increases, as a result of MAI accumulation and hence degraded SIR according to (5.16). Such degradation of SIR can be naturally mitigated by increasing the group delay swing, $\Delta\tau$ [Fig. 5.3(a)]. However, the corresponding bit rate $[R_{\mathrm{b}} = 1/(2\Delta\tau)]$ has to be consequently decreased to avoid inter-symbol interference, which degrades the spectral efficiency (bit rate per unit bandwidth) given the assumed fixed bandwidth. Another efficient way to enhance SIR, without affecting the bit rate, is increasing the bandwidth Δf [Fig. 5.3(b)]. However, this also degrades the spectral efficiency. In general, the DSBP is the critical figure of merit for DCMA SIR and spectral efficiency, and hence DCMA at large. We also make comparison between DCMA and the DSP based IR UWB multiple access technique, showing better performance for DCMA technique. It is also worth mentioning that, since DCMA is the world's first real-time UWB IR multiple access technique, it is therefore hard to make a thorough comparison with different technologies.

In practice, one may further reduce MAI by achieving $\alpha_{ik}^2 < \alpha_{ii}^2 = 1$, $\forall\, k \neq i$ [Eq. (5.6c)] with beam forming, which is practically feasible. Figure 5.4 plots BEP but with $\alpha_{ik}^2 \equiv 0.1$, $\forall\, k \neq i$, so as to ensure $\alpha_{ik}^2 < \alpha_{ii}^2 = 1$, $\forall\, k \neq i$. The mean of α_{ik}^2, α_i^2 is given by (5.15b), which yields $\alpha_i^2 = 0.1$ and, according to (5.16), corresponds to SIR enhancement by a factor of $1/\alpha_i^2 = 10$ (10 dB). The BEP results based on Eq. (5.14) (sold lines) agree with those based on (5.16) with $\alpha_i^2 = 0.1$ (circle marks). In this scenario, the SIR enhancement via α_{ik}^2 decrease allows

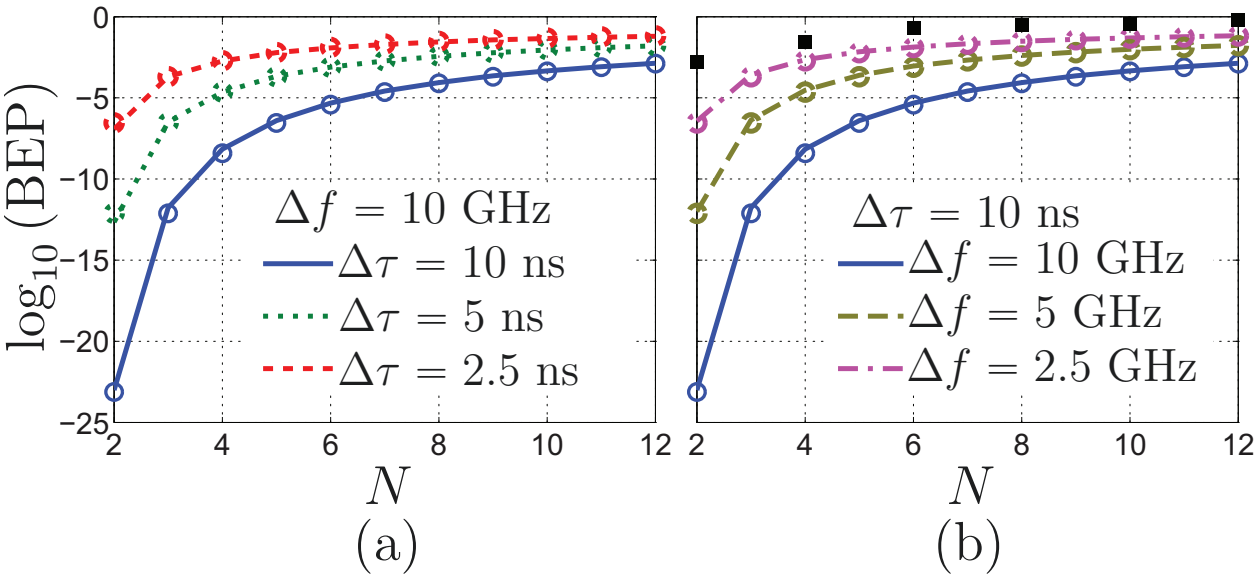

Figure 5.3 BEP [bit rate $R_\mathrm{b} = 1/(2\Delta\tau)$] versus N for an all-odd DCMA system with coding (5.25), $\sigma_\mathrm{N}^2 = 0$, and $\alpha_{ik}^2 \equiv 1\,(\forall\, k \neq i)$. These results are computed by (5.23) and (5.24) with SIR argument given by Eq. (5.14) (Sold lines) or Eq. (5.16) with $\alpha_i^2 = 1$ (circle marks). (a) Fixed bandwidth, $\Delta f = 10$ GHz and varying group delay swing, $\Delta\tau$. (b) Fixed $\Delta\tau = 10$ ns and varying Δf, compared with the performance (black square) of DSP based time hoping IR UWB multiple access technique in [17], with comparable bandwidth (2.5 GHz), where the DCMA provides better BEP performance with higher speed (50 Mbps) corresponding to the magenta curve (L. Zou, et al [16], TWC, © [2017] IEEE).

one to reduce DSBP for a given BEP, which reduces the phaser constraints [6].

We shall now see that reducing DSBP also leads to increased spectral efficiency at the expense of lower SIR and BEP. The spectral efficiency is defined as the system capacity, C, divided by the system bandwidth, Δf, and is measured in bit per second per Hertz (b/s/Hz). The capacity may be simply expressed as the maximum overall data throughput, $NR_\mathrm{b} = N/T_\mathrm{b} = N/(2\Delta\tau)$, where $R_\mathrm{b} = 1/(2\Delta\tau)$ is the maximum allowed bit rate. The spectral efficiency is then

$$\eta = \frac{C}{\Delta f} = \frac{N}{2\Delta\tau\Delta f} = \frac{N}{2\cdot \mathrm{DSBP}}, \tag{5.26}$$

which is inversely proportional to DSBP. Thus, reducing DSBP indeed enhances η, while degrading SIR and hence the BEP performance, according to (5.16) and (5.23). However, the additional freedom of α_i^2 [Eq. (5.15b) with (5.6c)], which may be activated by beam forming, i.e. controlling $\sqrt{G_{ik}/G_{ii}}$ in (5.6c), allows one to increase η without increasing SIR and BEP. Suppose for instance that $N = 12$ and that desired spectral efficiency is $\eta = 1$ b/s/Hz, or DSBP $= \Delta\tau\Delta f = 6$, which yields upon insertion into (5.16) SIR $= 24/(11\alpha_i^2)$. If $\alpha_i^2 =$

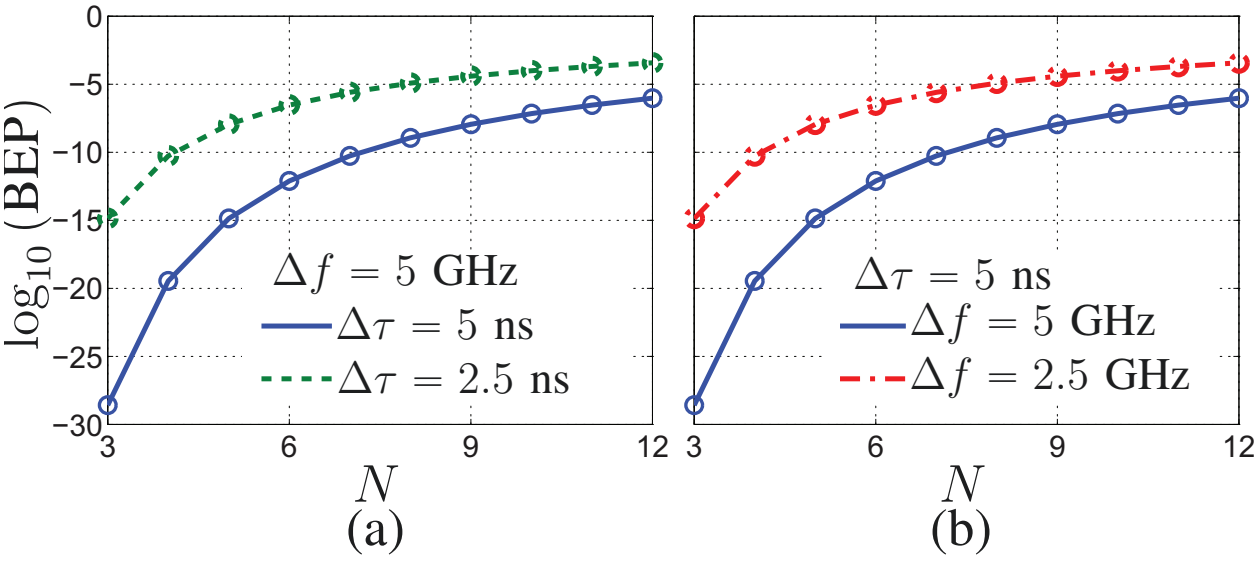

Figure 5.4 BEP $[R_{\rm b} = 1/(2\Delta\tau)]$ versus N for an all-odd DCMA system [Eq. (5.25)] with $\sigma_{\rm N}^2 = 0$, $\alpha_{ik}^2 \equiv 0.1\,(\forall\, k \neq i)$. These results are computed by (5.23) and (5.24) with SIR argument given by Eq. (5.14) (solid lines) or by Eq. (5.16) with $\alpha_i^2 = 0.1$ (circle marks). (a) Fixed $\Delta f = 5$ GHz and varying $\Delta\tau$. (b) Fixed $\Delta\tau = 5$ ns and varying Δf (L. Zou, et al [16], TWC, © [2017] IEEE).

1, SIR = 2.2, which is too low for acceptable BEP. Specifying $\text{BEP}_{\max} = 0.01$, found to correspond to SIR = 22 upon inverting (5.23), leads to $1/\alpha_i^2 \geq 10$ (10 dB), which may be achieved using beam forming with proper gains in (5.6c).

Figure 5.5 plots BEP versus SNR for an all-odd DCMA system with $\Delta\tau = 10$ ns, $\Delta f = 10$ GHz, and AWGN channels with identical energy $[\alpha_{ik}^2 \equiv 1\,(\forall\, k \neq i)]$. As SNR increases, BEP asymptotically approaches the corresponding noiseless BEP values given in Fig. 5.3, as expected. As SNR decreases below 15 dB, the three BEP curves converge to the same value, which indicates that in the SNR range SNR < 15 dB the total interference is dominated by AWGN. Figure 5.5 conveniently indicates the SNR requirement for a specified BEP level and DCMA dimension. For instance, for BEP of 10^{-3}, one finds that SNR should be larger than 16 dB and 20 dB for the $N = 4$ and $N = 8$ cases, respectively, whereas BEP for $N = 12$ is always larger than the specified value (10^{-3}) even as SNR approaches infinity.

$N = 2$ DCMA System

For this case, we restrict our study to the coding set $\mathbf{C} = [+1, -1]$, used in the experiment of Sec. 4.5 and corresponding to the arcsine MAI distribution (5.17), with finite support

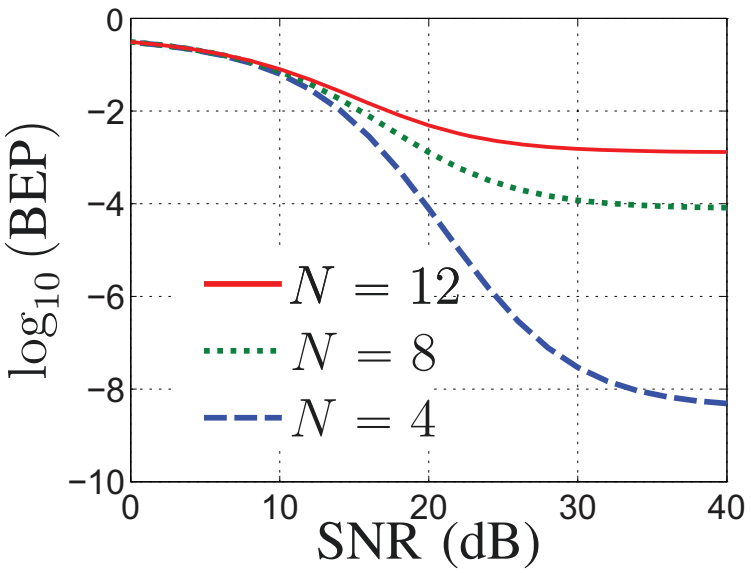

Figure 5.5 BEP versus SNR for DCMA with all-odd coding[Eq. (5.25)], $\Delta f = 10$ GHz, $\Delta\tau = 10$ ns in AWGN channel with $\alpha_{ik}^2 \equiv 1\,(\forall\, k \neq i)$. These results are computed by (5.22) and (5.24) with (5.20) and SIR_i given by (5.16) with $\alpha_i^2 = 1$. (L. Zou, et al [16], TWC, © [2017] IEEE).

$\hat{x}_i \in [-\sqrt{2}\hat{\sigma}_{\mathrm{X}_i}, \sqrt{2}\hat{\sigma}_{\mathrm{X}_i}]$ and symmetry about the zero mean. If $\sqrt{2}\sigma_{\mathrm{X}_i}$ is smaller than the detection threshold, which here is 0.5 (after normalization), as in the analysis of Sec. 5.1.3, the BEP is always zero. We assume $\sigma_{\mathrm{N}}^2 = 0$ (noiseless channel), and separately consider the case of bits "1" and "0" being sent. If $d_{i,\ell} = 1$ is sent, and $1 + \min(\hat{x}_i) = 1 - \sqrt{2}\hat{\sigma}_{\mathrm{X}_i} > 0.5$ ($\sqrt{2}\hat{\sigma}_{\mathrm{X}_i} < 0.5$), the bit "1" is correctly detected. If $d_{i,\ell} = 0$ is sent, and $0 + \max(\hat{x}_i) = \sqrt{2}\hat{\sigma}_{\mathrm{X}_i} < 0.5$ ($\sqrt{2}\hat{\sigma}_{\mathrm{X}_i} < 0.5$), the bit "0" is correctly detected. So, the correct detection criterion is the same for "1" and "0" in the case of the 0.5 threshold, and this criterion – $\hat{\sigma}_{\mathrm{X}_i} < 1/(2\sqrt{2})$ – ensures zero BEP. First substituting $N = 2$ into (5.16) and next equating the result to (5.14) with $\hat{\sigma}_{\mathrm{X}_i} < 1/(2\sqrt{2})$ leads to

$$\mathrm{SIR}_i = \frac{4 \cdot \mathrm{DSBP}}{\alpha_{ik}^2} = \frac{1}{\hat{\sigma}_{\mathrm{X}_i}^2} > 8. \tag{5.27a}$$

Finally, solving (5.27a) for the DSBP yields

$$\mathrm{DSBP} > 2\alpha_{ik}^2. \tag{5.27b}$$

In the particular case of equal signal and MAI energies ($\alpha_{ik}^2 = 1$, $\forall i, k$), as in the experiment (Sec. 4.5), Eq. (5.27b) becomes $\mathrm{DSBP} > 2$. In the experiment, the DSBP was set to 4 ($\Delta f = 4$ GHz, $\Delta\tau = 1$ ns), which corresponds to a margin of factor 2 in (5.27b), and the

measured SIR in Fig. 4.22(d) was about 10 to 12, consistently with (5.27a).

5.2 NLOS Channel Characterization

So far, we have only characterized the DCMA system for LOS channel. However, in practice, wireless channel is typically NLOS, i.e. exhibits multipath fading or dispersion [129]. Such multipath fading results in multiple resolvable instances of the original UWB pulses, and consequent lower SIR and worse BEP performance [130]. Moreover, the DCMA system presented so far can only route signals between fixed communication pairs, and practical communication system typically requires dynamic routing.

For channel dispersion compensation and for dynamic routing between arbitrary pairs, an adaptivity strategy must be incorporated. One solution may be to use phasers that are dynamically tuned in real time for group delay equalization between any arbitrary access point pair [15], but the technology for such phasers is complex and still at an early development stage. For this reason, we propose a routing station, or router, where the routing may be efficiently performed by using time reversal [131–133].

5.2.1 System Description

Figure 5.6 shows a diagrammatic representation of the proposed Time-Reversal Dispersion Code Multiple Access (TR-DCMA) routing system with $2M$ access points (AP) and the router with endowed with time reversal capability. Uplink $\mathrm{AP}^{\mathrm{U}}_{m}$, $m \in \{1, \ldots, M\}$, communicates with downlink $\mathrm{AP}^{\mathrm{D}}_{n(m)}$, $n(m) \in \{1, \ldots, M\}$, via the router, where $n(m)$ is a function of m corresponding to the desired routing link from access point m to access point n, with $n(m_1) \neq n(m_2)$ for $m_1 \neq m_2$.

For multiple access purpose, $\mathrm{AP}^{\mathrm{U/D}}_{k}$ is assigned a specific dispersion code, which is the group delay function $\tau^{\mathrm{U/D}}_{k}(\omega)$, provided by the coding phaser [6] that is incorporated in the AP system before/after the antenna. The phaser impulse response $g^{\mathrm{U/D}}_{k}(t)$ is found by inverse Fourier transforming ($\mathcal{F}^{-1}$) the transfer function $G^{\mathrm{U/D}}_{k}(\omega)$ as

$$g^{\mathrm{U/D}}_{k}(t) = \mathcal{F}^{-1}\left[G^{\mathrm{U/D}}_{k}(\omega)\right] = \mathcal{F}^{-1}\left[\mathrm{rect}\left(\frac{\omega-\omega_0}{\Delta\omega}\right) e^{j\phi^{\mathrm{U/D}}_{k}(\omega)}\right], \tag{5.28a}$$

where

$$\phi^{\mathrm{U/D}}_{k}(\omega) = -\int_{\omega_0-\Delta\omega/2}^{\omega} \tau^{\mathrm{U/D}}_{k}(\omega')\, d\omega', \tag{5.28b}$$

and $\tau^{\mathrm{U/D}}_{k}(\omega)$ are the phaser transfer phase and group delay (dispersion code), respectively, and $\omega_0 = 2\pi f_0$, $\Delta\omega = 2\pi\Delta f$ are the center frequency and bandwidth, respectively. The

wireless channel between the AP (after/before the phaser) and the router, denoted as $w_k^{\mathrm{U/D}}(t)$, naturally includes the AP and the router antenna impulse responses in the communication direction and typically exhibits multipath fading [85].

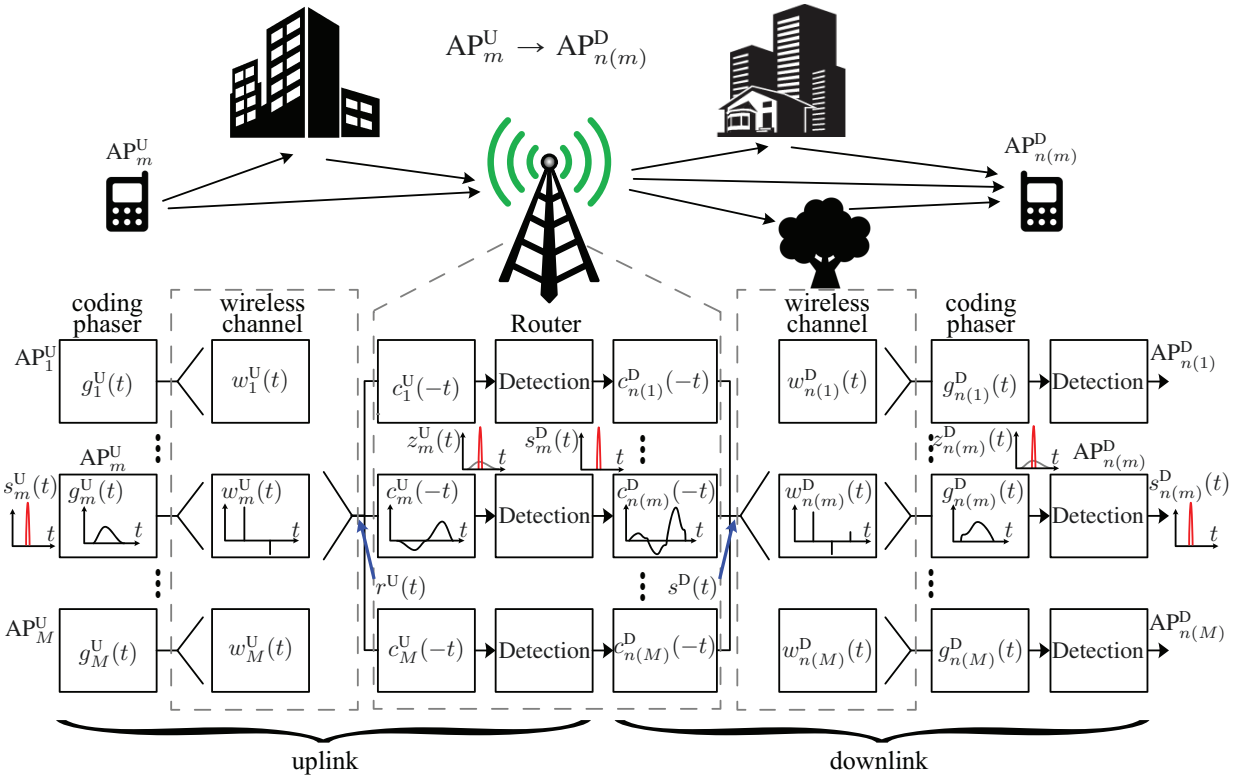

Figure 5.6 Diagrammatic representation of the proposed TR-DCMA system (L. Zou, et al, [18], ArXiv : `https://arxiv.org/abs/1709.08085`).

5.2.2 Modeling

Calibration Phase

During this phase, the $2M$ APs sequentially send a known beacon signal, $s^{\mathrm{B}}(t)$, to the router. The router receives for $\mathrm{AP}_k^{\mathrm{U/D}}$ the signal

$$\begin{aligned} r_k^{\mathrm{B,U/D}}(t) &= \left[(s^{\mathrm{B}} * g_k^{\mathrm{U/D}}) * w_k^{\mathrm{U/D}} \right](t) \\ &= \left(s^{\mathrm{B}} * c_k^{\mathrm{U/D}} \right)(t), \end{aligned} \tag{5.29a}$$

where

$$c_k^{\mathrm{U/D}}(t) = (g_k^{\mathrm{U/D}} * w_k^{\mathrm{U/D}})(t), \tag{5.29b}$$

is the overall channel impulse response, corresponding to the convolution ("$*$") of the corresponding *guided-wave* channel (coding phaser) and *wireless* channel impulse response.

Since $s^{\mathrm{B}}(t)$ is known, $c_k^{\mathrm{U/D}}(t)$ can be determined from (5.29a) by the router. This may be done either digitally or analogically. In the former case, the measured signal $r_k^{\mathrm{U/D}}(t)$ is stored, then numerically deconvolved and flipped, i.e. $c_k^{\mathrm{U/D}}(t) \to c_k^{\mathrm{U/D}}(-t)$, and finally reconverted to the analog domain. In the latter case, $r_k^{\mathrm{U/D}}(t)$ is immediately deconvolved by the (known) time-reversed version of $s^{\mathrm{B}}(t)$, $s^{\mathrm{B}}(-t)$, using a real-time convolver [32], yielding $c_k^{\mathrm{U/D}}(t)$, which is itself time-reversed by a real-time time reverser [69] into $c_k^{\mathrm{U/D}}(-t)$.

Communication Phase

• *Uplink Transmission*

Assume the worst-case scenario where the M uplink APs are sending their signals at the same time. Denoting $s_m^{\mathrm{U}}(t)$ the signal sent from $\mathrm{AP}_m^{\mathrm{U}}$, the signal received by the router is

$$r^{\mathrm{U}}(t) = \sum_{m=1}^{M} \alpha_m^{\mathrm{U}} s_m^{\mathrm{U}}(t) * c_m^{\mathrm{U}}(t), \tag{5.30}$$

where $\alpha_m^{\mathrm{U}} > 0$ is the sent signal magnitude. The decoding of the signal from $\mathrm{AP}_m^{\mathrm{U}}$ at the router consists in convolving $r^{\mathrm{U}}(t)$ with the time-reversed version of the corresponding channel impulse response $c_m^{\mathrm{U}}(-t)$ constructed in the calibration phase [Sec. (5.2.2)]. Thus,

$$z_m^{\mathrm{U}}(t) = r^{\mathrm{U}}(t) * c_m^{\mathrm{U}}(-t) = \tilde{s}_m^{\mathrm{U}}(t) + x_m^{\mathrm{U}}(t), \tag{5.31a}$$

with the desired signal

$$\tilde{s}_m^{\mathrm{U}}(t) = \alpha_m^{\mathrm{U}} s_m^{\mathrm{U}}(t) * c_m^{\mathrm{U}}(t) * c_m^{\mathrm{U}}(-t) \approx \alpha_m^{\mathrm{U}} s_m^{\mathrm{U}}(t), \tag{5.31b}$$

is an approximation of the desired signal, $s_m^{\mathrm{U}}(t)$, the approximation (rather equality) being due to the finite calibration time in (5.29b) [2], and

$$x_m^{\mathrm{U}}(t) = c_m^{\mathrm{U}}(-t) * \sum_{\substack{k=1 \\ k \neq m}}^{M} \alpha_k^{\mathrm{U}} s_k^{\mathrm{U}}(t) * c_k^{\mathrm{U}}(t), \tag{5.31c}$$

is a distortion signal called multiple-access interference (MAI).

At this point, the uplink signal $z_m^{\mathrm{U}}(t)$ in (5.31), including the desired information $\tilde{s}_m^{\mathrm{U}}(t)$ and

2. If the calibration time were infinite, then we would have an equality from the identity $c_m^{\mathrm{U}}(t) * c_m^{\mathrm{U}}(-t) = \delta(t)$. In practice, $c_m^{\mathrm{U}}(t)$ in (5.31b) is a *truncated* version of the ideal $c_m^{\mathrm{U}}(t)$ function.

interference from the other channels $x_m^{\mathrm{U}}(t)$, is passed through a threshold detector in the router (Fig. 5.6), which transforms it into the signal $s_m^{\mathrm{D}}(t)$.

• *Downlink Transmission*

In the downlink transmission process, the signal $s_m^{\mathrm{D}}(t)$ is to be routed to $\mathrm{AP}_{n(m)}^{\mathrm{D}}$, the desired corresponding access point, that generally varies in time. For this purpose, it is first predistorted by convolution with the time-reversed version of the corresponding downlink channel impulse response, $c_{n(m)}^{\mathrm{D}}(-t)$. Then, the M predistorted signals are combined and sent by the antenna of the router as

$$s^{\mathrm{D}}(t) = \sum_{m=1}^{M} \alpha_m^{\mathrm{D}} s_m^{\mathrm{D}}(t) * c_{n(m)}^{\mathrm{D}}(-t), \;\; \alpha_m^{\mathrm{D}} > 0. \tag{5.32}$$

After passing the wireless channel $w_{n(m)}^{\mathrm{D}}(t)$, this signal is decoded by phaser $g_{n(m)}^{\mathrm{D}}(t)$ as

$$\begin{aligned} z_{n(m)}^{\mathrm{D}}(t) &= s^{\mathrm{D}}(t) * w_{n(m)}^{\mathrm{D}}(t) * g_{n(m)}^{\mathrm{D}}(t) \\ &= s^{\mathrm{D}}(t) * c_{n(m)}^{\mathrm{D}}(t) = \tilde{s}_{n(m)}^{\mathrm{D}}(t) + x_{n(m)}^{\mathrm{D}}(t), \end{aligned} \tag{5.33a}$$

where

$$\tilde{s}_{n(m)}^{\mathrm{D}}(t) = \alpha_m^{\mathrm{D}} s_m^{\mathrm{D}}(t) * c_{n(m)}^{\mathrm{D}}(-t) * c_{n(m)}^{\mathrm{D}}(t) \approx \alpha_m^{\mathrm{D}} s_m^{\mathrm{D}}(t) \tag{5.33b}$$

and

$$x_{n(m)}^{\mathrm{D}}(t) = c_{n(m)}^{\mathrm{D}}(t) * \sum_{\substack{k=1 \\ k \neq m}}^{M} \alpha_k^{\mathrm{D}} s_k^{\mathrm{D}}(t) * c_{n(k)}^{\mathrm{D}}(-t). \tag{5.33c}$$

The following threshold detection (Fig. 5.6) yields $s_{n(m)}^{\mathrm{D}}(t)$. Communication is naturally successful when the detected downlink signal is identical to the transmitted uplink signal, i.e. $s_{n(m)}^{\mathrm{D}}(t) = s_m^{\mathrm{D}}(t) = s_m^{\mathrm{U}}(t)$.

5.2.3 System Characterization

This section characterizes the proposed time-reversal routing DCMA system in terms of MAI, signal to interference ratio (SIR) and bit error probability (BEP) for the case of On-Off Keying (OOK) modulation and Chebyshev dispersion coding. Note that, since uplink and downlink signals are described by mathematical expressions, Eqs. (5.31) and (5.33), of the same form, we shall consider here only the uplink case, the downlink and overall transmission being immediately deducible from it.

Modulation and Coding

Assuming OOK modulation, the transmitted signal is the pulse train

$$s_m^{\mathrm{U}}(t) = \sum_{\ell} d_{m\ell}^{\mathrm{U}} \delta(t - \ell T_{\mathrm{b}} - t_m^{\mathrm{U}}), \tag{5.34}$$

where $d_{m\ell}^{\mathrm{U}} = 1$ or 0 is the ℓ^{th} base-band bit, $\delta(\cdot)$ is the Dirac function, T_{b} is bit period and t_m^{U} is a random time offset.

Following Sec. 4.3, we choose odd Chebyshev dispersion coding $[\tau_m^{\mathrm{U}}(\omega)]$ for $\mathrm{AP}_m^{\mathrm{U}}$, $\forall\, m$, corresponding to

$$\tau_m^{\mathrm{U}}(\omega) = \tau_0 + \frac{\Delta\tau}{2} T_{i(m)} \left(\frac{\omega - \omega_0}{\Delta\omega/2} \right), \tag{5.35}$$

where $\Delta\tau$ is group delay swing over the band $\Delta\omega$, $T_{i(m)}$ is $i(m)^{\mathrm{th}}$ order Chebyshev polynomial of the first kind, and where we define $T_{-i(m)} = -T_{i(m)}$ for $i(m) > 0$. The code set of the M uplink access points may then be written

$$\mathbf{C} = \{i(1), \ldots, i(m), \ldots, i(M)\},\ i(m) \text{ odd and } i(m) \geq 3. \tag{5.36}$$

In the forthcoming computations, we consider the CM3 type (4–10 m NLOS) indoor multipath channel [134] for $w_m^{\mathrm{U}}(t)$.

MAI Probability Density Function

In Sec. 5.1.2, we have shown that in a LOS wireless channel, the MAI corresponding to all-odd Chebyshev dispersion coding (5.36) follows a normal distribution. We shall show here that the same is true for NLOS.

Figure 5.7 plots uplink simulation results of an $M = 5$ TR-DCMA system for three different bit periods (T_{b}) in the worst-case interference scenario where all the transmitters continuously send the bit '1'. As expected, the interference (MAI) floor $[x_m^{\mathrm{U}}(t)]$ decreases with increasing T_{b} due to decreasing MAI interference. The probability density function (PDF) of $x_m^{\mathrm{U}}(t)$ are found (third column in the figure) to closely follow the normal distribution PDF

$$\mathrm{PDF}(x_m^{\mathrm{U}}) = \frac{1}{\sqrt{2\pi\sigma^2}} \exp\left[-\frac{(x_m^{\mathrm{U}} - \mu_m)^2}{2\sigma_m^2} \right], \tag{5.37a}$$

where μ_m is the mean of x_m^{U}, which is 0 due to the symmetric-bipolar nature of MAI, and

σ_m^2 is the variance,

$$\sigma_m^2 = \frac{1}{T_\mathrm{b}} \int_{T_\mathrm{b}} \left| x_m^\mathrm{U}(t) - \mu_m^\mathrm{U} \right|^2 \, dt = \frac{1}{T_\mathrm{b}} \int_{T_\mathrm{b}} \left| x_m^\mathrm{U}(t) \right|^2 \, dt, \tag{5.37b}$$

which is equivalent to the MAI average power over one bit. In a realistic scenario, where bits '1' and '0' alternate in the wireless channel, the interference would naturally be less, leading to smaller σ_m^2 values. In the forthcoming results, the same worst-case scenario has been assumed for the PDF, and practical results would then be better than what will be shown.

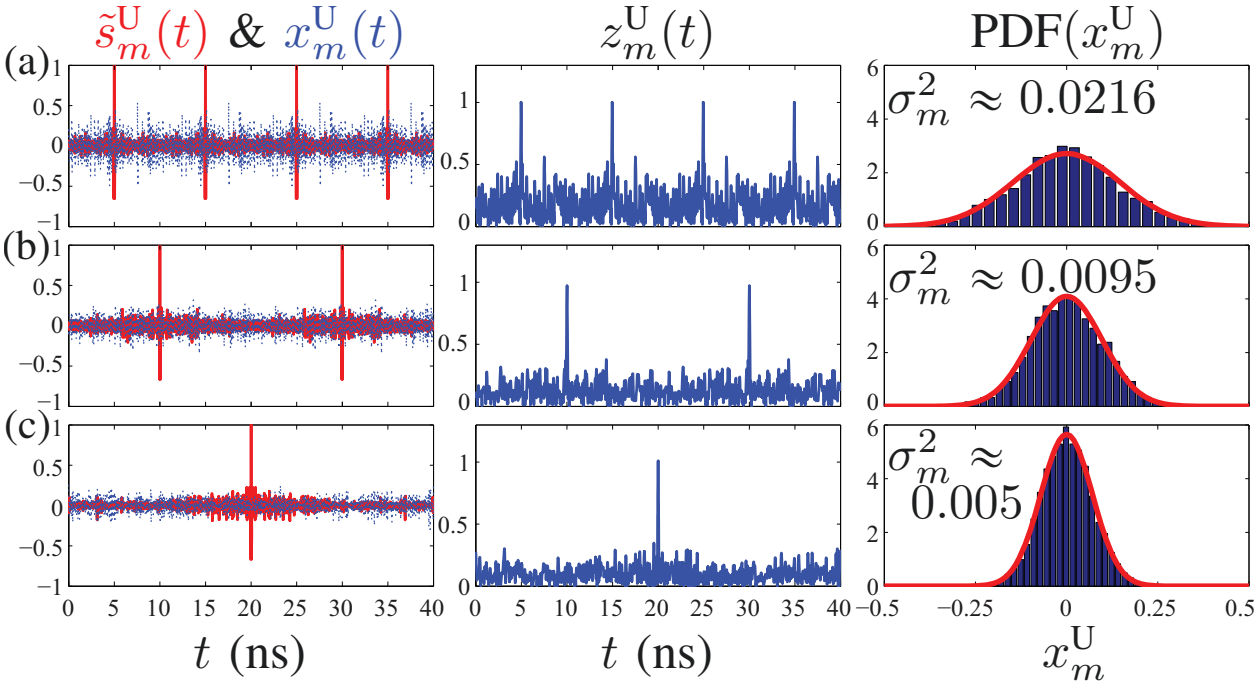

Figure 5.7 Uplink simulation results in the worst-case interference scenario, where $d_{m\ell}^\mathrm{U} = 1$, $\forall m, \ell$, in (5.34) for $M = 5$ TR-DCMA with $\Delta f = 10$ GHz, $\Delta\tau = 10$ ns, coding $\mathbf{C} = \{3, -3, 5, -5, 7\}$ and identical energy $\alpha_m^\mathrm{U} = \text{const.}$ in (5.30). All the results are normalized as follows : for each m, α_m^U is set such that $|\tilde{s}_m^\mathrm{U}(t)|_\mathrm{max} = 1$ in (5.31b) and $x_m^\mathrm{U}(t)$ is divided by that α_m^U in (5.31c). First column : desired signal, $\tilde{s}_m^\mathrm{U}(t)$ (red-solid curve), and MAI, $x_m^\mathrm{U}(t)$ (blue-dotted curve), computed using (5.31b) and (5.31c), respectively. Second column : total encoded signal, $z_m^\mathrm{U}(t)$, computed using (5.31a). Third column : probability density function (PDF) of the MAI values, obtained by counting the occurrences of the sample values (blue stripes) and compared against the normal distribution PDF (red curve) [Eq. (5.37a) with mean $\mu_m = 0$, $\forall m$, and variance σ_m^2 in (5.37b). (a) $T_\mathrm{b} = \Delta\tau$, (b) $T_\mathrm{b} = 2\Delta\tau$, and (c) $T_\mathrm{b} = 4\Delta\tau$ (L. Zou, et al, [18], ArXiv : `https://arxiv.org/abs/1709.08085`).

Statistical and Analytical SIR

The SIR may be statistically found by taking the ratio of $|\tilde{s}_m^{\mathrm{U}}(t)|_{\max}$ to the MAI variance given by (5.37b), using the normalization indicated in the caption of Fig. 5.7, which yields

$$\mathrm{SIR}_m^{\mathrm{U}\prime} = \frac{1}{\sigma_m^2}. \tag{5.38}$$

Similar (5.16), This quantity can also be obtained analytically as

$$\mathrm{SIR}_m^{\mathrm{U}} = \frac{2\Delta f T_{\mathrm{b}}}{\overline{\alpha_m^2}(N-1)}, \tag{5.39a}$$

where

$$\overline{\alpha_m^2} = \frac{1}{N-1}\sum_{\substack{k=1\\k\neq m}}^{M}\left(\frac{\alpha_k^{\mathrm{U}}}{\alpha_m^{\mathrm{U}}}\right)^2 \tag{5.39b}$$

is the mean of the normalized MAI energies [3].

Figure 5.8 compares the analytical [Eq. (5.39)] and statistical [Eq. (5.38)] SIRs. Good agreement is observed, with deviation smaller than 2 dB. Therefore, we will directly use (5.39) to avoid statistical testing over many bits in the remainder of the section.

The downlink MAI also follows normal distribution, and the corresponding $\mathrm{SIR}_{n(m)}^{\mathrm{D}}$ is also approximated by (5.39) with α_k^{U} and α_m^{U} replaced by $\alpha_{n(k)}^{\mathrm{D}}$ and $\alpha_{n(m)}^{\mathrm{D}}$.

Overall BEP Performance

According to (5.22), the BEP for MAI with normal distribution is found is

$$\mathrm{BEP}_m^{\mathrm{U}} = \frac{1}{\sqrt{2\pi}}\int_{\sqrt{\mathrm{SIR}_m^{\mathrm{U}}/2}}^{\infty}\exp\left(-\frac{x^2}{2}\right)dx, \tag{5.40}$$

where $\mathrm{SIR}_m^{\mathrm{U}}$ is given by (5.39). The downlink $\mathrm{BEP}_{n(m)}^{\mathrm{D}}$ is found by replacing $\mathrm{SIR}_m^{\mathrm{U}}$ in (5.40) with $\mathrm{SIR}_{n(m)}^{\mathrm{D}}$.

Communication is overall successful if both the uplink and downlink transmissions are suc-

3. In (5.39b), $k = m$ is excluded from the sum as it corresponds to the signal.

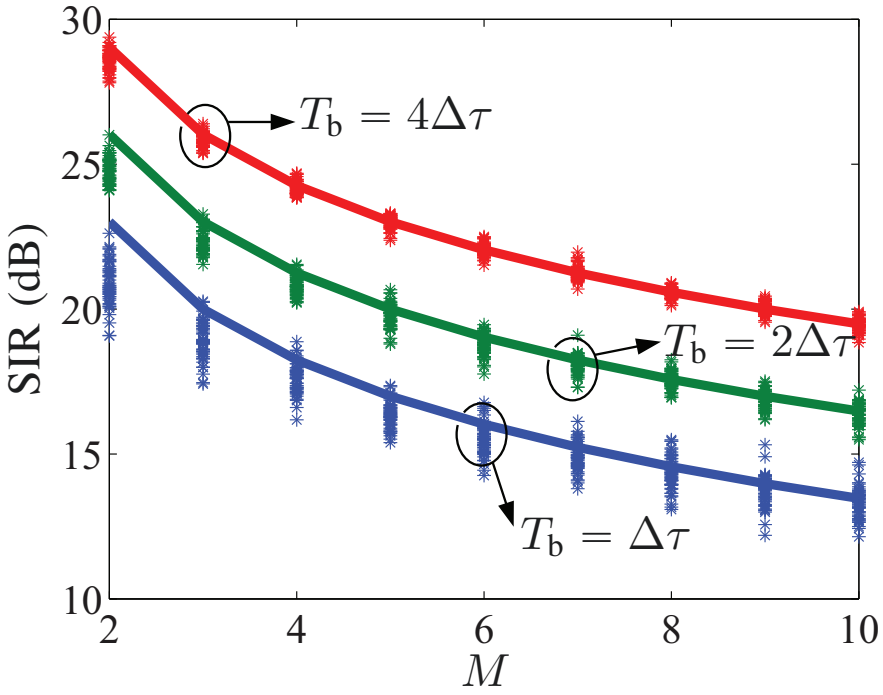

Figure 5.8 SIR versus the number of transmitters (M) with $\Delta f = 10$ GHz, $\Delta\tau = 10$ ns, coding $\mathbf{C} = \{3, -3, 5, -5, \ldots\}$, identical energy ($\alpha_m^{\mathrm{U}} = \text{const.}\ \forall\, m$) in (5.30), and different T_{b}. Solid curves : Eq. (5.39), '*' markers : Eq. (5.38) with (5.37b) and (5.31c) for 500 bits (L. Zou, et al, [18], ArXiv : `https://arxiv.org/abs/1709.08085`).

cessful, corresponding to the overall BEP

$$\begin{aligned} \mathrm{BEP}_m &= 1 - \left(1 - \mathrm{BEP}_m^{\mathrm{U}}\right)\left(1 - \mathrm{BEP}_{n(m)}^{\mathrm{D}}\right) \\ &= \mathrm{BEP}_m^{\mathrm{U}} + \mathrm{BEP}_{n(m)}^{\mathrm{D}} - \mathrm{BEP}_m^{\mathrm{U}}\mathrm{BEP}_{n(m)}^{\mathrm{D}} \\ &\approx \mathrm{BEP}_m^{\mathrm{U}} + \mathrm{BEP}_{n(m)}^{\mathrm{D}}. \end{aligned} \tag{5.41}$$

Figure 5.9 plots the BEP (same for all m's) of the TR-DCMA system for APs with identical energy, and compared against that of the corresponding DCMA system without time-reversal routing. Due to the two-step (uplink and downlink) transmission phases, the BEP is approximately doubled, or degraded by an order of $\log_{10} 2 \approx 0.3$. This graph shows that the BEP is not affect by the dynamic TR routing.

5.3 Summary

This chapter characterize DCMA system in terms of bit error probability (BEP) numerically. The characterization was first performed for LOS wireless channel, without additional

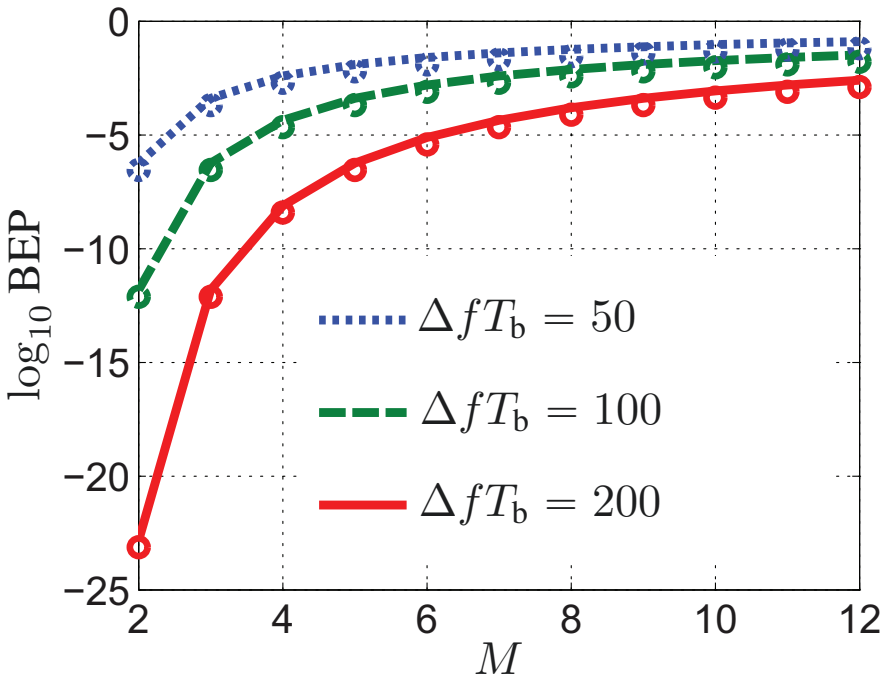

Figure 5.9 BEP versus the number of simultaneous communication links (M) in the TR-DCMA system in Fig. 5.6 for APs with identical energy ($\alpha_m^{\mathrm{U}} = \alpha_{n(m)}^{\mathrm{D}} = \text{const.}\ \forall\, m$), computed using (5.41) (curves), and compared against the BEP of the corresponding DCMA system without time-reversal routing (circles), for different $\Delta f T_{\mathrm{b}}$ values (L. Zou, et al, [18], ArXiv : `https://arxiv.org/abs/1709.08085`).

dispersion. The MAI statistical distribution was found, and the SIR was computed both analytically and statistically, the BEP corresponding to a normal distribution is given by the Q function, with lower integration bound being a function of the SIR. Thus, the overall BEP is a function of SIR, enhancing SIR is critical for better BEP performance. Finally, the BEP was computed for two cases, 1) all interfered energies are equal to that of the desired signal energy, 2) the ratio of the desired signal energy to the interfered energy is enhanced by means, such as for instance beamforming. For the former case, the BEP is at the order of 10^{-7} for 6 users, while BEP below 10^{20} is essentially considered to be zero. For the latter case, the BEP is at the order of 10^{-7} even for 12 users, confirming the effectiveness of beamforming for SIR enhancement. Other SIR enhancement technique may include assigning orthogonal pulse shapes for different users, etc.

The system has some limitations. First, The routing scheme is fixed, because the group delay functions are fixed. The solution may be to use reconfigurable phaser presented in Chapter 3 to tune the group delay functions dynamically. Second, the characterization was initially performed only for LOS channel, which is dispersion-less. However, in practice, the channel

is NLOS, leading to additional dispersion, which can be compensated by using the reconfigurable phaser technologies. However, making the terminal coding phaser reconfigurable inevitably complicates the simple design. We therefore proposed to use time-reversal, as an efficient self-adaptive solution, to address the two aforementioned limitations, i.e. to achieve dynamic routing and to compensate NLOS dispersion, in one shot. We also performed characterization for such time-reversal based DCMA system for its MAI, SIR and BEP. It is worth mentioning that, for millimeter-wave communication, such as 5G, the NLOS dispersion may be neglected due to very weak multiple path components compared to the LOS component, and the channel may be approximated as LOS. In that case, the dynamic routing is still accomplished by time-reversal.

CHAPTER 6 CONCLUSION AND RECOMMENDATIONS

6.1 Conclusion

This thesis presents group delay engineering based R-ASP techniques and applications to wireless communications. The chapters corresponding to selected articles represent novel R-ASP concepts, components and systems.

Chapter 2 introduced the group delay engineering concept and figures of merit. Then, a practical example of group delay swing (dispersion) enhancement phaser using reflective resonator units was presented.

Chapter 3 first showed the amplitude unbalance issue related to passive phasers, and proposed the gain-loss equalization concept for perfectly all-pass amplitude, furthermore, demonstrated that tuning the equalized gain and loss controls the group delay function in real-time, leading to de-facto all-pass and group delay reconfigurable phaser. We systematically modeled, analyzed such phaser based on coupled-line coupler loaded by a gain/loss load, and experimentally demonstrated the prototype, in terms of group delay swing and profile reconfigurability, amplitude flatness, and noise figure, etc. Such reconfigurable phaser may find its R-ASP applications where real-time adaptivity to the dynamic environment is required.

Chapter 4 first introduced the concept of DCMA communication system, with complete mathematical description to the system. Then, the chapter presented Chebyshev polynomial group delay function set as an efficient multiple access coding scheme. Finally, we implemented a proof-of-concept DCMA system and demonstrated the data transmission experiment, hence showing the feasibility of this purely analog and real-time multiple access scheme for high-speed wireless communications. The system employed C-section phaser technology for its simple design and small size. Also presented in Chapter 4 in Sec. 4.4.1 is the UWB RF pulse generator based on a pair of step recovery diodes with pulse duration tunable by a single resistor. Such pulse generator may find wide applications in R-ASP, where phasers typically manipulate UWB impulse radio signal, and in other UWB radio systems with low cost and low complexity.

In Chapter 5, Sec. 5.1 first stochastically characterized DCMA for LOS wireless channel, in terms of MAI, SIR and BEP for different parameters, such as simultaneous users N, delay swing bandwidth product, etc. We have shown that the critical figure of merit is the Delay Swing Bandwidth Product (DSBP), and that SIR and spectral efficiency are linearly and inversely proportional to the DSBP, respectively. One may consequently use directive an-

tennas to satisfy simultaneously stringent SIR and spectral efficiency specifications. Then, Sec. 5.2 proposed a time-reversal routing scheme for dynamically switching communication links and compensating the NLOS wireless channel dispersion. The system incorporates a time reversal router or base station which takes account for the complexity of routing and compensation processing, while maintains the advantages of DCMA, such as low-complexity and low-latency for access point transceiver. All in all, being a real-time analog signal processing technology, DCMA exhibits a number of advantages over DSP-based technologies, including the absence of latency (with negligible delay, only related to electromagnetic wave propagation), lower complexity, lower cost and lower power consumption, and higher scalability to millimeter-wave or terahertz frequencies for future high-speed communications.

6.2 Miscellaneous Suggestions for Future Work

Here are some suggestions for the future works.
- "Phasenna", combination of antenna and phaser.
- Methods for breaking the limit on time-bandwidth product constant of phasers.
- More sophisticated dispersion coding functions (group delay functions) for DCMA BEP improvement.
- Real-time spread spectrum wireless communication system to accommodate modulation schemes with higher spectrum efficiency.

6.2.1 "Phasenna" – Combination of Antenna and Phaser

The concept of "phasenna", which essentially combines the antenna and phaser functions compactly in one component, was first proposed by demonstrating group delay engineering using a modified log-periodic diple array (LPDA) with rearranged dipoles [135]. Such component may find its applications in low-cost and compact wireless communication systems. However, using such modified LPDA can only engineer negative-slope group delay, because the dipoles here must be placed increasingly large from the feed to avoid harmonic radiation. A group delay engineering method using phase array antenna has been proposed in [136]. The method yields synthesized phase response with strong oscillation around the specified phase, thus the group delay, being the derivative of phase, would oscillate even stronger than the phase. Therefore, a different approach has to be investigated for effectively synthesizing the group delay of radiation wave.

6.2.2 Breaking the Limit on Time-Bandwidth Product Constant of Phasers

We have shown in Chapter 5 that the delay swing bandwidth product (DSBP) is the critical figure of merit, which is positively related to time bandwidth product ($\mathcal{P}$) as given by (2.4). $\mathcal{P}$ is constant for a given phaser [6, 44], breaking the constant limit would be challenging. Recently, K. L. Tsakmakidis, et al. have shown that non-reciprocal coupling of a resonator breaks the time bandwidth product constant [137], which may lead to new type of phaser with enhanced $\mathcal{P}$ capability and thus is worth investigating.

6.2.3 Dispersion Codes for Improved DCMA Performance

In Chapter 5, we have shown that, given different dispersion codes (group delay functions), one gets different MAI statistical distributions, such as for instance, the linear dispersion coding leads to the arcsine distribution, and higher order Chebyshev coding leads to the normal distribution, as shown in Fig. 5.1(c). A specific MAI distribution further yields corresponding BEP performances. For example, the MAI with normal distribution leads to corresponding BEP given by (5.22). Thus, the dispersion code selection is critical to DCMA BEP performance. To find the optimal coding scheme, one may resort to solving the inverse problem. The inverse problem may be defined as finding the group delay function set corresponding to the given MAI distribution. Such inverse problem is interesting in that it allows one to first determine the MAI distribution for possibly best BEP performance, and then to generate the corresponding group delay functions leading to that MAI distribution.

6.2.4 Real-Time Spread Spectrum Wireless Communication System

Despite the simplicity and low-latency, the real-time DCMA system has its drawbacks. It only manipulates UWB impulse signal, whose modulation schemes are typically constrained to on-off keying (OOK), binary phase shift keying (BPSK), or pulse position modulation (PPM), and thus limiting the spectrum efficiency and data capacity. On the other hand, more spectrum-efficient modulation schemes, such as 64QAM, OFDM, etc, are not seen being applied to impulse signal.

Spread spectrum multiple access (SSMA) techniques have been efficiently applied in wireless communication and able to accommodate high spectrum-efficient modulation schemes. However, conventional SSMA is not done in real-time fashion, thus limiting its speed. We will next propose a real-time SSMA method, using space-time metamaterial [138], for wireless communications.

6.3 Proposal for Real-Time Spread Spectrum Multiple Access

There exists duality between the DCMA and SSMA system, as compared in Fig. 6.1. A DCMA system spreads and re-compresses narrow time duration signal in time domain, while keeping its frequency contents (bandwidth) unaltered [Fig. 6.1(a)]. In contrast, an SS system spreads and re-compresses narrow bandwidth signal in frequency domain, while keeping time duration unaltered [Fig. 6.1(b)].

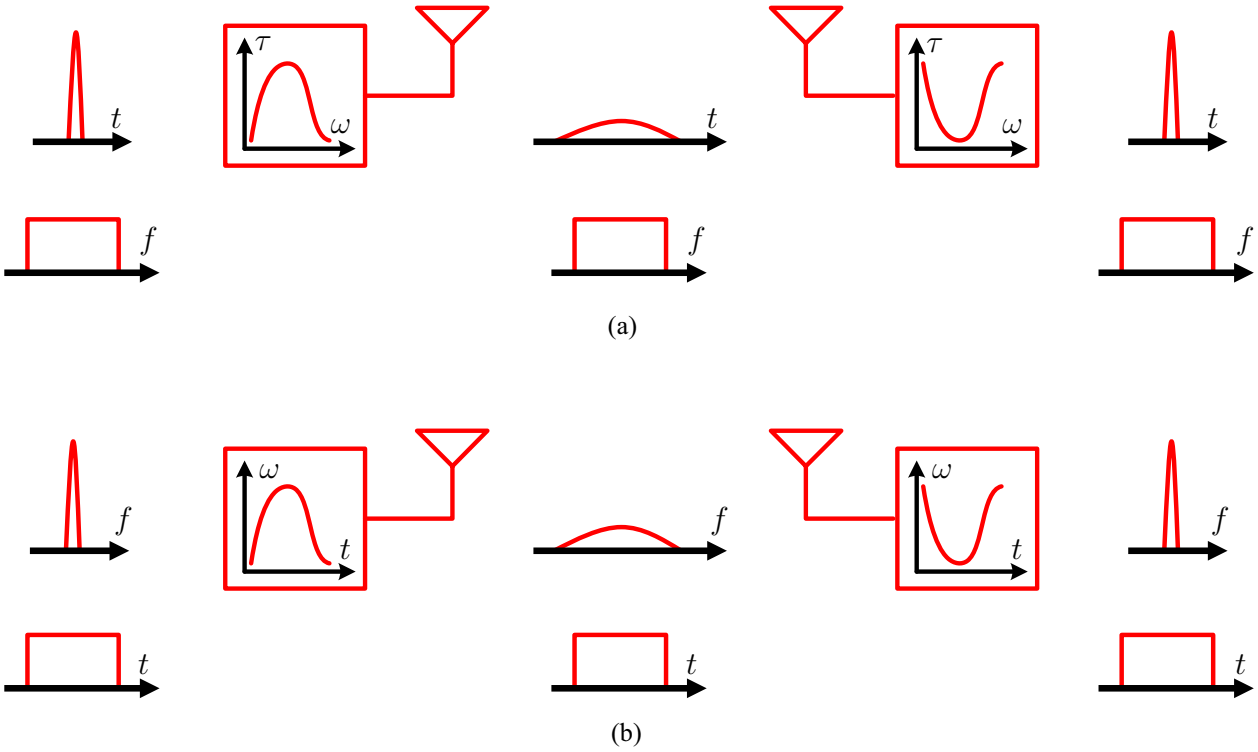

Figure 6.1 Comparison of DCMA and spread spectrum (SS) system. (a) DCMA system. (b) SS system.

Conventionally, spread spectrum coding, such as for instance frequency hoping, may be done with complex frequency synthesizer and mixer [129]. Figure 6.2 shows conventional approach for spread spectrum coding. The input, here for illustrative purpose, is narrowband QPSK modulated signal $s_{\mathrm{i}}(t)$ with carrier frequency ω_0 and symbol duration T. The spread spectrum code $\omega_{\mathrm{code}}(t)$, with frequency variation $\Delta\omega$ over time T, may be generated by a frequency synthesizer, which is not explicitly shown here. The mixer output is the product of $s_{\mathrm{i}}(t)$ and a frequency varying $[\omega_{\mathrm{code}}(t)]$ signal, leading to a double sideband signal with bandwidth of each sideband broadened by $\Delta\omega$. For high speed communication, i.e. T is small, a fast frequency

synthesizer is required. A digital frequency synthesizer exhibits limited output frequency, narrow bandwidth, and power consumption that scales with the frequency [22]. An analog frequency synthesizer, typically based on phase locked loop (PLL), is constrained by the trade-off between jitter (phase noise) and settling time (speed) due to PLL feedback [139]. Moreover, the fastest settling time is typically in the order of microsecond, and hence limiting the achievable communication speed (symbol rate). In any cases, conventional spread spectrum is not based on real-time processing.

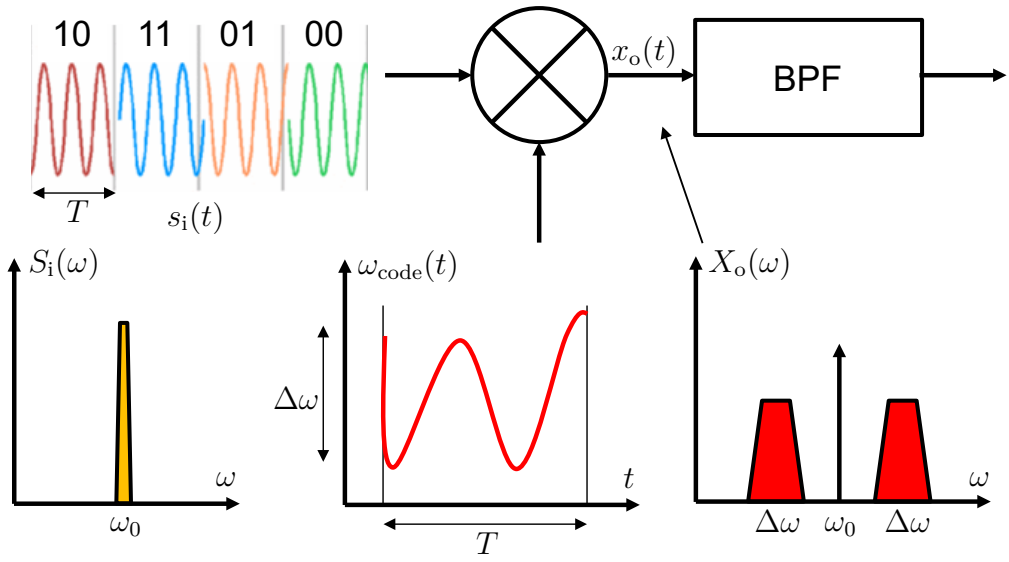

Figure 6.2 Diagrammatic illustration of conventional spread spectrum coding using mixer.

Recently, the advancement of space-time (ST) metamaterial, whose material properties vary with space and time, enables unprecedented control of electromagnetic wave properties, including control of wave temporal frequency [138], in real time. Figure 6.3 shows a conceptual ST transmission line for both frequency synthesizing and mixing. For these purposes, the ST line has a moving PEC wall (short end), whose position z as function of time t is tuned dynamically by some mechanism. We shall now explain how the frequency is synthesized without mixer and conventional synthesizer.

Suppose we want to synthesize a frequency function, which is the time derivative of the phase of the ST system output signal $x_o(t) = \cos[\omega_0 t + \phi(t)]$, as

$$\omega(t) = \omega_0 + \frac{\partial \phi}{\partial t}, \tag{6.1}$$

where ω_0 is the input frequency, $\phi(t)$ is the phase of the output signal. Also the output frequency variation is attributed to the Doppler frequency shift caused by the moving PEC

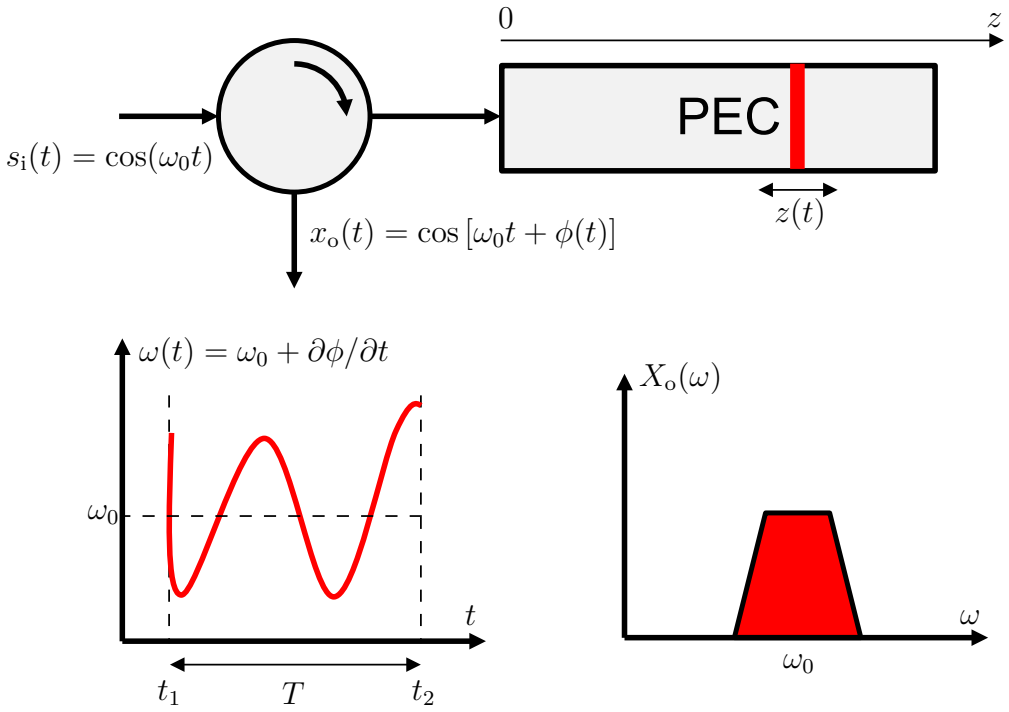

Figure 6.3 Conceptual ST transmission line for high speed frequency synthesizing and mixing.

wall, as

$$\omega(t) = \omega_0 \left[1 - \frac{v(t)}{c/\sqrt{\epsilon_{\mathrm{r,eff}}}}\right] = \omega_0 \left[1 - \frac{z'(t)\sqrt{\epsilon_{\mathrm{r,eff}}}}{c}\right], \tag{6.2}$$

where c is the speed of light, $\epsilon_{\mathrm{r,eff}}$ is effective permittivity of the transmission line, $v(t) = z'(t) = dz/dt$ is the speed of the PEC wall. When the PEC wall moves away from the input of the line (in $+z$ direction), i.e. $v(t) > 0$, the synthesized frequency $\omega(t) < \omega_0$, otherwise $\omega(t) > \omega_0$ for the wall moving in $-z$ direction. The PEC wall moving back-and-forth yields the frequency variation as function of time, $\omega(t)$. One may next find $z(t)$ corresponding to the desired $\omega(t)$. Note that by rearranging (6.2), one finds

$$z'(t) = \frac{c}{\sqrt{\epsilon_{\mathrm{r,eff}}}} \left[1 - \frac{\omega(t)}{\omega_0}\right]. \tag{6.3}$$

Therefore, $z(t)$ is found by integral

$$z(t) = z(t_1) + \frac{c}{\sqrt{\epsilon_{\mathrm{r,eff}}}} \int_{t_1}^{t} \left[1 - \frac{\omega(\tau)}{\omega_0}\right] d\tau, \quad t \in [t_1, t_2], \tag{6.4}$$

where t_1 and $t_2 = t_1 + T$ are the beginning and ending time of one symbol with duration T, and $z(t_1)$ is the PEC wall position at t_1.

The position tuning mechanism may be achieved by using an array of shunt transistor switches along a conventional transmission line. At any specific time instant t, one of the switches at $z(t)$ is closed, providing a very low resistance to the ground and thus mimicking a PEC wall moving along the line.

The advantages of the system in Fig. 6.3 compared to that in Fig. 6.2 is : 1) much simpler and cheaper design without frequency synthesizer and mixer, 2) faster symbol rate due to the elimination of PLL with microsecond-order settling time. Thus, the ST metamaterial technique allows real-time spread spectrum coding, which exhibits capabilities of real-time low-latency processing and of accommodating high spectrum-efficient modulation schemes.

REFERENCES

[1] L. Zou and C. Caloz, "High-resolution transmission-type (TT) dispersive delay structure (DDS) based on reflection-type (RT) elements," in *Proc. IEEE Int'l Microw. Symp.*, Tampa, FL. U.S., Jun. 2014.

[2] J. S. Lee, C. Nguyen, and T. Scullion, "New uniplanar subnanosecond monocycle pulse generator and transformer for time-domain microwave applications," *IEEE Trans. Microw. Theory Techn.*, vol. 49, no. 6, pp. 1126 – 1129, Jun. 2001.

[3] T. Xia, A. S. Venkatachalam, and D. Huston, "A high-performance low-ringing ultra-wideband monocycle pulse generator," *IEEE Trans. Instrum. Meas.*, vol. 61, no. 1, pp. 261 – 266, Jan. 2012.

[4] L. Zou, S. Gupta, and C. Caloz, "A simple picosecond pulse generator based on a pair of step recovery diodes," *IEEE Microw. Wireless Compon. Lett.*, vol. 27, no. 5, pp. 467 – 469, May 2017.

[5] B. Nikfal, D. Badiere, M. Repeta, B. Deforge, S. Gupta, and C. Caloz, "Distortion-less real-time spectrum sniffing based on a stepped group-delay phaser," *IEEE Microw. Wireless Compon. Lett.*, vol. 22, no. 11, pp. 601 – 603, Nov. 2012.

[6] C. Caloz, S. Gupta, Q. Zhang, and B. Nikfal, "Analog signal processing : A possible alternative or complement to dominantly digital radio schemes," *IEEE Microw. Mag.*, vol. 14, no. 6, pp. 87 – 103, Sep. 2013.

[7] C. Campbell, *Surface Acoustic Wave Devices and Their Signal Processing Applications*. New York : Academic Press, 1989.

[8] C. Caloz and T. Itoh, *Electromagnetic metamaterials, transmission line theory and microwave applications*. Wiley-IEEE Press, 2006.

[9] K. O. Hill and G. Meltz, "Fiber Bragg grating technology fundamentals and overview," *J. Lightw. Technol.*, vol. 15, no. 8, pp. 1263 – 1276, Aug. 1997.

[10] M. A. G. Laso, T. Lopetegi, M. J. Erro, D. Benito, M. J. Garde, M. A. Muriel, M. Sorolla, and M. Guglielmi, "Real-time spectrum analysis in microstrip technology," *IEEE Trans. Microw. Theory Techn.*, vol. 51, no. 3, pp. 705 – 717, Mar. 2003.

[11] Q. Zhang, D. L. Sounas, and C. Caloz, "Synthesis of cross-coupled reduced-order dispersive delay structures (DDS) with arbitrary group delay and controlled magnitude," *IEEE Trans. Microw. Theory Techn.*, vol. 61, no. 3, pp. 1043 – 1052, Mar. 2013.

[12] S. Gupta, A. Parsa, E. Perret, R. V. Snyder, R. J. Wenzel, and C. Caloz, "Group-delay engineered noncommensurate transmission line all-pass network for analog signal processing," *IEEE Trans. Microw. Theory Techn.*, vol. 58, no. 9, pp. 2392 – 2407, Sep. 2010.

[13] O. Schwelb, "Transmission, group delay, and dispersion in single-ring optical resonators and add/drop filters - a tutorial overview," *J. Lightw. Technol.*, vol. 22, no. 5, pp. 1380 – 1394, May 2004.

[14] Q. Zhang, S. Gupta, and C. Caloz, "Synthesis of narrowband reflection-type phasers with arbitrary prescribed group delay," *IEEE Trans. Microw. Theory Techn.*, vol. 60, no. 8, pp. 2394 – 2402, Aug. 2012.

[15] L. Zou, S. Gupta, and C. Caloz, "Loss-gain equalized reconfigurable c-section analog signal processor," *IEEE Trans. Microw. Theory Techn.*, vol. 65, no. 2, pp. 555 – 564, Feb. 2017.

[16] ——, "Real-time dispersion code multiple access (DCMA) for high-speed wireless communications," *IEEE Trans. Wireless Commun.*, Oct. 2017. [Online]. Available : http://ieeexplore.ieee.org/document/8086172/

[17] S. Gezici, H. Kobayashi, H. V. Poor, and A. F. Molisch, "Performance evaluation of impulse radio UWB systems with pulse-based polarity randomization," *IEEE Trans. Signal Process.*, vol. 53, no. 7, pp. 2537–2549, Jul. 2005.

[18] L. Zou and C. Caloz, "Time-reversal routing for dispersion code multiple access (dcma) communications," *arXiv :1709.08085*, 2017. [Online]. Available : https://arxiv.org/abs/1709.08085

[19] B. P. Lathi, *Modern Digital and Analog Communication Systems 3th Ed.* New York : Oxford University Press, 1998.

[20] Q. C. Li, H. Niu, A. T. Papathanassiou, and G. Wu, "5g network capacity : Key elements and technologies," *IEEE Veh. Technol. Mag.*, vol. 9, no. 1, pp. 71–78, Mar. 2014.

[21] A. Osseiran, V. Braun, T. Hidekazu, P. Marsch, H. Schotten, H. Tullberg, M. A. Uusitalo, and M. Schellmann, "The foundation of the mobile and wireless communications system for 2020 and beyond : Challenges, enablers and technology solutions," in *IEEE Veh. Technol. Conf. (VTC)*, Dresden, Germany, Jun. 2013.

[22] B. Murmann, "Adc performance survey 1997-2017 [online]. available : http://web.stanford.edu/~murmann/adcsurvey.html," Tech. Rep.

[23] B. E. A. Saleh and M. C. Teich, *Fundamentals of Photonics 2nd Ed.* Hoboken, NJ : John Wiley, 2007.

[24] J. Azaña, "Ultrafast analog all-optical signal processors based on fiber-grating devices," *IEEE Photon. J.*, vol. 2, no. 3, pp. 359 – 386, Jun. 2010.

[25] W. Liu, M. Li, R. S. Guzzon, E. J. Norberg, J. S. Parker, M. Lu, L. A. Coldren, and J. Yao, "A fully reconfigurable photonic integrated signal processor," *Nature Photonics*, vol. 10, no. 2, pp. 190–195, Feb. 2016.

[26] J. Azaña and M. A. Muriel, "Real-time optical spectrum analysis based on the time-space duality in chirped fiber gratings," *IEEE J. Quantum Electron.*, vol. 36, no. 5, pp. 517–526, May 2000.

[27] N. K. Berger, B. Levit, S. Atkins, and B. Fischer, "Time-lens-based spectral analysis of optical pulses by electrooptic phase modulation," *Electron. Lett.*, vol. 36, no. 19, p. 1644–1646, Sep. 2000.

[28] K. Goda and B. Jalali, "Dispersive fourier transformation for fast continuous single-shot measurements," *Nature Photonics*, vol. 7, no. 1, pp. 102–112, Jan. 2013.

[29] A. M. Fard, S. Gupta, and B. Jalali, "Photonic time-stretch digitizer and its extension to real-time spectroscopy and imaging," *Laser & Photonics Reviews*, vol. 7, no. 2, pp. 207–263, 2013.

[30] R. Slavík, Y. Park, N. Ayotte, S. Doucet, T.-J. Ahn, S. LaRochelle, and J. Azaña, "Photonic temporal integrator for all-optical computing," *Opt. Express*, vol. 16, no. 22, pp. 18 202–18 214, Oct. 2008.

[31] L. M. Rivas, S. Boudreau, Y. Park, R. Slavík, S. LaRochelle, A. Carballar, and J. Azaña, "Experimental demonstration of ultrafast all-fiber high-order photonic temporal differentiators," *Opt. Lett.*, vol. 34, no. 12, pp. 1792–1794, Jun 2009.

[32] J. Zhang and J. Yao, "Photonic-assisted microwave temporal convolution," *J. Lightw. Technol.*, vol. 34, no. 20, pp. 4652–4657, Oct 2016.

[33] L. Zhuang, M. R. Khan, W. Beeker, A. Leinse, R. Heideman, and C. Roeloffzen, "Novel microwave photonic fractional hilbert transformer using a ring resonator-based optical all-pass filter," *Opt. Express*, vol. 20, no. 24, pp. 26 499–26 510, Nov 2012.

[34] H. Shahoei, P. Dumais, and J. Yao, "Continuously tunable photonic fractional hilbert transformer using a high-contrast germanium-doped silica-on-silicon microring resonator," *Opt. Lett.*, vol. 39, no. 9, pp. 2778–2781, May 2014.

[35] H. P. Sardesai, C.-C. Chang, and A. M. Weiner, "A femtosecond code-division multiple-access communication system test bed," *J. Lightw. Technol.*, vol. 16, no. 11, p. 1953, Nov 1998.

[36] P. R. Prucnal, *Optical Code Division Multiple Access : Fundamentals and Applications*. Boca Raton, FL. : CRC Press, Taylor & Francis Group, 2006.

[37] C. H. Lee, *Microwave Photonics, 2nd Ed.* Boca Raton, FL. : CRC Press, Taylor & Francis Group, 2013.

[38] R. A. Minasian, E. H. W. Chan, and X. Yi, "Microwave photonic signal processing," *Opt. Express*, vol. 21, no. 19, pp. 22 918–22 936, Sep 2013.

[39] R. Minasian, "Photonic signal processing of microwave signals," *IEEE Trans. Microw. Theory Techn.*, vol. 54, no. 2, pp. 832 – 846, Feb. 2006.

[40] J. Zhang and J. Yao, "Broadband microwave signal processing based on photonic dispersive delay lines," *IEEE Trans. Microw. Theory Techn.*, vol. 65, no. 5, pp. 1891–1903, May 2017.

[41] ——, "Photonic-assisted microwave temporal convolution," *J. Lightw. Technol.*, vol. 34, no. 20, pp. 4652–4657, Oct 2016.

[42] ——, "Broadband and precise microwave time reversal using a single linearly chirped fiber bragg grating," *IEEE Trans. Microw. Theory Techn.*, vol. 63, no. 7, pp. 2166–2172, July 2015.

[43] J. Yao, "Photonic generation of microwave arbitrary waveforms," *Optics Communications*, vol. 284, no. 15, pp. 3723 – 3736, 2011.

[44] S. Gupta, Q. Zhang, L. Zou, L. Jiang, and C. Caloz, "Generalized coupled-line all-pass phasers," *IEEE Trans. Microw. Theory Techn.*, vol. 63, no. 3, pp. 1 – 12, Mar. 2015.

[45] J. D. Schwartz, R. Abhari, D. V. Plant, and J. Azaña, "Design and analysis of 1-d uniform and chirped electromagnetic bandgap structures in substrate-integrated waveguides," *IEEE Trans. Microw. Theory Techn.*, vol. 58, no. 7, pp. 1858–1866, July 2010.

[46] M. A. G. Laso, T. Lopetegi, M. J. Erro, D. Benito, M. J. Garde, M. A. Muriel, A. Sorolla, and M. Guglielmi, "Chirped delay lines in microstrip technology," *IEEE Microw. Wireless Compon. Lett.*, vol. 11, no. 12, pp. 486–488, Dec 2001.

[47] A. Lujambio, I. Arnedo, M. Chudzik, I. Arregui, T. Lopetegi, and M. A. G. Laso, "Dispersive delay line with effective transmission-type operation in coupled-line technology," *IEEE Microw. Wireless Compon. Lett.*, vol. 21, no. 9, pp. 459–461, Sept 2011.

[48] S. Gupta, D. L. Sounas, H. V. Nguyen, Q. Zhang, and C. Caloz, "CRLH-CRLH C-section dispersive delay structures with enhanced group-delay swing for higher analog signal processing resolution," *IEEE Trans. Microw. Theory Techn.*, vol. 60, no. 12, pp. 3939 – 3949, Dec. 2012.

[49] E. G. Cristal, "Analysis and exact synthesis of cascaded commensurate transmission-line C-section all-pass networks," *IEEE Trans. Microw. Theory Techn.*, vol. 14, no. 6, pp. 285 – 291, Jun. 1966.

[50] ——, "Theory and design of transmission line all-pass equalizers," *IEEE Trans. Microw. Theory Techn.*, vol. 17, no. 1, pp. 28 – 38, Jan. 1969.

[51] Q. Zhang, S. Gupta, and C. Caloz, "Synthesis of broadband phasers formed by commensurate c- and d-sections," *Int. J. RF Microw. Comput. Aided Eng.*, vol. 24, no. 3, pp. 322 – 331, May 2014.

[52] M. K. Mandal, D. Deslandes, and K. Wu, "Complementary microstrip-slotline stub configuration for group delay engineering," *IEEE Microw. Wireless Compon. Lett.*, vol. 22, no. 8, pp. 388 – 390, Aug. 2012.

[53] Y. W. Chang, C. W. Hsue, J. Y. Wen, and Y. T. Yeh, "Dispersive delay line with large group delay using deformed open stub and its complementary slot line," *IEEE Microw. Wireless Compon. Lett.*, vol. 26, no. 2, pp. 122–124, Feb 2016.

[54] E. Abdo-Sánchez, J. E. Page, T. M. Martín-Guerrero, J. Esteban, and C. Camacho-Peñalos, "Planar broadband slot radiating element based on microstrip-slot coupling for series-fed arrays," *IEEE Trans. Antennas Propag.*, vol. 60, no. 12, pp. 6037 – 6042, Dec. 2012.

[55] C.-W. Hsue and Y.-W. Chang, "Dispersive delay lines using microstrip technology," *The Journal of Engineering*, October 2016.

[56] K. Achouri, A. Yahyaoui, S. Gupta, H. Rmili, and C. Caloz, "Dielectric resonator metasurface for dispersion engineering," *IEEE Trans. Antennas Propag.*, vol. 65, no. 2, pp. 673–680, Feb 2017.

[57] S. Gupta, B. A. Khan, and C. Caloz, "Forward and backward coupled ring based electromagnetic phasers," in *IEEE European Conf. Antennas Propag. (EuCAP)*, Lisbon, Portugal, Apr. 2015.

[58] B. Nikfal, S. Gupta, and C. Caloz, "Increased group delay slope loop system for enhanced-resolution analog signal processing," *IEEE Trans. Microw. Theory Techn.*, vol. 59, no. 6, pp. 1622 – 1628, Jun. 2011.

[59] B. Xiang, X. Wang, and A. B. Apsel, "A reconfigurable integrated dispersive delay line (RI-DDL) in 0.13-μm CMOS process," *IEEE Trans. Microw. Theory Techn.*, vol. 61, no. 7, pp. 2610 – 2619, Jul. 2013.

[60] J. D. Schwartz, J. Azaña, and D. V. Plant, "Experimental demonstration of real-time spectrum analysis using dispersive microstrip," *IEEE Microw. Wireless Compon. Lett.*, vol. 16, no. 4, pp. 215–217, April 2006.

[61] S. Gupta and C. Caloz, "Analog real-time fourier transformer using a group delay engineered c-section all-pass network," in *IEEE AP-S Int. Antennas Propag. (APS)*, Toronto, Canada, July 2010, pp. 1–4.

[62] S. Gupta, S. Abielmona, and C. Caloz, "Microwave analog real-time spectrum analyzer (RTSA) based on the spectral-spatial decomposition property of leaky-wave structures," *IEEE Trans. Microw. Theory Techn.*, vol. 57, no. 12, pp. 2989 – 2999, Dec. 2009.

[63] M. Chudzik, I. Arnedo, A. Lujambio, I. Arregui, I. Gardeta, F. Teberio, J. Azaña, D. Benito, M. A. G. Laso, and T. Lopetegi, "Design of transmission-type Nth-order differentiators in planar microwave technology," *IEEE Trans. Microw. Theory Techn.*, vol. 60, no. 11, pp. 3384–3394, Nov 2012.

[64] I. Arnedo, J. D. Schwartz, M. A. G. Laso, T. Lopetegi, D. V. Plant, and J. Azaña, "Passive microwave planar circuits for arbitrary uwb pulse shaping," *IEEE Microw. Wireless Compon. Lett.*, vol. 18, no. 7, pp. 452–454, July 2008.

[65] G. Zhang, Q. Zhang, Y. Chen, T. Guo, C. Caloz, and R. D. Murch, "Dispersive feeding network for arbitrary frequency beam scanning in array antennas," *IEEE Trans. Antennas Propag.*, vol. 65, no. 6, pp. 3033–3040, June 2017.

[66] S. Gupta and C. Caloz, "Dispersion-compensation technique for log-periodic antennas using c-section all-pass dispersive delay structures," in *IEEE Int. Symp. Antennas Propag. (ISAP)*, Jeju, South Korea, Oct. 2011.

[67] B. Xiang, A. Kopa, Z. Fu, and A. B. Apsel, "Theoretical analysis and practical considerations for the integrated time-stretching system using dispersive delay line (DDL)," *IEEE Transactions on Microwave Theory and Techniques*, vol. 60, no. 11, pp. 3449 – 3457, Nov. 2012.

[68] J. D. Schwartz, J. Azaña, and D. V. Plant, "A fully electronic system for the time magnification of ultra-wideband signals," *IEEE Trans. Microw. Theory Techn.*, vol. 55, no. 2, pp. 327 – 334, Feb. 2007.

[69] ——, "An electronic temporal imaging system for compression and reversal of arbitrary UWB waveforms," in *Proc. IEEE Radio and Wireless Symp.*, Orlando, FL. U.S., Jan. 2008, pp. 487 – 490.

[70] S. Ding, S. Gupta, R. Zhang, L. Zou, B. Wang, and C. Caloz, "Enhancement of time-reversal subwavelength wireless transmission using pulse shaping," *IEEE Trans. Antennas Propag.*, vol. 63, no. 9, pp. 4169 – 4174, Sep. 2015.

[71] H. V. Nguyen and C. Caloz, "Crlh delay line pulse position modulation transmitter," *IEEE Microw. Wireless Compon. Lett.*, vol. 18, no. 8, pp. 527–529, Aug 2008.

[72] S. Abielmona, S. Gupta, and C. Caloz, "Compressive receiver using a CRLH-based dispersive delay line for analog signal processing," *IEEE Trans. Microw. Theory Techn.*, vol. 57, no. 11, pp. 2617 – 2626, Nov. 2009.

[73] B. Nikfal and C. Caloz, "Low-complexity and frequency-scalable analog real-time fdm receiver based on a dispersive delay structure," in *IEEE European Microw. Conf. (EuMC)*, Manchester, England, Oct. 2011, pp. 397 – 400.

[74] B. Nikfal, Q. Zhang, and C. Caloz, "Enhanced-SNR impulse radio transceiver based on phasers," *IEEE Microw. Wireless Compon. Lett.*, vol. 24, no. 11, pp. 778 – 780, Nov. 2014.

[75] H. Taki, S. Azou, A. Hamie, A. A. Housseini, A. Alaeddine, and A. Sharaiha, "On phaser-based processing of impulse radio {UWB} over fiber systems employing {SOA}," *Optical Fiber Technology*, vol. 36, pp. 33 – 40, 2017.

[76] E. Perret, M. Hamdi, G. E. P. Tourtollet, R. Nair, F. Garet, A. Delattre, A. Vena, L. Duvillaret, P. Martinez, S. Tedjini, and Y. Boutant, "THID, the next step of chipless RFID," in *RFID IEEE Int'l Conf.*, Penang, Malaysia, Apr. 2013.

[77] S. Gupta, B. Nikfal, and C. Caloz, "Chipless RFID system based on group delay engineered dispersive delay structures," *IEEE Antennas and Wireless Propag. Lett.*, vol. 10, pp. 1366 – 1368, Oct. 2011.

[78] B. Nikfal, C. Caloz, and M. A. Salem, "A method and apparatus for encoding data using instantaneous frequency dispersion," Patent WO/2015/179 949, May, 2015. [Online]. Available : https://patentscope.wipo.int/search/en/detail.jsf?docId=WO2015179949

[79] L. Zou, S. Gupta, and C. Caloz, "Real-time dispersion code multiple access (DCMA) for high-speed wireless communications," *arXiv :1703.10516*, 2017. [Online]. Available : http://arxiv.org/abs/1703.10516

[80] ——, "Dispersion code modulation for enhanced spectral efficiency in wireless communications," in *IEEE AP-S Int. Antennas Propag. (APS)*, Fajaro, Puerto Rico, Jun. 2016, pp. 1851 – 1852.

[81] S. Gupta and C. Caloz, "Perfect dispersive medium for real-time signal processing," *IEEE Trans. Antennas Propag.*, vol. -, no. -, pp. 601 – 611, - 2016.

[82] J. R. Andrews, "Picosecond pulse generation techniques and pulser capabilities," Picosecond pulse labs, Tech. Rep., 2008.

[83] A. Kamal, A. Bhattacharya, M. Tamrakar, and C. Roy, "Low-ring and reduced-cost step recovery diode based uwb pulse generators for GPR applications," *Microw. Opt. Technology Lett.*, vol. 56, no. 10, pp. 2289 – 2294, Oct. 2014.

[84] C. Zhang and A. E. Fathy, "Reconfigurable pico-pulse generator for UWB applications," in *IEEE MTT-S Int. Microw. Symp. (IMS)*, San Francisco, CA, Jun. 2006, pp. 407 – 410.

[85] A. F. Molisch, *Wireless Communications, 2nd Ed.* John Wiley & Sons, Inc., 2011.

[86] A. D. Polyanin and A. V. Manzhirov, *Handbook of Mathematics for Engineers and Scientists*. Boca Raton, FL. : CRC Press, Taylor & Francis Group, 2007.

[87] E. C. Farnett and G. H. Stevens, *Chapter 10, Pulse Compression Radar of Radar Handbook 2nd Ed. Edited by M. Skolnik*. McGraw Hill, 1990.

[88] M. B. N. Butler, "Radar applications of s.a.w. dispersive filters," *Communications, Radar and Signal Processing, IEE Proceedings F*, vol. 127, no. 2, pp. 118–124, Apr. 1980.

[89] M. Solal, "High performance SAW dispersive delay lines for low time bandwidth using periodically sampled transducers," in *IEEE 1988 Ultrasonics Symposium Proceedings.*, Oct 1988, pp. 175–178 vol.1.

[90] J. R. Klauder, P. A. C, S. Darlington, and W. J. Albersheim, "The theory and design of chirp radars," *Bell System Technical Journal*, vol. 39, pp. 745–808, 1960.

[91] J. W. Arthur, "Modern saw-based pulse compression systems for radar applications. part 1 : Saw matched filters," *Electronics & Communication Engineering Journal*, vol. 7, pp. 236–246, Dec. 1995.

[92] ——, "Modern saw-based pulse compression systems for radar applications. part 2 : Practical systems," *Electronics & Communication Engineering Journal*, vol. 8, pp. 57–78, Apr. 1996.

[93] G. Sisó, M. Gil, J. Bonache, and F. Martín, "On the dispersion characteristics of metamaterial transmission lines," *Journal of Applied Physics*, vol. 102, no. 7, p. 074911, 2007.

[94] C. Caloz, "Metamaterial dispersion engineering concepts and applications," *Proc. IEEE*, vol. 99, no. 10, pp. 1711–1719, Oct 2011.

[95] R. J. Cameron, "Advanced coupling matrix synthesis techniques for microwave filters," *IEEE Trans. Microw. Theory Techn.*, vol. 51, no. 1, pp. 1–10, Jan 2003.

[96] ——, "Advanced filter synthesis," *IEEE Microw. Mag.*, vol. 12, no. 6, pp. 42–61, Oct 2011.

[97] ——, *Microwave Filters for Communication Systems : Fundamentals, Design and Applications*. Hoboken, New Jersey : Wiley-Interscience, 2007.

[98] D. M. Pozar, *Microwave Engineering 4th Ed.* John Wiley, 2011.

[99] S. Lucyszyn and I. D. Robertson, "Analog reflection topology building blocks for adaptive microwave signal processing applications," *IEEE Trans. Microw. Theory Techn.*, vol. 43, no. 3, pp. 601 – 611, Mar. 1995.

[100] R. K. Mongia, I. J. Bahl, P. Bhartia, and J. Hong, *RF and Microwave Coupled-Line Circuits, 2nd Ed.* Norwood, MA : Artech House, 2007.

[101] S. Gupta, L. Zou, M. A. Salem, and C. Caloz, "Bit-error-rate (BER) performance in dispersion code multiple access (DCMA)," in *IEEE AP-S Int. Antennas Propag. (APS)*, Jul. 2015, pp. 1015 – 1016.

[102] S. Colangeli, R. Cleriti, D. Palombini, and E. Limiti, "On the unconditional stability of n-port networks," in *IEEE European Microw. Conf. (EuMC)*, Rome, Italy, Oct. 2014, pp. 1520–1523.

[103] S. Uysal and H. Aghvami, "Synthesis, design, and construction of ultra-wide-band nonuniform quadrature directional couplers in inhomogeneous media," *IEEE Trans. Microw. Theory Techn.*, vol. 37, no. 6, pp. 969 – 976, Jun. 1989.

[104] S. Lee and Y. Lee, "A design method for microstrip directional couplers loaded with shunt inductors for directivity enhancement," *IEEE Trans. Microw. Theory Techn.*, vol. 58, no. 4, pp. 994 – 1002, Apr. 2010.

[105] M. Dydyk, "Microstrip directional couplers with ideal performance via single-element compensation," *IEEE Trans. Microw. Theory Techn.*, vol. 47, no. 6, pp. 956 – 964, Jun. 1999.

[106] R. B. Marks, "A multiline method of network analyzer calibration," *IEEE Trans. Microw. Theory Techn.*, vol. 39, no. 7, pp. 1205–1215, Jul. 1991.

[107] M. Ferrera, Y. Park, L. Razzari, B. E. Little, S. T. Chu, R. Morandotti, D. J. Moss, and J. Azaña, "On-chip CMOS-compatible all-optical integrator," *Nature Comm.*, vol. 1, Jun. 2010.

[108] N. Ngo, S. Yu, S. Tjin, and C. Kam, "A new theoretical basis of higher-derivative optical differentiators," *Optics Communications*, vol. 230, no. 1, pp. 115 – 129, 2004.

[109] M. H. Asghari and J. Azaña, "All-optical hilbert transformer based on a single phase-shifted fiber bragg grating : design and analysis," *Opt. Lett.*, vol. 34, no. 3, pp. 334–336, Feb 2009.

[110] T. S. Rappaport, S. Sun, R. Mayzus, H. Zhao, Y. Azar, K. Wang, G. N. Wong, J. K. Schulz, M. Samimi, and F. Gutierrez, "Millimeter wave mobile communications for 5G cellular : It will work !" *IEEE Access*, vol. 1, pp. 335 – 349, May 2013.

[111] J. G. Andrews, S. Buzzi, W. Choi, S. V. Hanly, A. Lozano, A. C. K. Soong, and J. C. Zhang, "What will 5G be ?" *IEEE J. Sel. Areas Commun.*, vol. 32, no. 6, pp. 1065 – 1082, Jun. 2014.

[112] F. Boccardi, R. W. Heath, A. Lozano, T. L. Marzetta, and P. Popovski, "Five disruptive technology directions for 5G," *IEEE Commun. Mag.*, vol. 52, no. 2, pp. 74 – 80, Feb. 2014.

[113] A. Osseiran, F. Boccardi, V. Braun, K. Kusume, P. Marsch, M. Maternia, O. Queseth, M. Schellmann, H. Schotten, H. Taoka, H. Tullberg, M. A. Uusitalo, B. Timus, , and M. Fallgren, "Scenarios for 5G mobile and wireless communications : the vision of the METIS project," *IEEE Commun. Mag.*, vol. 52, no. 5, pp. 26 – 35, May 2014.

[114] M. Z. Win and R. A. Scholtz, "Impulse radio : How it works," *IEEE Commun. Lett.*, vol. 2, no. 2, pp. 36 – 38, Feb. 1998.

[115] ——, "Ultra-wide bandwidth time-hopping spread spectrum impulse radio for wireless multiple-access communications," *IEEE Trans. Commun.*, vol. 48, no. 4, pp. 679 – 691, Apr. 2000.

[116] H. Fathallah, L. A. Rusch, and S. LaRochelle, "Passive optical fast frequency-hop CDMA communications system," *J. Lightw. Technol.*, vol. 17, no. 3, pp. 397 – 405, Mar. 1999.

[117] L. R. Chen, "Flexible fiber Bragg grating encoder/decoder for hybrid wavelength-time optical CDMA," *IEEE Photon. Technol. Lett.*, vol. 13, no. 11, pp. 1233 – 1235, Nov. 2001.

[118] H. Tamai, H. Iwamura, N. Minato, and S. Oshiba, "Experimental study on time-spread/wavelength-hop optical code division multiplexing with group delay compensating en/decoder," *IEEE Photon. Technol. Lett.*, vol. 16, no. 1, pp. 335 – 337, Jan. 2004.

[119] J. Yao, "Microwave photonics," *J. Lightw. Technol.*, vol. 27, no. 3, pp. 314 – 335, Feb. 2009.

[120] Ş. Selçuk Bayin, *Essentials of Mathematical Methods in Science and Engineering.* Hoboken, NJ : John Wiley & Sons, Ltd, 2008.

[121] S. Taravati, S. Gupta, Q. Zhang, and C. Caloz, "Enhanced bandwidth and diversity in real-time analog signal processing (R-ASP) using nonuniform c-section phasers," *IEEE Microw. Wireless Compon. Lett.*, vol. 26, no. 9, pp. 663 – 665, Sep. 2016.

[122] J. D. Gibson, *The Mobile Communication Handbook, 2nd Ed.* Boca Raton, FL. : CRC Press, 1999.

[123] S. M. Sze and K. N. Kwok, *Physics of Semiconductor Devices 3rd Ed.* Hoboken, New Jersey : John Wiley & Sons, 2007.

[124] J. Bird, *Electrical Circuit Theory and Technology 5th Ed.* Routledge, 2013.

[125] P. Gibson, "The vivaldi aerial," in *IEEE European Microw. Conf. (EuMC)*, Brighton, England, Sep. 1979, pp. 1851 – 1852.

[126] K. Kikuta and AHirose, "Dispersion characteristics of ultra wideband antennas and their radiation patterns," in *Proc. URSI Int'l Symp. on Electromagnetic Theory (EMTS)*, Hiroshima, Japan, May 2013, pp. 462 – 465.

[127] W. Wiesbeck, G. Adamiuk, and C. Sturm, "Basic properties and design principles of UWB antennas," *Proc. IEEE*, vol. 97, no. 2, pp. 372 – 385, Feb. 2009.

[128] Y. Horii, S. Gupta, B. Nikfal, and C. Caloz, "Multilayer broadside-coupled dispersive delay structures for analog signal processing," *IEEE Microw. Wireless Compon. Lett.*, vol. 22, no. 1, pp. 1 – 3, Jan. 2012.

[129] A. Goldsmith, *Wireless Communications*. New York : Cambridge University Press, 2005.

[130] A. F. Molisch, "Ultra-wide-band propagation channels," *Proc. IEEE*, vol. 97, no. 2, pp. 353–371, Feb. 2009.

[131] L. Zou, S. Gupta, and C. Caloz, "Time-reversal based routing in dispersion code multiple access (dcma)," in *IEEE Int. Symp. Antennas Propag. (ISAP)*, Hobart, Australia, Nov. 2015, pp. 366 – 369.

[132] M. Fink, "Time reversal of ultrasonic fields-part I : Basic principles," *IEEE Trans. Ultrason., Ferroelect., Freq. Control*, vol. 39, no. 5, pp. 555 – 566, May 1992.

[133] G. Lerosey, J. de Rosny, A. Tourin, A. Derode, G. Montaldo, and M. Fink, "Time reversal of electromagnetic waves," *Phys. Rev. Lett.*, vol. 92, p. 193904, May 2004.

[134] J. R. Foerster, M. Pendergrass, and A. F. Molisch, "A channel model for ultra wideband indoor communication," Mitsubishi Electric Research Laboratories, Inc., Tech. Rep., Oct. 2003.

[135] L. Zou and C. Caloz, "Concept of combined phaser-antenna - "phasenna" ? - for wireless radio analog signal processing (R-ASP)," in *2014 IEEE AP-S Int. Antennas Propag. (APS)*, Memphis, TN, US, July 2014, pp. 822–823.

[136] C. T. M. Wu, S. Gharavi, B. Daneshrad, and T. Itoh, "Group delay dispersion engineered antenna array," in *2013 Euro. Microw. Conf. (EuMC)*, Nuremberg, Germany, Oct 2013, pp. 1663–1666.

[137] K. L. Tsakmakidis, L. Shen, S. A. Schulz, X. Zheng, J. Upham, X. Deng, H. Altug, A. F. Vakakis, and R. W. Boyd, "Breaking lorentz reciprocity to overcome the time-bandwidth limit in physics and engineering," *Science*, vol. 356, no. 6344, pp. 1260–1264, Jun. 2017.

[138] C. Caloz, Z.-L. Deck-Léger, and N. Chamanara, "Towards space-time metamaterials," in *Int. Congress Advanced Electromagnetic Mat. Microw. Opt.*, Marseille, France, Aug. 2017, p. 849–851.

[139] P. Paliwal, P. Laad, M. Sattineni, and S. Gupta, "Tradeoffs between settling time and jitter in phase locked loops," in *2013 IEEE 56th Int'l Midwest Symp. on Circuits and Systems (MWSCAS)*, Columbus, OH, USA, Aug 2013, pp. 746–749.

ANNEXE A PARITY RELATIONSHIP BETWEEN THE CHEBYSHEV GROUP DELAY AND THE INTERFERENCE WAVEFORM

We shall show that if $\tau_{ik}(\omega)$ is odd (about the center frequency, ω_0), then $|h_{ik}(t)|$ (envelope) is even (about the center delay, $2\tau_0$), while if $\tau_{ik}(\omega)$ is even (about ω_0), then $|h_{ik}(t)|$ is neither even nor odd, as illustrated in Fig. 4.4. The cascaded group delay $\tau_{ik}(\omega)$ [Eq. (4.9)] for the all-odd and all-even coding cases is written as an odd function and an even function of ω, offset by $2\tau_0$ (constant), respectively, i.e.

$$\tau_{ik,\text{odd-coding}}(\omega) = \tau_{\text{odd}}(\omega) + 2\tau_0, \tag{A.1a}$$

$$\tau_{ik,\text{even-coding}}(\omega) = \tau_{\text{even}}(\omega) + 2\tau_0, \tag{A.1b}$$

where

$$\tau_{\text{odd}}(\omega_0 - u) = -\tau_{\text{odd}}(\omega_0 + u), \tag{A.1c}$$

$$\tau_{\text{even}}(\omega_0 - u) = \tau_{\text{even}}(\omega_0 + u). \tag{A.1d}$$

The corresponding phase, being the antiderivative of the group delay, includes a dispersive term with opposite parity, a linear (non-dispersive) term and a constant term, i.e.

$$\phi_{ik,\text{odd-coding}}(\omega) = \phi_{\text{even}}(\omega) - 2\tau_0\omega + C_{\text{odd-coding}}, \tag{A.2a}$$

$$\phi_{ik,\text{even-codin}}(\omega) = \phi_{\text{odd}}(\omega) - 2\tau_0\omega + C_{\text{even-coding}}, \tag{A.2b}$$

where

$$\phi_{\text{even}}(\omega_0 - u) = \phi_{\text{even}}(\omega_0 + u), \tag{A.2c}$$

$$\phi_{\text{odd}}(\omega_0 - u) = -\phi_{\text{odd}}(\omega_0 + u), \tag{A.2d}$$

and $C_{\text{odd-coding}}$ and $C_{\text{even-coding}}$ are constants, that we set to zero without loss of generality. The transfer functions corresponding to (A.2) are then

$$H_{ik,\text{odd-coding}}(\omega) = \text{rect}\left(\frac{\omega - \omega_0}{\Delta\omega}\right) e^{j\phi_{\text{even}}(\omega)} e^{-j2\tau_0\omega}, \tag{A.3a}$$

$$H_{ik,\text{even-coding}}(\omega) = \text{rect}\left(\frac{\omega - \omega_0}{\Delta\omega}\right) e^{j\phi_{\text{odd}}(\omega)} e^{-j2\tau_0\omega}. \tag{A.3b}$$

Let us now derive the impulse responses, which are the inverse Fourier transforms of (A.3).

For the all-odd coding case,

$$\begin{aligned} h_{ik,\text{odd-coding}}(t) &= \mathcal{F}^{-1}[H_{ik,\text{odd-coding}}(\omega)] \\ &= h'_{ik}(t) * \delta(t - 2\tau_0), \end{aligned} \tag{A.4a}$$

where

$$h'_{ik}(t) = \frac{1}{2\pi} \int_{-\infty}^{+\infty} \text{rect}\left(\frac{\omega - \omega_0}{\Delta\omega}\right) e^{j\phi_{\text{even}}(\omega)} e^{j\omega t}\, d\omega. \tag{A.4b}$$

Under the substitution $\omega - \omega_0 = u$, Eq. (A.4b) becomes

$$\begin{aligned} h'_{ik}(t) &= \frac{1}{2\pi} \int_{-\infty}^{+\infty} \text{rect}\left(\frac{u}{\Delta\omega}\right) e^{j\phi_{\text{even}}(\omega_0+u)} e^{j(\omega_0+u)t}\, du \\ &= \frac{e^{j\omega_0 t}}{2\pi} \int_{-\infty}^{+\infty} \text{rect}\left(\frac{u}{\Delta\omega}\right) e^{j\phi_{\text{even}}(\omega_0+u)} e^{jut}\, du \\ &= A(t) \cdot e^{j\omega_0 t}, \end{aligned} \tag{A.5a}$$

where

$$A(t) = \frac{1}{2\pi} \int_{-\infty}^{+\infty} \text{rect}\left(\frac{u}{\Delta\omega}\right) e^{j\phi_{\text{even}}(\omega_0+u)} e^{jut}\, du \tag{A.5b}$$

is seen to be the envelope of $h'_{ik}(t)$ corresponding to the carrier term $\exp(j\omega_0 t)$. We shall now show that $A(t)$ is even-symmetric about $t = 0$, i.e. $A(-t) = A(t)$, so that the envelop of $h_{ik,\text{odd-coding}}(t)$ [Eq. (A.4a)] is even-symmetric about $t = 2\tau_0$ due to the time-shift resulting from the convolution with $\delta(t - 2\tau_0)$. For this purpose, let us examine $A(-t)$. We have

$$\begin{aligned} A(-t) &= \frac{1}{2\pi} \int_{-\infty}^{+\infty} \text{rect}\left(\frac{u}{\Delta\omega}\right) e^{j\phi_{\text{even}}(\omega_0+u)} e^{ju(-t)}\, du \\ &= \frac{1}{2\pi} \int_{-\infty}^{+\infty} \text{rect}\left(\frac{u}{\Delta\omega}\right) e^{j\phi_{\text{even}}(\omega_0+u)} e^{j(-u)t}\, du. \end{aligned} \tag{A.6}$$

Substituting $-u = u'$ transforms. (A.6) into

$$\begin{aligned} A(-t) &= \frac{1}{2\pi} \int_{+\infty}^{-\infty} \text{rect}\left(\frac{-u'}{\Delta\omega}\right) e^{j\phi_{\text{even}}(\omega_0-u')} e^{ju't}\, d(-u') \\ &= \frac{1}{2\pi} \int_{-\infty}^{+\infty} \text{rect}\left(\frac{-u'}{\Delta\omega}\right) e^{j\phi_{\text{even}}(\omega_0-u')} e^{ju't}\, du'. \end{aligned} \tag{A.7}$$

Note that both the transfer magnitude and phase in (A.7) are even, i.e. $\text{rect}(-u'/\Delta\omega) = \text{rect}(u'/\Delta\omega)$ and $\phi_{\text{even}}(\omega_0 - u') = \phi_{\text{even}}(\omega_0 + u')$ [Eq. (A.2c)]. Thus

$$A(-t) = \frac{1}{2\pi} \int_{-\infty}^{+\infty} \text{rect}\left(\frac{u'}{\Delta\omega}\right) e^{j\phi_{\text{even}}(\omega_0+u')} e^{ju't}\, du'. \tag{A.8}$$

Comparing (A.8) with (A.5b) yields

$$A(-t) = A(t), \tag{A.9}$$

and hence the envelop of Eq. (A.4a) is indeed symmetric about $t = 2\tau_0$ for odd coding case as already shown in Fig. 4.4. The demonstration of (A.9) has used the following property of the Fourier transform pair : an even (resp. odd) transfer function, whose transfer magnitude and phase are both even (resp. odd), corresponds to an even (resp. odd) impulse response envelope [86]. When the coding set is even, the corresponding envelope is computed by (A.5b) with the transfer phase $\phi_{\text{even}}(\omega_0 + u)$ replaced by $\phi_{\text{odd}}(\omega_0 + u)$, which is an odd function of u, according to (A.2d). However, the transfer magnitude is still even (rectangular), leading to an envelope function that is neither even nor odd.

ANNEXE B COMPARISON OF DIFFERENT UWB PULSE GENERATION TECHNOLOGIES

Table B.1 Experimental performance comparison between the stub-less pulse generator and stub-based ones reported in [2] and [3]. The efficiency may be defined as the ratio of the output peak amplitude to the input peak amplitude (L. Zou, et al, [4], MWCL, ©2017 IEEE).

	Stub-less	Stub-based [2]	Stub-based [3]
Tunability	easy	hard [84]	
Complexity	low	high	
PRR	100 MHz	10 MHz	10 MHz
Pulse width	62 ps (min) [1]	330 ps	> 1 ns
Rising/falling	SRD dependent, typical $30 - 150$ ps		
Amplitude	0.6 - 0.7 V	2 V	1.8 V
Efficiency	low	higher	

1. Pulse width is more temperature sensitive than stub-based generator.